

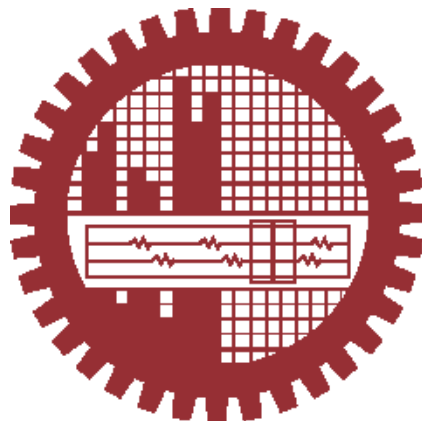
**SYNTHESIS OF NOVEL MAGNETITE NANOPARTICLES WITH CHITOSAN  
MESOPOROUS SILICA COATING FOR EFFICIENT REMOVAL OF HEAVY  
METALS FROM WASTEWATER**

**By**

**Kazi Faiza Amin**

**Student No- 0417112005**

MASTER OF SCIENCE IN MATERIALS AND METALLURGICAL ENGINEERING



Department of Materials and Metallurgical Engineering  
Bangladesh University of Engineering and Technology (BUET)

24 May, 2022


## *Candidate's Declaration*

I hereby certify that the work which is being submitted entitled as: "SYNTHESIS OF NOVEL MAGNETITE NANOPARTICLES WITH CHITOSAN MESOPOROUS SILICA COATING FOR EFFICIENT REMOVAL OF HEAVY METALS FROM WASTEWATER" in partial fulfilment of the requirements for the award of Masters of Science in Materials and Metallurgical Engineering at Bangladesh University of Engineering and Technology (BUET) is a successive record of my own work carried out during the period of October 2020 to January 2022. The research described herein was conducted under the supervision of Professor Dr. Fahmida Gulshan from the Department of Materials and Metallurgical Engineering, Bangladesh University of Engineering and Technology (BUET) and Dr. Sheikh Manjura Hoque of Materials Science Division, Atomic Energy Centre, Dhaka.

This work is entirely original, except where acknowledgements and references are made to previous work. Neither this, nor any substantially similar thesis is being submitted for any other degrees or other qualification at any other university.

Date: 24 May, 2022

Candidate's Signature: .....



Kazi Faiza Amin

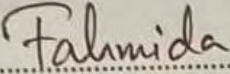
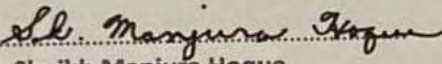
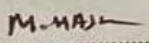
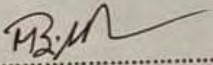
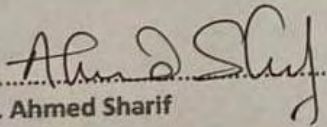
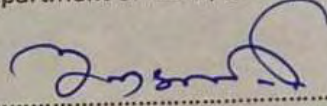
Student ID: 0417112005

MSc. Engg. MME, BUET

## Approval page

The thesis titled "SYNTHESIS OF NOVEL MAGNETITE NANOPARTICLES WITH CHITOSAN MESOPOROUS SILICA COATING FOR EFFICIENT REMOVAL OF HEAVY METALS FROM WASTEWATER" submitted by Kazi Faiza Amin, Roll No: 0417112005, Session: April/2017, has been accepted as satisfactory in partial fulfillment of the requirement for the degree of Masters of Science in Materials and Metallurgical Engineering on 24 May, 2022.

### BOARD OF EXAMINERS

1.   
.....  
**Dr. Fahmida Gulshan**  
Professor  
MME, BUET, Dhaka  
Chairman  
(Supervisor)
2.   
.....  
**Dr. Sheikh Manjura Hoque**  
Head  
Materials Science Division, Atomic Energy Center, Dhaka.  
Member  
(Co-Supervisor)
3.   
.....  
Head  
Professor  
Department of MME, BUET, Dhaka  
Member  
(Ex-officio)
4.   
.....  
**Dr. Md. Muktadir Billah**  
Associate Professor  
Department of MME, BUET, Dhaka  
Member
5.   
.....  
**Dr. Ahmed Sharif**  
Professor  
Department of MME, BUET, Dhaka.  
Member
6.   
.....  
**Dr. Al-Nakib Chowdhury**  
Professor  
Department of Chemistry, BUET, Dhaka  
Member  
(External)

## *Acknowledgement*

First of all, I would like to pay my gratitude to almighty Allah for His upmost favor and enormous blessings to complete my research in due time and without any difficulties.

I would like to take this opportunity to express my heartiest gratitude to the following people for their invaluable help rendered during my candidatures as M.Sc. Engg. student at the Department of Materials and Metallurgical Engineering, Bangladesh University of Engineering and Technology (BUET).

I would like to express my sincerest gratitude to my supervisors, Professor Dr. Fahmida Gulshan and Dr. Sheikh Manjura Hoque for their invaluable advices, encouragement and patience during this research period.

I am deeply indebted to Dr. Harinarayan Das, Dr. Rimi Rashid of Materials Science Division, Atomic Energy Centre, Dhaka for their sincere assistance and encouragement to this work. I would like to convey my gratitude to Ms. Jhorna and Ms. Nurunnahar Sheuli of Atomic Energy Center, Dhaka for their help in performing my experiments at the laboratory successfully. I am thankful to Mr. Badhan Saha of BCSIR for his sincere help in the AAS experiments.

Finally, I express my profound gratitude towards my loving family without whom I could not have done this.

**Kazi Faiza Amin**

May 2022

## Abstract

Contamination of natural water resources by heavy metal pollutants present in wastewater has become a worldwide concern. Removal of heavy metal ions by surface functionalized magnetic nanoparticles adsorption is an economical route due to its simplicity and easy operation. However, bare magnetite nanoparticles are not good adsorbents and are susceptible to oxidation and agglomeration. The challenge is to develop economically feasible magnetite nanoparticles with an appropriate surface functionalization that will simultaneously provide adsorption efficiency, hydrophilicity, and recyclability without compromising magnetic properties. The aim of this study was to develop magnetite nanoparticles with a combined coating of chitosan and mesoporous silica which would act as an efficient adsorbent of heavy metal ions i.e.,  $\text{Pb}^{2+}$ ,  $\text{Cd}^{2+}$  and  $\text{As}^{3+}$  from water. The  $\text{Fe}_3\text{O}_4$  nanoparticles were synthesized via thermal decomposition method of iron-oleate precursor. The synthesized particles were subjected to X-ray diffraction (XRD), Physical Property Measurement System (PPMS), and Transmission Electron Microscopy (TEM) to determine the crystalline phase, crystallite size, magnetic properties, and morphology respectively. The coating of mesoporous silica was formed on the particles by reaction of phase transferring them with the help of Cetrimonium bromide (CTAB) and addition of Tetraethyl orthosilicate (TEOS). The chitosan coating over the mesoporous silica coated particles was put by subjecting the particles to 5% chitosan solution in acetic acid with pH 6.0. The successful formation of the coatings was confirmed by conducting Fourier-transform infrared spectroscopy (FTIR) analysis. The final substance to be used as the adsorbent exhibited a saturation magnetization of 28.84 emu/g. The coated particles were used as adsorbents for  $\text{Pb}^{2+}$ ,  $\text{Cd}^{2+}$  and  $\text{As}^{3+}$  present in water. During the adsorption experiments the contact time and initial concentration parameters were varied and the corresponding data was fitted to pseudo-first

order and pseudo-second order kinetic model to determine the adsorption mechanism. The data was also fitted to the Langmuir and Freundlich adsorption isotherms. The data demonstrated a closer fitting to the Pseudo-2<sup>nd</sup> order kinetic model and the Langmuir Isotherm model. Based on these results the adsorption process is determined to be a monolayer chemisorption and the particles were concluded to be an efficient heavy metal adsorbent with adsorption capacity of 150.33 mg/g, 126.26 mg/g, and 3.021 mg/g for Pb<sup>2+</sup>, Cd<sup>2+</sup> and As<sup>3+</sup> respectively.

**Keywords:** Adsorption, magnetite nanoparticles, mesoporous silica, chitosan, adsorption kinetic models, adsorption isotherm models, lead, cadmium, arsenic.

## Table of Contents

Abstract.....	iv
List of Figures .....	ix
List of Tables .....	xi
List of Abbreviations .....	xii
1 Chapter 1: Introduction .....	1
2 Chapter 2: Literature Review.....	4
2.1 Magnetic Nanoparticles.....	4
2.1.1 Superparamagnetism.....	5
2.1.1.1 Effect of Magnetic Field- Langevin Function .....	7
2.1.2 Synthesis of Magnetic Nanoparticle .....	8
2.1.2.1 Co-precipitation .....	8
2.1.2.2 Thermal Decomposition .....	9
2.1.2.3 Microemulsion.....	10
2.1.2.4 Hydro/Solvothermal .....	11
2.1.3 Phase Transfer of Magnetic Nanoparticles.....	13
2.2 Surface Functionalization of Magnetic Nanoparticles.....	14
2.2.1 Surface Modification with Mesoporous Silica .....	16
2.2.2 Synthesis of Mesoporous Silica.....	17
2.3 Chitosan .....	18
2.3.1 Chitosan Grafting on Mesoporous Silica.....	19
2.3.2 Adsorption and desorption mechanism of chitosan .....	20
2.4 Heavy metal pollution of water .....	21

2.5	Techniques for heavy metal removal from water .....	23
2.5.1	Chemical precipitation .....	23
2.5.2	Ion exchange .....	23
2.5.3	Membrane filtration .....	24
2.5.4	Coagulation and flocculation .....	25
2.5.5	Flotation .....	25
2.5.6	Electrochemical treatment .....	26
2.5.7	Adsorption .....	27
2.5.7.1	Adsorbent Categories .....	28
2.5.7.1.1	Natural Adsorbents .....	28
2.5.7.1.2	Synthetic Adsorbents .....	29
2.6	Fundamentals of adsorption.....	30
2.6.1	Classification of adsorption.....	30
2.6.2	Adsorption Kinetics.....	30
2.6.2.1	Kinetic Models Based on the Order of Reaction .....	31
2.6.2.2	Empiric adsorption kinetic models .....	31
2.6.3	Adsorption Isotherms .....	32
2.6.3.1	Langmuir isotherm model .....	32
2.6.3.2	Freundlich isotherm model .....	33
2.6.3.3	Sips isotherm model .....	34
2.6.3.4	Liu isotherm model.....	34
2.6.3.5	Redlich–Peterson isotherm model .....	35
2.6.3.6	Other isotherm models for adsorption .....	35
3	Chapter 3: Experimental Details.....	37



3.1	Raw Materials .....	37
3.2	Synthesis of Fe <sub>3</sub> O <sub>4</sub> MNPs .....	38
3.3	Surface functionalization of MNPs with mesoporous silica and chitosan.....	40
3.4	Adsorption test .....	41
3.5	Characterizations .....	42
3.5.1	X-ray Diffractometry (XRD) .....	42
3.5.2	Transmission Electron Microscopy (TEM) .....	43
3.5.3	Fourier Transform Infrared Spectroscopy (FTIR) .....	43
3.5.4	Physical Properties Measurement System (PPMS) .....	44
3.5.5	Atomic Absorption Spectroscopy (AAS).....	44
4	Chapter 4: Results and Discussion.....	45
4.1	X-Ray Diffraction Analysis .....	45
4.2	Transmission Electron Microscopy Analysis .....	48
4.3	Fourier Transform Infrared Spectroscopic Analysis.....	52
4.4	VSM Data Analysis .....	53
4.5	Adsorption Data Analysis.....	56
4.5.1	Adsorption Kinetic Model Fitting.....	59
4.5.2	Adsorption Isotherm Model Fitting .....	64
4.5.3	Desorption Study .....	70
5	Chapter 5: Conclusion & Recommendation .....	72
5.1	Concluding Remarks.....	72
5.2	Recommendations for Future Prospect.....	73
6	References .....	74

## List of Figures

Figure 2–1: Crystal structure of magnetite ( $\text{Fe}_3\text{O}_4$ ). .....	5
Figure 2–2: Magnetization of superparamagnetic nanoparticles. ....	7
Figure 2–3: Comparison of ferromagnetic, paramagnetic, and superparamagnetic magnetization curves. ....	7
Figure 2–4: Overview of synthesis methods for $\text{Fe}_3\text{O}_4$ MNPs. ....	8
Figure 2–5: Synthesis of $\text{Fe}_3\text{O}_4$ MNPs via thermal decomposition method. ....	10
Figure 2–6: Synthesis of MNPs via microemulsion method. ....	11
Figure 2–7: Phase transfer of hydrophobic MNPs. ....	13
Figure 2–8: Illustration of modified surface of MNPs. ....	14
Figure 2–9: Different types of mesoporous $\text{SiO}_2$ structures. ....	17
Figure 2–10: Synthesis of mesoporous $\text{SiO}_2$ on MNPs. ....	17
Figure 2–11: Derivation of chitosan from chitin. ....	19
Figure 2–12: Adsorption-desorption mechanism of heavy metal by chitosan. ....	21
Figure 2–13: Ion exchange process of heavy metal removal. ....	24
Figure 2–14: Illustration of the electrocoagulation and electrofloatation process of heavy metal removal from water. ....	26
Figure 2–15: Illustration of adsorption of heavy metals by surface functionalized MNPs. ....	27
Figure 3–1: Thermal decomposition synthesis of $\text{Fe}_3\text{O}_4$ MNPs. ....	39
Figure 3–2: Surface functionalization of $\text{Fe}_3\text{O}_4$ MNPs with mesoporous $\text{SiO}_2$ and chitosan. ....	40
Figure 3–3: Adsorption experiment. ....	42
Figure 3–4: Rigaku SmartLab XRD machine. ....	42
Figure 3–5: TEM machine. ....	43
Figure 3–6: FTIR machine. ....	43
Figure 3–7: Physical Properties Measurement System. ....	44
Figure 3–8: AAS machine. ....	44
Figure 4–1: XRD plot of the bare and coated $\text{Fe}_3\text{O}_4$ MNPs. ....	45
Figure 4–2: Comparative stacking of XRD plots of bare and coated $\text{Fe}_3\text{O}_4$ MNPs. ....	46

Figure 4–3: TEM images of (a) and (b) bare Fe <sub>3</sub> O <sub>4</sub> MNPs; (c) and (d) mesoporous SiO <sub>2</sub> coated Fe <sub>3</sub> O <sub>4</sub> MNPs.....	48
Figure 4–4: Size distribution of bare Fe <sub>3</sub> O <sub>4</sub> MNPs. ....	49
Figure 4–5: Size distribution of mesoporous SiO <sub>2</sub> coated Fe <sub>3</sub> O <sub>4</sub> MNPs.....	49
Figure 4–6: SAED pattern of bare Fe <sub>3</sub> O <sub>4</sub> MNPs.....	50
Figure 4–7: EDS spectra of bare Fe <sub>3</sub> O <sub>4</sub> MNPs. ....	51
Figure 4–8: EDS spectra of mesoporous SiO <sub>2</sub> coated Fe <sub>3</sub> O <sub>4</sub> MNPs.....	51
Figure 4–9: FTIR spectra of Fe <sub>3</sub> O <sub>4</sub> -SiO <sub>2</sub> -CTAB, Fe <sub>3</sub> O <sub>4</sub> -SiO <sub>2</sub> , and Fe <sub>3</sub> O <sub>4</sub> -SiO <sub>2</sub> -Chitosan MNPs. ....	52
Figure 4–10: M-H curves of bare Fe <sub>3</sub> O <sub>4</sub> , SiO <sub>2</sub> coated Fe <sub>3</sub> O <sub>4</sub> and SiO <sub>2</sub> -Chitosan coated Fe <sub>3</sub> O <sub>4</sub> MNPs. .....	53
Figure 4–11: Langevin function fitting to the M-H curve of bare Fe <sub>3</sub> O <sub>4</sub> MNPs. ....	55
Figure 4–12: Langevin function fitting to the M-H curve of SiO <sub>2</sub> coated Fe <sub>3</sub> O <sub>4</sub> MNPs.....	55
Figure 4–13: Langevin function fitting to the M-H curve of SiO <sub>2</sub> -Chitosan coated Fe <sub>3</sub> O <sub>4</sub> MNPs. ....	56
Figure 4–14: Contact time effect on the adsorption capacity of lead (Pb <sup>2+</sup> ).....	58
Figure 4–15: Contact time effect on the adsorption capacity of cadmium (Cd <sup>2+</sup> ). ....	58
Figure 4–16: Contact time effect on the adsorption capacity of arsenic (As <sup>3+</sup> ). ....	59
Figure 4–17: Lead (Pb <sup>2+</sup> ) adsorption data fitting to the pseudo first order kinetic model.....	60
Figure 4–18: Cadmium (Cd <sup>2+</sup> ) adsorption data fitting to the pseudo first order kinetic model... ..	60
Figure 4–19: Arsenic (As <sup>3+</sup> ) adsorption data fitting to the pseudo first order kinetic model.....	61
Figure 4–20: Lead (Pb <sup>2+</sup> ) adsorption data fitting to the pseudo second order kinetic model. ....	62
Figure 4–21: Cadmium (Cd <sup>2+</sup> ) adsorption data fitting to the pseudo second order kinetic model. .....	62
Figure 4–22: Arsenic (As <sup>3+</sup> ) adsorption data fitting to the pseudo second order kinetic model. ....	63
Figure 4–23: Lead (Pb <sup>2+</sup> ) adsorption data fitting to the Langmuir isotherm model.....	65
Figure 4–24: Cadmium (Cd <sup>2+</sup> ) adsorption data fitting to the Langmuir isotherm model.....	66
Figure 4–25: Arsenic (As <sup>3+</sup> ) adsorption data fitting to the Langmuir isotherm model.....	66
Figure 4–26: Lead (Pb <sup>2+</sup> ) adsorption data fitting to the Freundlich isotherm model.....	67
Figure 4–27: Cadmium (Cd <sup>2+</sup> ) adsorption data fitting to the Freundlich isotherm model.....	68
Figure 4–28: Arsenic (As <sup>3+</sup> ) adsorption data fitting to the Freundlich isotherm model.....	68

## List of Tables

Table 2–1: Estimated maximum single domain size for different magnetic materials [12].....	6
Table 2–2: Comparison between chemical synthesis methods of MNPs.....	12
Table 2–3: Reported studies of surface functionalization for heavy metal removal. ....	15
Table 2–4: Short list of recent works on mesoporous SiO <sub>2</sub> –chitosan drug delivery system.....	19
Table 2–5: World health organization (WHO) permissible limit of heavy metals in wastewater.	22
Table 2–6: WHO designated permissible heavy metal limit in drinking water. ....	22
Table 2–7: List of other reported adsorption isotherm models. ....	35
Table 3–1: List of chemical reagents used at different stages of experiment.....	37
Table 4–1: Calculation of crystallite size of Fe <sub>3</sub> O <sub>4</sub> MNPs from FWHM.....	47
Table 4–2: Result of Langevin function fitting to the VSM data.....	54
Table 4–3: Comparison of magnetic properties of various reported magnetic adsorbents.....	54
Table 4–4: Adsorption data of Pb <sup>2+</sup> , Cd <sup>2+</sup> , and As <sup>3+</sup> with variable contact time.....	57
Table 4–5: Parameters of the pseudo first order kinetic model fitting to the adsorption data. .	60
Table 4–6: Parameters of the pseudo second order kinetic model fitting to the adsorption data. .....	61
Table 4–7: Adsorption data of Pb <sup>2+</sup> , Cd <sup>2+</sup> , and As <sup>3+</sup> with variable initial solution concentration.	64
Table 4–8: Parameters of the Langmuir isotherm model fitting to the adsorption data. ....	65
Table 4–9: Parameters of the Freundlich isotherm model fitting to the adsorption data. ....	67
Table 4–10: Comparison of maximum adsorption capacity of current work and other reported adsorbents. ....	70
Table 4–11: Concentration profile of desorption solution. ....	71

## List of Abbreviations

MNPs	Magnetic nanoparticles
nm	Nanometer
CTAB	Cetrimonium bromide
TEOS	Tetraethyl orthosilicate
mg	Milligram
µg	Microgram
ml	Milliliter
L	Liter
g	Gram
ppm	Parts per million
ppb	Parts per billion
°C	Degree Celsius
XRD	X-ray diffraction spectroscopy
TEM	Transmission electron microscopy
EDS	Energy dispersive x-ray spectroscopy
FTIR	Fourier transform infra-red spectroscopy
PPMS	Physical properties measurement system
VSM	Vibrating Sample Magnetometer
emu	Electromagnetic unit
AAS	Atomic absorption spectroscopy
Adj. R <sup>2</sup>	Adjusted linear regression coefficient

## 1 Chapter 1: Introduction

Water is a primary resource for the presence of life on earth and access to clean water is critical for humans and the ecosystem. Nonetheless, during the recent decades, water quality has been negatively influenced by a continuously increasing population, rapid industrialization, increasing urbanization, and careless utilization of natural resources. Organic matter, nutrients, pharmaceutical and personal care products, poly- and perfluoroalkyl substances, biocides, heavy metals, dyes, radionuclides, plastics, nanoparticles and pathogens are among the pollutants of major concern [1].

Heavy metal ions are among the most released contaminants. Heavy metals and metalloids are elements with density greater than  $4 \text{ g/cm}^3$  which include copper (Cu), cadmium (Cd), zinc (Zn), lead (Pb), mercury (Hg), arsenic (As), silver (Ag), chromium (Cr), iron (Fe) and platinum (Pt). Heavy metals are a group of metals found in large quantities in the earth's crust. Heavy metals like copper and zinc may be required in tiny levels by humans. But large quantities of these metals can be hazardous. The sources of these pollutants can be both natural and man-made. Natural sources include the interactions with metal or metal salt containing rocks and volcanic eruptions. Man-made sources include industrial activities such as fossil fuel combustion, metal processing, tannery wastes, agricultural, and domestic waste products like pesticides and detergents. Heavy metals are non-biodegradable in nature. These metals are a potential risk, given these hazards and their wide exposure in the environment including their bioaccumulation. Metals, such as cadmium (Cd), lead (Pb), arsenic (As), Nickel (Ni) are potentially highly toxic. These metals have a number of adverse outcomes for human health, including kidney failure, softening of bones, prostate cancer, and damage to the liver, children's central nervous system and the reproductive system [2].

The US Environmental Protection Agency (USEPA) regulates heavy metal concentrations in drinking water in the United States under the Safe Drinking Water Act. The United Nations International Children's Emergency Fund (UNICEF), the World Health Organization (WHO), the

World Bank, and non-governmental organizations (NGOs) have taken attempts to regulate heavy metal levels in drinking water in underdeveloped countries. Frequent applications of heavy metals in different areas of industry together with their toxic effects on human life have spurred the demand for development of novel techniques for effective removal of heavy metal ions from industrial wastes. Various types of materials such as ion exchange resins, hydrogels, biomimetic compounds, biopolymers, activated carbon, and nano-sized materials have been employed for the removal of these toxic metal ions [3].

The necessity for the development of heavy metal adsorbents with high adsorption capacity, fast adsorption– desorption kinetics, and easy separation and regeneration is rapidly rising. Recently, nanometer-sized metal oxides have been found to be potential heavy metal adsorbents because of large surface areas. However, the major drawback in their practical application is the difficulty and extra cost of separation process upon completion of adsorption. Due to their huge surface area and the unique property of simple and quick separation under external magnetic fields, nanosized magnetic particles are regarded prospective adsorbents for aqueous heavy metals. Iron oxide nanoadsorbents such as magnetite ( $\text{Fe}_3\text{O}_4$ ) have been widely used by researchers for removal of different heavy metal pollutants from environmental or industrial wastes. However, there are technical problems that limit the practical use of iron oxide nanoadsorbents for removal of heavy metal ions from industrial and environmental samples. First is the aggregation tendency of iron oxide magnetic nanoparticles (MNPs) in aqueous solution which greatly weakens their efficiency. Secondly the interactions between unfunctionalized iron oxides and metal ions are often irreversible. To overcome these limitations, immobilization of the polymer shell on the nanoparticles have been explored by researchers. In recent years, several studies have focused on polymeric surface functionalized MNPs because the polymer shell prevents the magnetic core part from aggregation and improves the dispersion stability in aqueous medium. Among the many options for this polymeric shell material, chitosan is a particularly notable biosorbent for heavy metal ions removal, because it has a novel blend of properties like biocompatibility, bioactivity, biodegradability, and renewability [4]. Deposition of mesoporous silica layers on MNPs is considered promising for developing magnetic materials for removal of environmental and protecting the magnetic core from oxidation and leaching [5,6]. The combination of

mesoporous silica with chitosan in nano-sized particle form have been reported to be successful in the pH responsive drug delivery application [7]. Till now the role of the combined coating of mesoporous silica and chitosan on magnetic nanoparticles for as heavy metal adsorbents has not been explored. Based on their pH responsive drug delivery performance, the chitosan-mesoporous silica coated  $\text{Fe}_3\text{O}_4$  nanoparticle can be a promising route for sustainable and efficient and heavy metal adsorption from wastewater.

Therefore, this thesis work consists of the synthesis of mesoporous silica-chitosan coated magnetite nanoparticles and studies its adsorption mechanism of  $\text{Pb}^{2+}$ ,  $\text{Cd}^{2+}$ , and  $\text{As}^{3+}$  in water.

This thesis consists of six chapters. Chapter 2 presents a detailed discussion of synthesis procedure along with morphology and properties of magnetic nanoparticles; structure and importance of mesoporous silica and chitosan as functionalizing substances; adsorption kinetic models and adsorption isotherm models. Chapter 3 contains the details of experimental procedures and information of used chemicals. Chapter 4 presents the results obtained from the experiments and their analysis in order to deduct a conclusion. And finally chapter 5 reports the findings of this study and scope of further study on the achieved progress.



## 2 Chapter 2: Literature Review

Nanotechnology has become an inseparable part of modern living in the last few decades. At present nanotechnology is being utilized in every aspect of our lives ranging from agriculture, medicine, manufacture industry to construction, transport, and clean energy. Nanotechnology is playing a crucial role in sustainable development. The study of nanoparticles is a widely explored area of this field. In the simplest term, nanoparticles are ultrafine particles with a size range of 1 nm to 100 nm. Their size range requires electron microscopes to study their morphology as optical microscope utilizing the visible light of wavelength 400-700 nm cannot be used. Due to their large surface area to volume ratio, nanoparticles demonstrate some unique properties different from their bulk materials. In case of adsorption, the increased surface area of nanoparticles plays a crucial role. Nanoparticles exhibit enhanced efficiency as adsorbent. The potential of different nanoparticles for removal of water contaminants like dyes, antibiotics, and heavy metals are being explored intensively at present. This chapter contains an elaborate discussion focused on magnetic nanoparticles, their synthesis process, properties, surface modification, and their application in heavy metal removal and the related literature.

### 2.1 Magnetic Nanoparticles

In the simplest sense, magnetic nanoparticles are particles of matter containing magnetic elements such as iron, cobalt, nickel and can be manipulated by external magnetic field. The application of magnetic nanoparticles (MNPs) ranges from magnetic fluids, nano-medicine [8], sensing [9], information storage [10], magnetic resonance imaging, and catalysis [11]. When the size of the nanoparticles is below a crucial value, usually between 10-20 nm depending on the substance, the MNPs demonstrate the optimum performance regardless of the nature of application [12]. Due to their size MNPs possess some unique features such as superparamagnetism. These characteristics are discussed in the next section briefly.

The MNPs utilized for this study is magnetite ( $\text{Fe}_3\text{O}_4$ ), a mixer of iron(II) oxide ( $\text{FeO}$ ) and iron(III) oxide ( $\text{Fe}_2\text{O}_3$ ) or hematite.  $\text{Fe}_3\text{O}_4$  is ferrimagnetic with a Curie temperature of 858 K.  $\text{Fe}_3\text{O}_4$  has a cubic inverse spinel group structure, which is made up of a cubic close-packed array of oxide ions in which all of the  $\text{Fe}^{2+}$  ions occupy half of the octahedral sites and the  $\text{Fe}^{3+}$  ions are uniformly distributed among the remaining octahedral sites and tetrahedral sites. The electron spins of the  $\text{Fe}^{2+}$  and  $\text{Fe}^{3+}$  ions in the octahedral sites are connected, while the spins of the  $\text{Fe}^{3+}$  ions in the tetrahedral sites are coupled but anti-parallel to the former, resulting in the ferrimagnetism of  $\text{Fe}_3\text{O}_4$ . The magnetic contributions of both sets are not balanced, and a permanent magnetism exists [13].

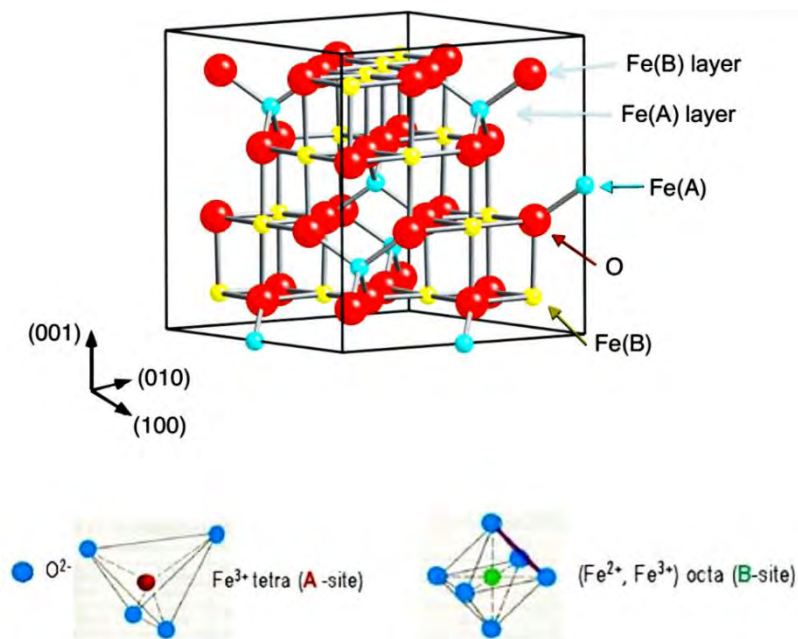


Figure 2–1: Crystal structure of magnetite ( $\text{Fe}_3\text{O}_4$ ).

### 2.1.1 Superparamagnetism

Small ferromagnetic or ferrimagnetic nanoparticles exhibit a unique kind of magnetism called superparamagnetism. Magnetization can randomly switch direction in nanoparticles under the effect of temperature. The Néel relaxation time is the amount of time between two flips. When the period used to test the magnetization of nanoparticles is significantly longer than the Neel relaxation time in the absence of external magnetic field, their magnetization seems to be in average zero. This state is designated as superparamagnetism state. An external magnetic field can magnetize the nanoparticles in

this condition, analogous to a paramagnet. But their magnetic susceptibility is substantially higher. Because the possibility of agglomeration is low at ambient temperature, superparamagnetic nanoparticles are particularly appealing for a wide range of applications.

Isolated nanoparticles have a constant magnetic moment and act like a large paramagnetic atom, with negligible remanence and coercivity. The magnetization of nanoparticles is thought to be the sum of all the individual magnetic moments carried by the nanoparticle's atoms. The magnetism has a limited probability of flipping at a certain temperature and the Neel relaxation time  $\tau_n$  is represented by the Neel-Arrhenius equation mentioned below.

$$\tau_n = \tau_0 \exp\left(\frac{KV}{k_B T}\right) \dots \dots \dots \text{Equation 2.1}$$

Here  $\tau_0$  is the attempt time individual to the material, K is the nanoparticle's magnetic anisotropy energy density and V is the volume of the nanoparticle,  $k_B$  is the Boltzmann constant, and T is the temperature. Since  $\tau_n$  is exponentially dependent on the particle volume, flipping probability is only considerable at the nanoscale.

Table 2–1: Estimated maximum single domain size for different magnetic materials [12].

Material	Critical diameter of a spherical particle, $D_c$ nm
FCC Co	7
Fe	15
Ni	55
Fe <sub>3</sub> O <sub>4</sub>	128

Another term associated with superparamagnetism is the blocking temperature which is defined as the temperature at which  $\tau_n = \tau_m$ ,  $\tau_m$  being the measurement time. The nanoparticle magnetization will flip multiple times throughout the measurement if  $\tau_m \gg \tau_n$  and will appear to be superparamagnetic. This situation occurs when the measuring temperature is below the blocking temperature. Blocking temperature  $T_B$  can be represented by the following equation.

$$T_B = \frac{KV}{k_B \ln\left(\frac{\tau_m}{\tau_n}\right)} \dots \dots \dots \text{Equation 2.2}$$

**2.1.1.1 Effect of Magnetic Field- Langevin Function**

Superparamagnetic nanoparticles align their magnetic moment to an externally applied magnetic field resulting in net magnetization. The magnetizing curve is represented by the Langevin function given below.

$$M = M_o \left[ \coth(\beta\mu H) - \frac{1}{\beta\mu H} \right] \dots \dots \dots \text{Equation 2.3}$$

Where M is the magnetization, H is the applied field,  $\mu$  is the magnetic moment of the nanoparticle,  $\beta = \frac{1}{k_{\beta}T}$  where  $k_{\beta}$  is the Boltzmann constant, and T is the temperature. The magnetization curve of superparamagnetic nanoparticles does not contain a loop indicating zero magnetic remanence.

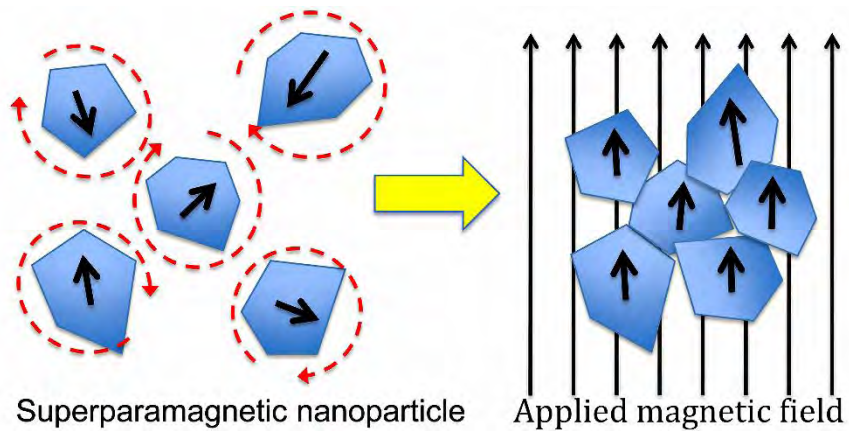


Figure 2–2: Magnetization of superparamagnetic nanoparticles.

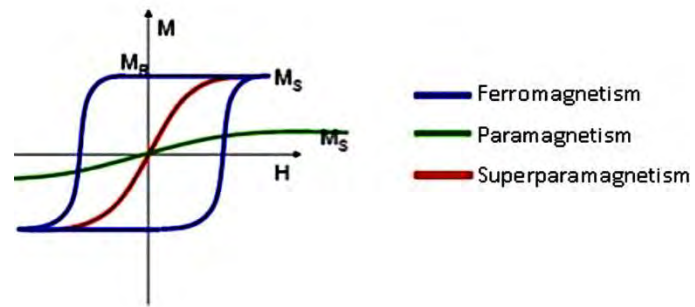


Figure 2–3: Comparison of ferromagnetic, paramagnetic, and superparamagnetic magnetization curves.

### 2.1.2 Synthesis of Magnetic Nanoparticle

Magnetic Fe<sub>3</sub>O<sub>4</sub> nanoparticles have been produced in a variety of compositions and phases. Many research over the last few years have reported effective synthesis pathways to shape-controlled, extremely stable, and monodisperse magnetic nanoparticles. Co-precipitation, thermal decomposition, micelle synthesis, hydro/solvothermal synthesis, and laser pyrolysis procedures are just a few of the processes that may be used to make MNPs. A brief discussion of the most common synthesis methods such as co-precipitation, thermal decomposition, solvothermal, microemulsion, etc. is presented in this section.

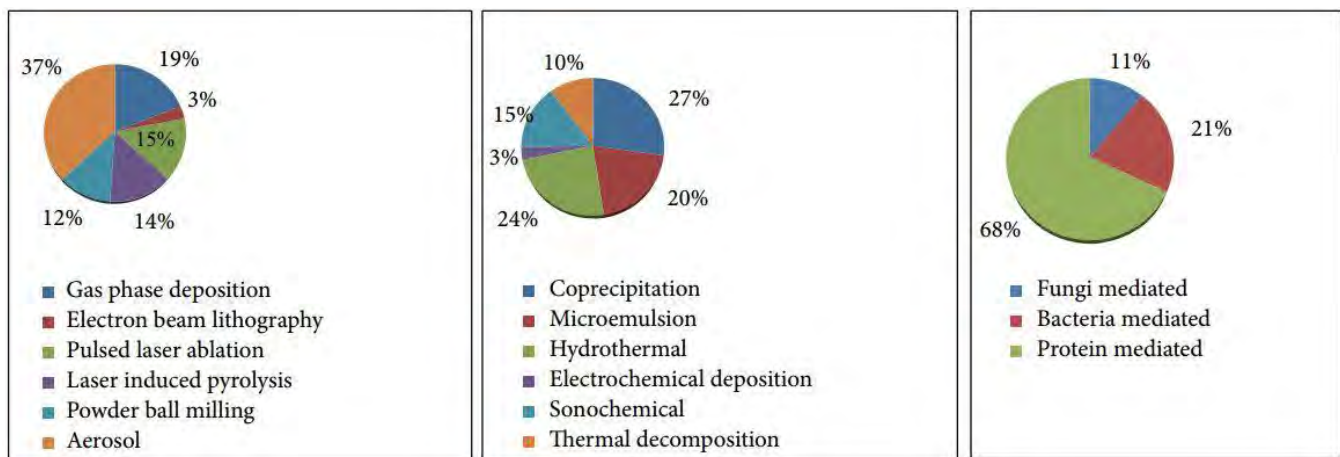


Figure 2–6: Overview of synthesis methods for Fe<sub>3</sub>O<sub>4</sub> MNPs.

#### 2.1.2.1 Co-precipitation

Co-precipitation method consists of adding a base to aqueous Fe<sup>2+</sup>/Fe<sup>3+</sup> salt solutions under inert atmosphere at ambient temperature or at increased temperature. It is a simple and practical approach to synthesis either Fe<sub>3</sub>O<sub>4</sub> or γ-Fe<sub>2</sub>O<sub>3</sub>. The following equation describes the chemical reaction occurring during co-precipitation process.



The kind of salts utilized (e.g. chlorides, sulfates, nitrates), the Fe<sup>2+</sup>/Fe<sup>3+</sup> ratio, the reaction temperature, the pH value, and the ionic strength of the medium determine the size and shape of the MNPs [14]. The

regulation of particle size and consequently achieving a narrow particle size distribution is a problem in the co-precipitation synthesis of  $\text{Fe}_3\text{O}_4$  MNPs. It is evident from equation 2.2 that the blocking temperature is determined by particle size. A broad particle size distribution will result in a wider range of blocking temperature, resulting in undesired magnetic behavior. Therefore, the co-precipitation method is sometimes rendered unsuitable in applications regarding monodisperse MNPs as it has the tendency to produce polydisperse MNPs. Organic compounds have recently been reported to be used as stabilizing and/or reducing agents in the successful manufacture of monodisperse MNPs of various sizes. Magnetite nanoparticles with sizes of 4–10 nm can be stabilized in an aqueous solution of 1 wt% polyvinylalcohol (PVA) [15]. Several organic anions, such as carboxylate and hydroxyl-carboxylate ions, have been researched extensively for their influence on the production of MNPs but the ideal choice for stabilizing  $\text{Fe}_3\text{O}_4$  is reported to be oleic acid [16]. The effect of these organic ions can be explained by two opposing mechanisms- chelation of the metal ions preventing nucleation leading to larger particles, and the other one is accumulation of additive on nuclei inhibiting particle growth [12].

#### ***2.1.2.2 Thermal Decomposition***

Thermal decomposition is the process of synthesizing MNPs from the decomposition of an organo-metallic precursor at high temperature. Thermal decomposition method was initially used for producing high-quality semiconductor nanocrystals and later was successfully utilized for synthesizing MNPs [17]. The thermal breakdown of organometallic compounds in high-boiling organic solvents containing stabilizing surfactants may essentially be used to make monodisperse magnetic nanocrystals with lower sizes [18–21]. The organometallic precursors varies from Fe-acetylacetonates [ $\text{Fe}(\text{acac})_n$ ] ( $n = 2$  or  $3$ , acac = acetylacetonate) [22], Fe(III) oleate [23–25], and carbonyls [26].

Fatty acids [27], oleic acid [23–26], and hexadecylamine [28] are common surfactants used in the thermal decomposition process. The size and shape of MNPs are controlled by the ratios of the initial reagents which are the organometallic compounds, surfactant, and solvent [29]. The reaction time, temperature, and aging time also plays a role in rendering the morphology of the MNPs.

In case of zero-valent organometallic precursor such as iron pentacarbonyl, a two-step procedure is utilized where the precursor first decomposes in a mixture of octyl ether and oleic acid at 100°C followed by the addition of trimethylamine oxide (CH<sub>3</sub>)<sub>3</sub>NO to form  $\gamma$ -Fe<sub>2</sub>O<sub>3</sub> nanocrystals with a size of approximately 13 nm [28]. Use of precursors containing cationic metal center directly produces Fe<sub>3</sub>O<sub>4</sub>. Highly monodisperse Fe<sub>3</sub>O<sub>4</sub> nanocrystals with tunable sizes and shapes over a wide size range (3–50 nm) and shapes of dots and cubes could be synthesized [19].

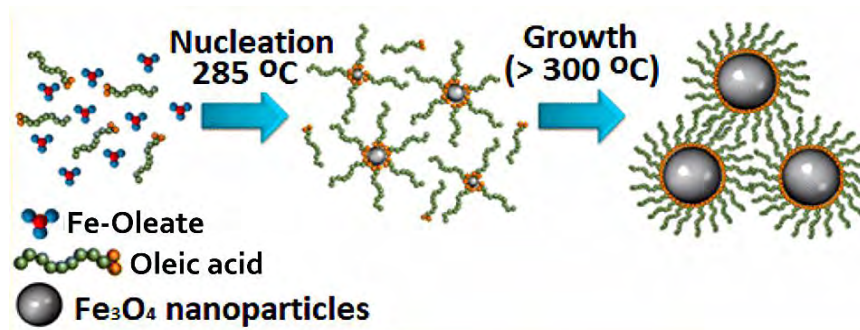


Figure 2–7: Synthesis of Fe<sub>3</sub>O<sub>4</sub> MNPs via thermal decomposition method.

The LaMer mechanism is used to describe this process. A supersaturated solution causes a brief burst of nucleation. Following that, particles expand slowly without any more nucleation, resulting in a full separation of nucleation and growth [30]. MNPs synthesized via thermal decomposition are coated with organic substance and hydrophobic in nature i.e., they are not soluble in water. But water soluble MNPs are preferred for practical application. Therefore, the MNPs have to be subjected to a phase transformation step before utilizing them for the actual purpose. Phase transformation procedures are discussed further in the later part of this chapter.

### 2.1.2.3 Microemulsion

A microemulsion is defined as the thermodynamically stable isotropic dispersion of two immiscible liquids in which an interfacial coating of surfactant molecules stabilizes the microdomain of one or both liquids [31]. The aqueous phase of water-in-oil microemulsions is dispersed as microdroplets of 1–50 nm diameter in the hydrocarbon phase, surrounded by a monolayer of surfactant molecules. The molar

ratio of the water-oil mixture regulates the size of the droplet [32]. When two identical water-in-oil microemulsions with the appropriate reactants are mixed together, the microdroplets collide, consolidate, and break again, eventually forming a nanosized precipitate in the micelles [33]. Technically, a microemulsion can be employed as a nano-reactor to produce nanoparticles. The MNPs can be separated from the microemulsion by adding acetone or ethanol and centrifuged or filtered out. Woo et al. produced iron oxide nanorods via a sol-gel reaction in reverse micelles formed by oleic acid and benzyl ether, using  $\text{FeCl}_3 \cdot 6\text{H}_2\text{O}$  as iron source and propylene oxide [34]. The drawbacks of microemulsion technique for synthesizing MNPs are polydispersity, low yield, and narrow time window for work.

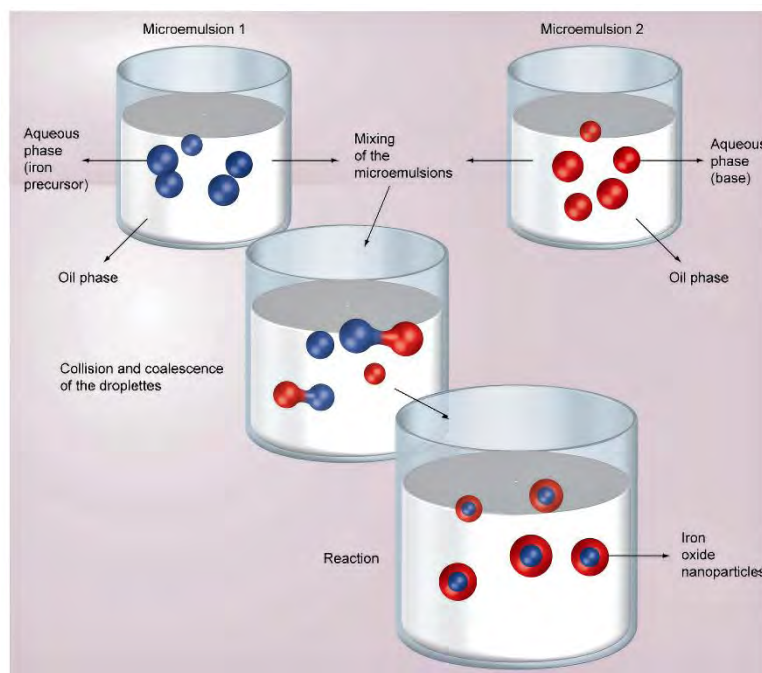


Figure 2–8: Synthesis of MNPs via microemulsion method.

#### 2.1.2.4 Hydro/Solvothermal

Hydrothermal or solvothermal procedure is the formation of nanocrystals at the interfaces of the liquid, solid, and solution phases by a liquid–solid–solution reaction. The process is driven by a general phase transfer and separation mechanism [35,36]. Decomposition of precursors in high boiling point solvent is a common procedure for semiconductor nanocrystal production [37]. An alternative to using high-temperature solvents, which may be both dangerous and expensive, is to employ more common solvents



that are restricted by their low boiling temperatures. To overcome this obstacle, solvents can be heated in a sealed autoclave. The autogenous pressure then significantly surpasses the ambient pressure, boosting the solvent's boiling point [38]. The difference between hydrothermal and solvothermal is simply the presence of water in the reaction mixture. There are two basic ways for magnetite to evolve via hydrothermal route- hydrolysis and oxidation or neutralization of mixed metal hydroxides [39]. The first method only uses ferrous salts for the reaction. Polyethylene glycol (PEG) has been reported to be an effective high-boiling point reducing agent as well as surfactant in producing monodisperse MNPs [40–43].

Table 2-2 summarizes the benefits and drawbacks, and required conditions of the four synthetic approaches outlined previously.

Table 2–2: Comparison between chemical synthesis methods of MNPs.

<b>Process</b>	<b>Maximum Reaction Temperature, °C</b>	<b>Synthesis condition</b>	<b>Dispersity</b>	<b>Shape control</b>	<b>Yield</b>
Co-precipitation	90	Ambient	Polydisperse	Poor	High
Thermal decomposition	320	Inert atmosphere	Highly monodisperse	Very good	High
Microemulsion	50	Ambient	Polydisperse	Good	Low
Hydro/Solvothermal	220	High pressure	Monodisperse	Very good	Medium

Apart from the above common methods, there are other various procedures that have been reportedly employed to generate MNPs with different outcomes. Organometallic decomposing via sonolysis have been studied and the results were satisfactory with high magnetization properties and crystallinity [44,45]. Gas–aerosol method utilizes spraying mixture of ferric salts and reducing agents in organic solvents in reactors and different sizes and shapes can be achieved from using different precursors [46–48]. MNPs can also be synthesized by oxidation of iron electrode in electrochemical deposition process and the morphology can be controlled by adjusting the current density [49–51].

### 2.1.3 Phase Transfer of Magnetic Nanoparticles

It is apparent from the previous discussion that synthesis of MNPs in organic solvents is the more efficient route as it delivers the proper shape, size, and homogeneity in high quantity and high yield. In organic methods high concentrations of reactants can produce high-quality nanocrystals with well-defined structure and controlled size, but aqueous techniques typically employ low concentrations of reactants due to ionic interactions [52]. MNPs synthesized via these routes are coated with organic substances which makes them hydrophobic. But hydrophilic MNPs are required for numerous applications, including catalysis, diagnostics, medication administration, and bio-labelling let alone the water treatment sector. Various efforts have been made over the recent years to find an effective method for transferring hydrophobic nanocrystals into hydrophilic while maintaining their original physical and chemical characteristics. The reported methods can be divided into two main categories-

1. Ligand exchange- replacing the initial organic ligand on the surface of the MNPs with a secondary surfactant like metal chalcogenide [53], 3,4-dihydroxyhydrocinnamic acid [54], or polyelectrolyte [55].
2. Encapsulation of nanocrystals into a hydrophilic shell- surfactant bilayers [56], amphiphilic polymer shell [57], or silica shell [58].

Wu et al. reported a relatively fast, bio-compatible, and cheaper method of phase transfer of oleic acid capped MNPs and other semiconducting nanocrystals by employing sodium oleate, hexadecyltrimethylammonium bromide (CTAB), and dopamine [59].

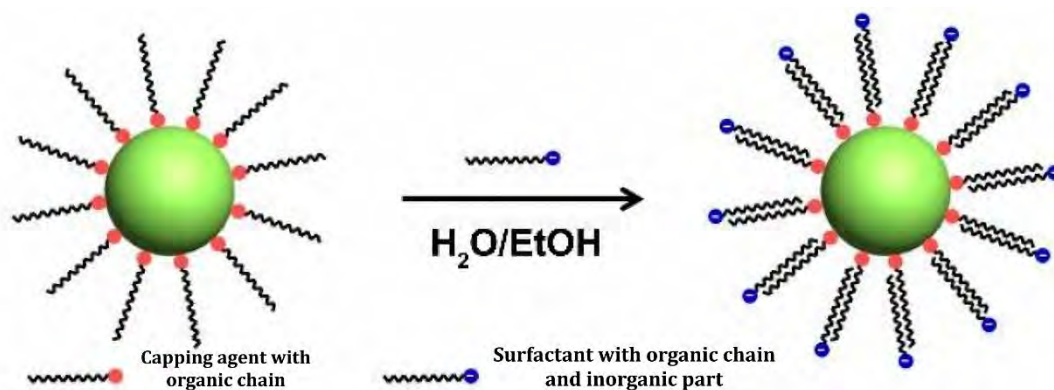


Figure 2–9: Phase transfer of hydrophobic MNPs.

## 2.2 Surface Functionalization of Magnetic Nanoparticles

The inherent instability of MNPs over extended periods of time is an inescapable challenge. To decrease the energy associated with the high surface area to volume ratio of nanosized particles, MNPs tend to form agglomerates which consequently reduces their efficiency where surface area is crucial such as adsorption applications. Furthermore, bare MNPs are chemically active and readily oxidized in air, losing their magnetic properties and dispersibility in the process. As a result, developing protective measures to maintain the integrity of MNPs against degradation during or after manufacturing is critical for many applications. Grafting or coating with organic species, such as surfactants or polymers, or coating with an inorganic layer, such as silica or carbon, are examples of these techniques. It's worth noting that in many circumstances, the protective shells may be employed for additional functionalization depending on the desired application. Particular components, such as catalytically active species, diverse medicines, specific binding sites, or other functional groups are employed for surface functionalization. This is particularly true for adsorption application. Surface functionalization creates opportunity for higher rate of adsorption and also provides way for recovery of the used particle.

All of the protection measures result MNPs with a core-shell structure, in which the naked magnetic nanoparticle serves as the core and is surrounded by a shell that protects it from the environment. Coating substances can be categorized into two types- firstly organic shells, such as surfactants and polymers [3,60–63]. And secondly inorganic components, such as silica [64,65], carbon [66], precious metals [67,68], or oxides [69]. Magnetic nanoparticles can also be dispersed/embedded within a dense matrix, such as polymer, silica, or carbon, to produce composites, which avoids or reduces agglomeration and oxidation. In such case, the MNPs are locked in space relative to each other whereas independently coated nanocrystals are readily miscible and stable in a range of environments.

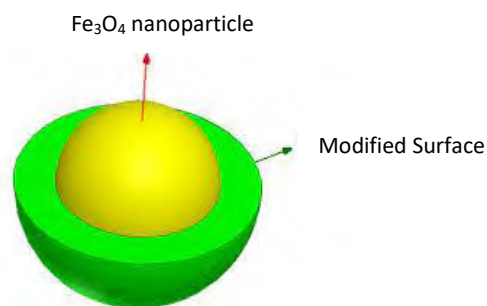


Figure 2–11: Illustration of modified surface of MNPs.

Table 2–3 contains a brief overview of some of the reported study regarding surface functionalization of MNPs specifically for heavy metal adsorption.

Table 2–3: Reported studies of surface functionalization for heavy metal removal.

<b>Synthesis Method</b>	<b>Coating agents</b>	<b>Surface functionalized group</b>	<b>Metal removed</b>	<b>Ref.</b>
Thermolysis	Dimercaptosuccinic acid	Thiol group	Hg(II), Ag(I), Pb(II), Cd(II), Tl	[70]
Thermolysis	Ethylenediamine	Amine group	Cr(III), Co(II), Ni(II), Cu(II), Cd(II), Pb(II), As(III)	[71]
Co-precipitation	Succinic acid	Carboxylic group		
Co-precipitation	Humic acid	Carboxylic and phenolic group	Hg(II), Pb(II), Cd(II), Cu(II)	[60]
Co-precipitation sol-gel process using sodium silicate (Fe <sub>3</sub> O <sub>4</sub> @SiO <sub>2</sub> )	(3-aminopropyl) trimethoxysilane	(3-aminopropyl) trimethoxysilane	Pb(II), Cd(II), Cu(II)	[72]
Co-precipitation hydrolysis of TEOS, (Fe <sub>3</sub> O <sub>4</sub> @SiO <sub>2</sub> )	Salicylic acid functionalized silica	Carboxylic group	Cu(II), Cd(II), Ni(II), Cr(III)	[65]
Co-precipitation	Carboxymethylated chitosan	Amino and hydroxyl groups	As(III)	[73]

### 2.2.1 Surface Modification with Mesoporous Silica

Surface modification is an essential part in developing MNPs for the purpose of adsorption of heavy metals. It not only provides larger quantity of adsorption sites but also protects the magnetic core from corrosion and degradation from the outer environment. Leaching or degradation of the core materials can consequently affect the magnetic properties of the adsorbent which is crucial for the ease of separation upon completion of the adsorption process. In order to develop a sustainable adsorbent, it has to be ensured that the adsorbed metal ions can be recovered from the MNPs and the MNPs can be reused. Surface modification is also important for this part of the process since the bonding between bare MNPs surface and metal ions would be irreversible if there occurs any. Several surface modification techniques have been discussed in the previous section. Among all the substances considered till date for MNPs surface modification, silica ( $\text{SiO}_2$ ) and mesoporous silica have been reported as one of the most efficient. Silica provides an excellent protection to the  $\text{Fe}_3\text{O}_4$  core from corrosive and oxidizing environments. In comparison to organic coating materials,  $\text{SiO}_2$  is stable under acidic circumstances and inert to redox processes, making it a suitable shell for protecting the inner magnetite core. Silica coating can also be a better site for further functionalizing with different ligands [65]. The presence of surface hydroxyl groups in the  $\text{SiO}_2$  covering shell makes further functionalization of magnetite nanoparticles easier [64].

Mesoporous silica is a specific structure of  $\text{SiO}_2$  with special characteristics. According to IUPAC (International Union of Pure and Applied Chemistry), mesoporous materials are those with pore sizes ranging from 2 to 50 nm and an ordered arrangement of pores, resulting in an ordered structure [74]. In 1992, Mobil Research and Development Corporation was the first to manufacture mesoporous solids from aluminosilicate gels via liquid crystal template mechanism [75]. The pore size and arrangement of mesoporous  $\text{SiO}_2$  can be regulated by the choice of the surfactant and reaction conditions. Depending on pore size and arrangement, mesoporous  $\text{SiO}_2$  can be classified into different types- MCM-41, MCM-48, MCM-50, SBA-11, SBA-12, SBA-15, SBA-16, etc. The SBA class possess larger pores and thicker walls than the MCM class [75]. The MCM class, particularly the MCM-41 has been widely reported as an efficient drug carrier [76,77] and adsorbent [6]. A major advantage of mesoporous  $\text{SiO}_2$  over typical  $\text{SiO}_2$  is that it provides larger surface area for ligand attachment due to the porous structure.

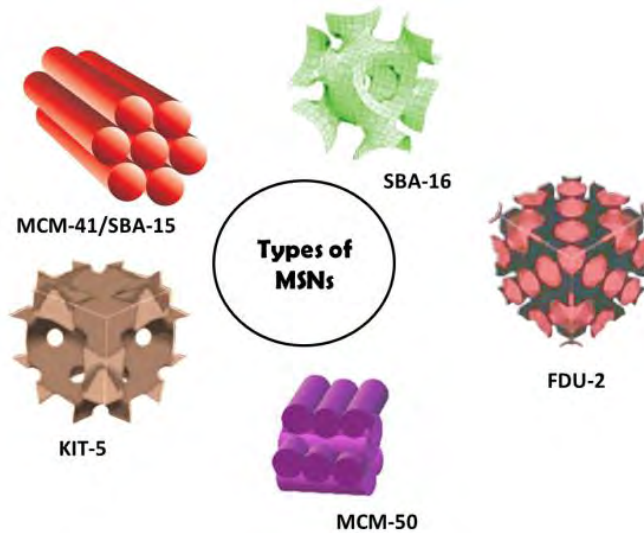


Figure 2–13: Different types of mesoporous SiO<sub>2</sub> structures.

### 2.2.2 Synthesis of Mesoporous Silica

Mesoporous silica is synthesized via a liquid crystal template method, which involves the hydrolysis and condensation of silica from tetraethyl orthosilicate (TEOS) on the surface of surfactant micelles. CTAB is used as the surfactant and it generates micelles with hydrophilic tails in the core. The micelles then accumulate on the MNPs surface. Upon hydrolysis of TEOS the hydrophilic positively charged monomer is attracted to the negatively charged hydrophilic head of CTAB. Eventually a shell of TEOS is formed around the MNP. When the CTAB is removed it leaves a mesoporous structure of SiO<sub>2</sub> on the MNP surface.

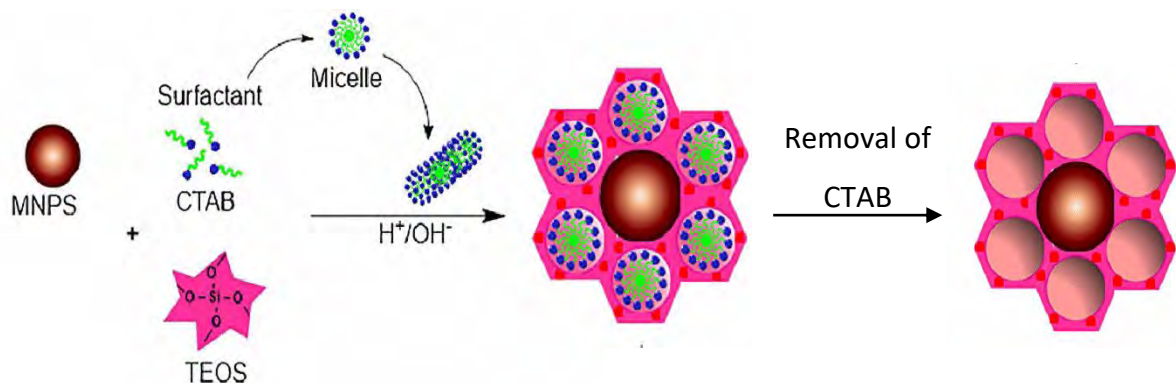


Figure 2–15: Synthesis of mesoporous SiO<sub>2</sub> on MNPs.

The removal of the surfactant or template is an important step in the synthesis of mesoporous SiO<sub>2</sub> coating. Several methods have been utilized for removal of template. Traditional calcination under air at 550°C is the most typical procedure for removing templates. Despite the fact that templates can be completely removed from pores, calcination has a number of significant disadvantages. These include significant framework shrinkage, collapse of the ordered structure, reduction of silanol (–Si–O–H–) concentrations on the pore wall, generation of large amounts of CO<sub>2</sub> and organic amine compounds, the presence of carbon deposits, and elimination of organic functionalities [78]. Presence of silanol group is required for further functionalization as they act as binding sites. Another crucial reason behind the unsuitability of calcination method in case of MNPs is that calcination temperature can easily exceed their blocking temperature and make the superparamagnetism characteristic obsolete. For this particular application solvent extraction or ion exchange method is preferred. Solution of ammonium nitrate (NH<sub>4</sub>NO<sub>3</sub>) has been reported as a fast and efficient medium for solvent extraction of CTAB [79,80]. The NH<sub>4</sub><sup>+</sup> cations create silanol groups on the surface of the mesoporous silica [79] which would play a crucial role in modifying the surface with chitosan. The chitosan modification is discussed further in the next section.

### 2.3 Chitosan

Chitosan is a linear polysaccharide made up of randomly placed deacetylated D-glucosamine (C<sub>6</sub>H<sub>13</sub>NO<sub>5</sub>) and acetylated N-acetyl-D-glucosamine (C<sub>8</sub>H<sub>15</sub>NO<sub>6</sub>). Chitosan can be derived by deacetylating chitin, a structural component of crustacean exoskeletons and fungi cell walls [81]. The acid dissociation constant, pK<sub>a</sub> value of the amino group in chitosan is 6.5, which causes substantial protonation in neutral solution, which increases with increasing acidity [82]. This makes chitosan an excellent pH responsive substance delivery system. High biocompatibility of chitosan has caused it to emerge as an ideal choice for pH responsive smart drug delivery system [83]. Chitosan has been studied extensively as a delivery system for anticancer drugs doxorubicin [82,83], raloxifene hydrochloride [84], and curcumin [85]. The same principal of pH stimulated delivery can be applied in developing sustainable adsorbent.

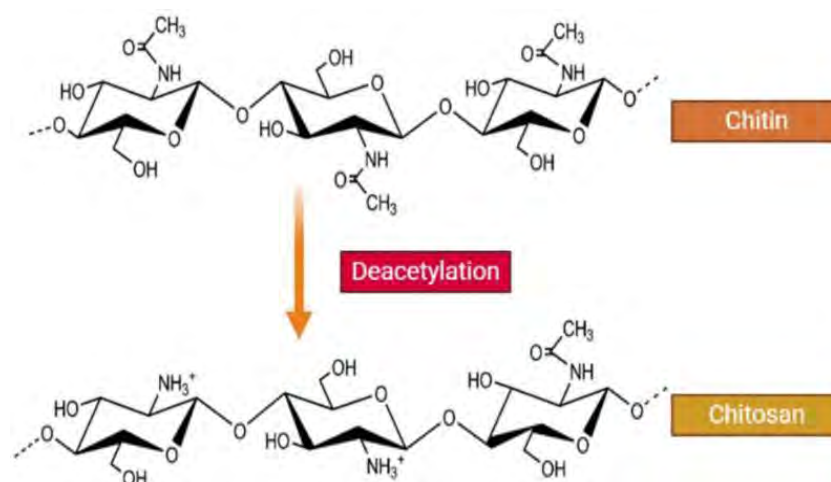


Figure 2–16: Derivation of chitosan from chitin.

### 2.3.1 Chitosan Grafting on Mesoporous Silica

The combined system of mesoporous silica and chitosan has potential application in fields of biomedicine, drug delivery and water treatment. Extensive research has been carried out in the recent decade to evaluate the efficiency of mesoporous silica–chitosan system in pH responsive drug delivery application with outstanding results. The popularity of this combination can be attributed to the fact that chitosan can be easily grafted on to mesoporous silica without the need of any expensive materials or equipment. The chitosan coating binds to the mesoporous silica surface with the help of the hydrogen bonding between the surface silanol groups and the amine groups on chitosan [80]. The porous structure of the SiO<sub>2</sub> acts as an ideal drug reservoir. A short list of the recently published work based on mesoporous silica and chitosan drug delivery system is given in table 2–4.

Table 2–4: Short list of recent works on mesoporous SiO<sub>2</sub>–chitosan drug delivery system.

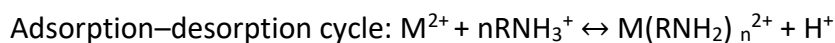
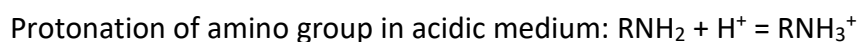
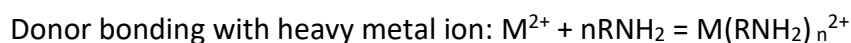
Loaded drug	Drug type	Reference
Pheophorbide A and doxorubicin	Anticancer	[86]
Methotrexate	Anti-breast cancer drug	[87]
Azoxystrobin	Pesticide	[88]
Capecitabine	Colorectal cancer	[89]
Benznidazole	Antiparasitic	[90]
Ibuprofen	Nonsteroidal anti-inflammatory	[91]



Keshavarz et al. has combined MNPs with mesoporous SiO<sub>2</sub>–chitosan coating to develop a drug delivery system that can also be used in hyperthermia applications [92]. The use of mesoporous SiO<sub>2</sub>–chitosan system in the heavy metal removal application has not been studied as extensively as the drug delivery application. Mainly because of the difficulty of separating the adsorbent from the aqueous medium. Nevertheless, some studies have explored the potential of mesoporous SiO<sub>2</sub>–chitosan for the recovery of rare earth elements [93], uranium and strontium removal [94], dye removal [95], lead adsorption [96], and rhenium adsorption [97]. However, the potential of magnetic mesoporous SiO<sub>2</sub>–chitosan nanoparticle for heavy metal removal is yet to be explored. Based on the results of the previously reported studies, MNPs coated with mesoporous SiO<sub>2</sub>–chitosan should act as an efficient and sustainable adsorbent for heavy metals from wastewater. Exploring that possibility is the objective of this research work.

### 2.3.2 Adsorption and desorption mechanism of chitosan

Chitosan composites in both bulk and nanoscale, magnetic or non-magnetic have been studied by several research groups for removal of heavy metals from water. The reported forms of chitosan adsorbents are encountered in a variety of forms such as chitosan nanoparticles [98], zero-valent iron encapsulated chitosan beads [99], TiO<sub>2</sub>-impregnated chitosan bead [100], metal oxide impregnated chitosan beads [4,101–103], metal doped chitosan hydrogels [104], and chitosan–transition metal ions complexes [105], etc. The amide groups on glucosamine in chitosan can chelate heavy metal ions, allowing it to absorb them. The nonprotonated amino group develops a donor bond with positively charged heavy metal ions through the unshared electron pair. This is the mechanism of the adsorption part. If the pH of the medium is lowered i.e., concentration of H<sup>+</sup> ion is increased, the amino group undergoes protonation and releases the metal ion into the medium triggering the desorption mechanism. The adsorption and desorption process can be expressed with the following reactions.



Here M denotes the heavy metal ion. Figure 2–12 illustrates the adsorption-desorption process of heavy metal by chitosan in a precise manner.

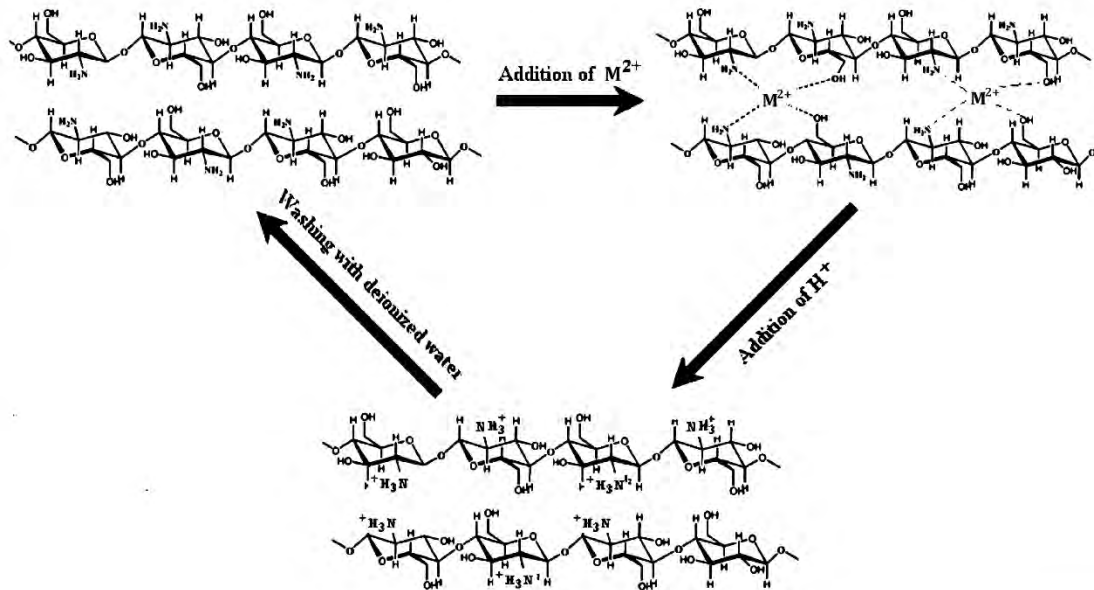


Figure 2–19: Adsorption-desorption mechanism of heavy metal by chitosan.

## 2.4 Heavy metal pollution of water

Human activities have a variety of effects on the environment. The discharge of untreated industrial and domestic effluents has specific role in polluting aquatic ecosystems. according to the World Health Organization air pollution, arsenic (As), asbestos, benzene, cadmium (Cd), dioxin and dioxin-like chemicals, excess fluoride, lead (Pb), mercury (Hg), and toxic pesticides are among the top 10 compounds of most health concern [106]. Prolonged exposure to hazardous metals including Cd, Pb, and Hg, as well as metalloids like As, has been associated to symptoms that are comparable to those of serious illnesses such as Alzheimer’s and Parkinson’s diseases [107,108]. Metal-derived reactive oxygen species can interact with DNA and nuclear proteins, resulting in carcinogenesis [109]. The chemical properties and metal speciation, as well as the biological traits of creatures in risk, all influence metal toxicity level [110]. Cadmium is listed as a human carcinogen by the United States Environmental Protection Agency (USEPA), and it is known to cause health problems including bone demineralization

either by direct bone destruction or through renal failure [111]. The International Agency for Research on Cancer (IARC) has classified Cd as a Category I carcinogen, while the USEPA has classified it as a Group B-I carcinogen [112]. Although many of these heavy metals are hazardous, there are other metals and metalloids that are hazardous but do not fall into the heavy metal category such as beryllium (Be) [113]. As, Cd, and Pb are the most typically detected metals of concern in wastewaters [114]. The increased demand for metallic items, along with inadequate treatment of industrial effluent, encourages indiscriminate hazardous metal pollution of water. Toxic metals such as Cd, Pb, and Hg are almost always detectable in municipal wastewater treatment works influents, although at varied quantities owing to a variety of circumstances such as the treatment station's location and industrial activity [115]. Allowable safe limits in wastewater and drinking water depends on level of toxicity of the metals. Table 2–5 and table 2–6 contains the designated amount of heavy metal in wastewater and drinking indicated by authorities.

Table 2–5: World health organization (WHO) permissible limit of heavy metals in wastewater.

<b>Heavy metal</b>	<b>Permissible limit (ppm)</b>
Cadmium	0.003
Lead	0.01
Mercury	0.001
Ni	0.02

Table 2–6: WHO designated permissible heavy metal limit in drinking water.

<b>Heavy Metal</b>	<b>Main Sources</b>	<b>Permissible limit (ppb)</b>
Lead (Pb)	Batteries, solder, alloys, cable sheathing pigments, rust inhibitors, ammunition, glazes, and plastic stabilizers.	10
Cadmium (Cd)	Batteries, paints, steel industry, plastic industries, metal refineries, and corroded galvanized pipes.	3
Arsenic (As)	Electronics and glass production.	10
Mercury (Hg)	Electrolytic production of chlorine and caustic soda, runoff from landfills and agriculture, electrical appliances, Industrial and control instruments, laboratory apparatus, and refineries.	6
Nickel (Ni)	Stainless steel and nickel alloy production.	70
Chromium (Cr)	Steel and pulp mills and tanneries.	5

## 2.5 Techniques for heavy metal removal from water

Various techniques have been developed over the years for removal of heavy metal ions from wastewater. Chemical precipitation, ion exchange, adsorption, membrane filtration, electrochemical treatment technologies, and other ways are utilized to remove heavy metal ions. The major methods are shortly discussed in this section to convey their basic mechanism along with advantages and disadvantages over each other.

### 2.5.1 Chemical precipitation

Chemical precipitation is the process of chemicals react with heavy metal ions to generate insoluble precipitates which can be separated from the water via sedimentation or filtering. The treated water is then decanted and released or reused as needed. Hydroxide precipitation and sulfide precipitation are two common chemical precipitation methods along with heavy metal chelating precipitation.

The solubility of heavy metal hydroxides is minimal in the pH range of 8.0 to 11.0. The insoluble hydroxides can be removed by flocculation and sedimentation. Lime is the preferred choice of base used in hydroxide precipitation at industries because of low cost, availability and ease of operation [116]. Despite the low cost the limitations of hydroxide precipitation include production of large volumes of low density sludge, inability to remove more than one metal at a time, and inhibition by complexing agents [111]. Major advantages of sulfides precipitation over hydroxide precipitation is the much lower solubility of the metal sulfide precipitates and they are not amphoteric. Metal sulfide sludges are also denser, making removal easier. However, this process possesses the danger of toxic H<sub>2</sub>S fume production in acidic condition [111]. The possibility of overcoming these limitation by precipitating heavy metals through chelation with organic compounds has been investigated by several research groups [117–119].

### 2.5.2 Ion exchange

Ion exchange procedure is based on the ability of natural or synthetic resin to exchange cations with the heavy metals ions in the wastewater. Strongly acidic resins with sulfonic acid groups (–SO<sub>3</sub>H) and mildly acidic resins with carboxylic acid groups (–COOH) are the most frequent cation exchangers. Synthetic resins are common choice as they have high rate of removal efficiency [120]. The removal efficiency is regulated by the solution pH, temperature, initial metal concentration, ionic charge, and contact time

[121]. The potential of natural resins like zeolites and silicate minerals has been explored by some researchers [122,123].

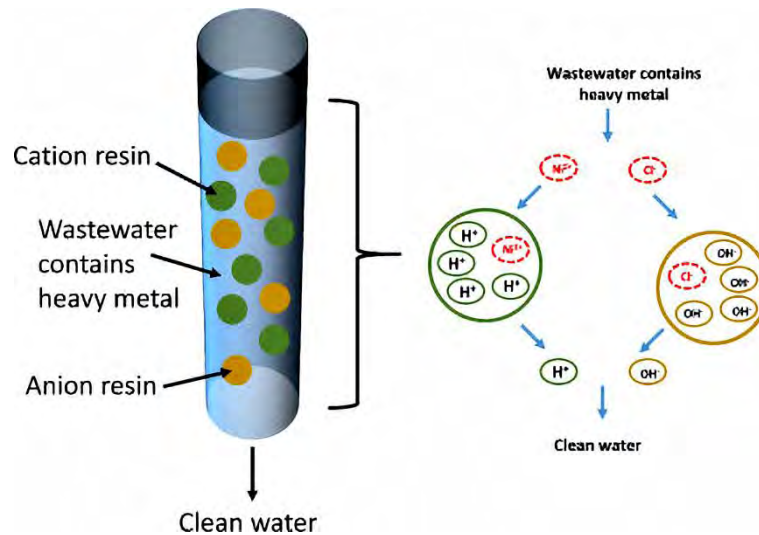


Figure 2–20: Ion exchange process of heavy metal removal.

### 2.5.3 Membrane filtration

Membrane filtering methods using various types of membranes have a lot of potential for heavy metal removal due to their high efficiency, and ease of use. Ultrafiltration, reverse osmosis, nanofiltration, and electrodialysis are the membrane technologies used to remove metals from wastewater.

Ultrafiltration (UF) is a membrane technology for removing dissolved and colloidal particles at low transmembrane pressures. Micellar enhanced ultrafiltration (MEUF) and polymer enhanced ultrafiltration (PEUF) was proposed since pore sizes of UF membranes are larger than dissolved metal ions. The addition of surfactants to wastewater is the basis of MEUF. Surfactant molecules create micelles, which can bind metal ions and form massive metal-surfactant complexes. These are filtered by the UF membrane. MEUF effectivity relies on characteristics and concentrations of the metals and surfactants, solution pH, ionic strength, and parameters related to membrane operation [111]. PEUF combines metallic ions with a water-soluble polymer to generate a macromolecular complex that is retained by the UF membrane. Metal and polymer type, metal-to-polymer ratio, pH, and the presence

of additional metal ions in the solution are the key factors that influence PEUF performance [111]. A semi-permeable membrane is used in the reverse osmosis (RO) process, which allows the filtered fluid to flow through while rejecting impurities. The main disadvantage of RO is the high power consumption caused by the high pumping pressures and the membrane repair. Nanofiltration (NF) is a procedure with characteristics between ultrafiltration (UF) and reverse osmosis (RO). Another membrane procedure for separating ions across charged membranes from one solution to another is electrodialysis (ED) which is driven by an electric field. The membrane can be of cation-exchange type or anion-exchange type. This method has been widely utilized to make drinking and process water from brackish water and seawater [124].

#### **2.5.4 Coagulation and flocculation**

Heavy metals are removed from wastewaters via coagulation and flocculation, followed by sedimentation and filtering. Hydrophobic colloids and suspended particles are the primary targets of coagulation. The action of polymers to build bridges between flocs and link the particles into huge agglomerates or clumps is known as flocculation. Coagulation and flocculation, in principle, is unable to fully treat heavy metal wastewater. As a result, alternative procedures must be used after coagulation flocculation.

#### **2.5.5 Flotation**

Flotation, which originated in mineral processing, is used to separate heavy metals from a liquid phase through bubble attachment. The major flotation procedures for removing metal ions from solution include dissolved air flotation (DAF), ion flotation, and precipitation flotation.

The purpose of DAF is to allow micro-bubbles of air to adhere to suspended particles in water, forming agglomerates with a lower density than water, leading the flocs to rise through the water and collect at the surface, where they may be removed as sludge [125]. Ion flotation is based on the employment of surfactants to make ionic metal species in wastewaters hydrophobic, and then using air bubbles to remove these hydrophobic species [126]. Another flotation approach is precipitate flotation, which is

based on the generation of precipitate and subsequent removal by air bubble attachment. Precipitation may occur as metal hydroxide or as a salt with a particular anion, based on the concentration of the metal solution [127].

### 2.5.6 Electrochemical treatment

Metal ions are plated out on a cathode surface in electrochemical processes, which can recover metals in their elemental condition. Electrochemical wastewater treatment systems require a significant investment as well as a costly electrical source. Electrocoagulation, electroflotation, and electrodeposition are the techniques that fall under this category.

The process of electrocoagulation (EC) includes the production of coagulants in a controlled environment by electrically dissolving aluminum or iron electrodes. Metal ions are generated at the anode, while hydrogen gas is discharged at the cathode. The hydrogen gas can aid in the flocculation of the particles in the water [128]. Electrofloatation (EF) is a solid/liquid separation technique that uses microscopic bubbles of hydrogen and oxygen gases created by water electrolysis to float contaminants to the surface of a water body. For the separation of heavy metals, electrodeposition is a "clean" method that leaves no lasting residues when performed under suitable conditions [129].

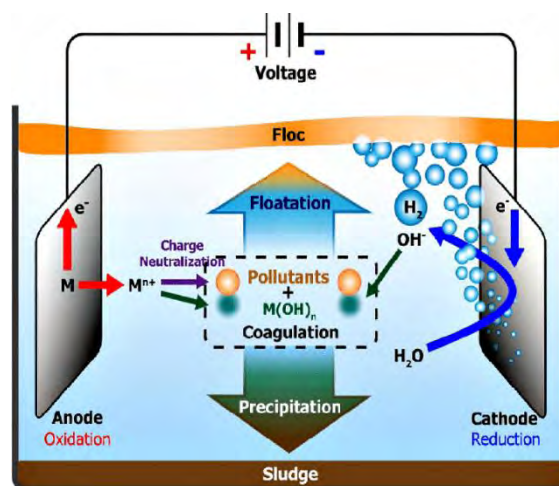


Figure 2–21: Illustration of the electrocoagulation and electrofloatation process of heavy metal removal from water.

### 2.5.7 Adsorption

The adsorption process includes solid–fluid mass transfer and is commonly used to remove chemicals from a fluid phase (liquid or gas) to a solid phase, via their accumulation on the interfacial surface or phase boundary [130]. Adsorption is now widely accepted as a viable and cost-effective approach of heavy metal wastewater treatment. The adsorption process is versatile in terms of design and operation, and it produces high-quality treated effluent in many circumstances. The ease of heavy metal removal without the application of external electricity makes adsorption an economically attractive route. Moreover, adsorption process is sustainable as adsorbents can be renewed using an appropriate desorption procedure.

There have been reports of many different varieties of adsorbents like Activated carbon (AC) adsorbents [131], Carbon nanotubes (CNTs) [132], polymeric bioadsorbents [133], etc. However, magnetic adsorbents have gained tremendous popularity due to its ease of separation. Since this particular work is based on the study on heavy metal adsorption by magnetic nano–adsorbents, the next section is dedicated to the detailed discussion of adsorption mechanisms, kinetic models, isotherm, etc. which will play a vital role in understanding the heavy metal adsorption mechanism.

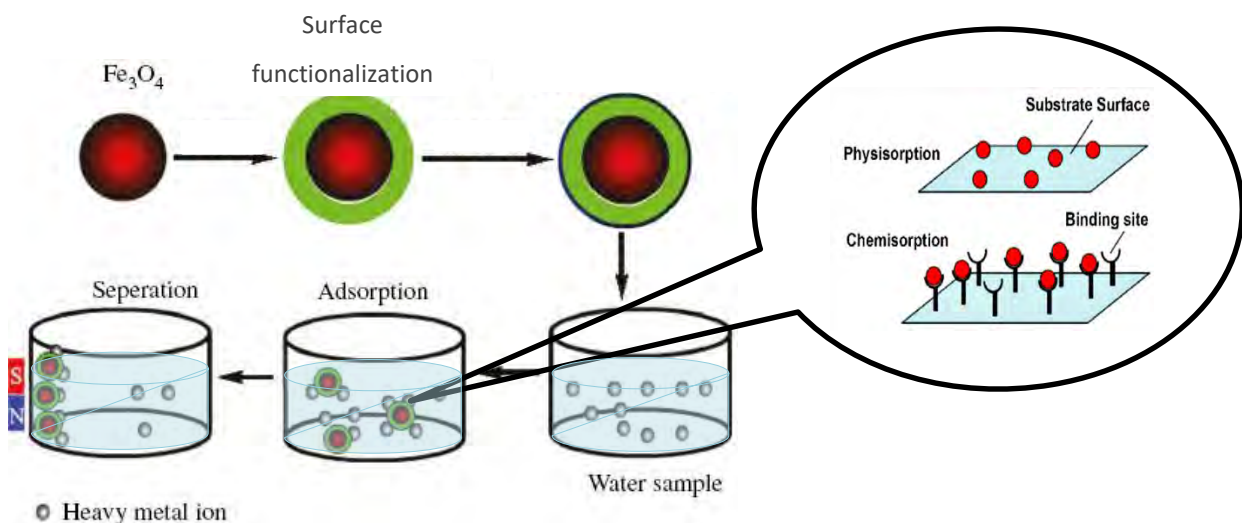


Figure 2–24: Illustration of adsorption of heavy metals by surface functionalized MNPs.



### 2.5.7.1 Adsorbent Categories

Over the last decade various types of adsorbents have been developed for heavy metal remediation of water. These adsorbents can be classified into two major categories- natural and synthetic. Natural adsorbents are substances derived from nature and synthetic adsorbents are developed in the laboratory. Both classes of adsorbent possess advantages and limitations based on their availability, manufacturing ease, cost, and adsorption performance.

#### 2.5.7.1.1 Natural Adsorbents

Nature provided materials like clay minerals and cellulose can be used as adsorbents either directly or with some modifications. Clay minerals have enormous surface areas, allowing them to absorb cations and anions by ion exchange, adsorption, or both methods [134]. These adsorption characteristics of clay are highly influenced by the stacking of certain clay minerals. Adsorption may be influenced by the arrangement of group sites on the material surface. Adsorption may be influenced by the arrangement of group sites on the material surface [135]. The essential features of clay minerals that affect their adsorption capabilities are Cation Exchange Capacity (CEC) and Specific Surface Area (SSA). The total negative charges contained in the clay that may attract and retain heavy metal cations are referred to as CEC [136]. SSA is the total surface area accessible as reactive surfaces [134]. Some clay minerals have just exterior layers, such as kaolinite and illite, whereas others, such as smectites and attapulgite, contain both internal and external layers, giving them substantially greater specific surface areas [137].

Chemically modified cellulose has been explored as heavy metal adsorbent. Esterification, oxidation, and photografting are the mostly explored chemical modification of cellulose to develop heavy metal adsorbent [138]. Dialdehyde cellulose prepared by periodate oxidation of cellulose showed an impressive adsorption capacity of 184 mg g<sup>-1</sup> and 236 mg g<sup>-1</sup> for Ni(II) and Cu(II) [139]. Various agricultural waste like sugarcane bagasse, wheat bran, rice husk, orange peel, saw dust, coconut shell modified with surfactants have been reportedly used as potential heavy metal adsorbents [112].

### 2.5.7.1.2 Synthetic Adsorbents

Synthetic adsorbents can be further classified into carbon based, silica based, or magnetic nano-sized adsorbents. For heavy metal removal, graphene can be oxidized to add hydrophilic groups [140]. Graphene has also been functionalized with magnetic cyclodextrin chitosan [141], ferro/ferric oxide composite [142]. Due to well-developed porous structure and a large internal surface area for adsorption, activated carbon is an effective heavy metal adsorbent. Carbon nanotubes are effective adsorbents for heavy metal removal owing to their chemical stability, wide surface area, outstanding mechanical and electrical capabilities, adsorption property, and well-developed mesopores [143]. Multi-walled carbon nanotubes [144] and nitric acid functionalized carbon nanotubes [145] have been reported to be used for Cr adsorption.

Mesoporous silica may be chemically modified via the attachment of groups including carboxylic acid, sulfonic acid and amino-carbonyl. Polyaniline/polypyrrole/hexagonal type mesoporous silica was reported to exhibit a removal efficiency of 99.2% for Cd at an optimum pH of 8 [146]. Burke et al. employed aminopropyl and mercaptopropyl, functionalized and bi-functionalized, large pore mesoporous silica spheres for the removal of chromium from wastewater [147].

Chitosan based nano-adsorbents have been largely explored due to the unique properties of chitosan discussed previously. Chen et al. developed thiourea-modified magnetic ion imprinted chitosan/TiO<sub>2</sub> composite for the removal of Cd [148]. Activated carbon coated chitosan was reported to have an adsorption capacity of 52.63 mg/g for Cd at an optimum pH of 6 with 100% removal [149].

Red mud- a waste from aluminum industries was modified to adsorb heavy metals from wastewater [150–152]. Alumina nanoparticles have been used for Cu removal successfully [153,154]. Ghaemi et al. combined alumina with PES (polyethersulfone) resulting into increased porosity and hydrophilicity aiding 60% Cu removal compared to 25% with pristine PES membrane [155].

Different types of biological organisms such as yeast [156], bacteria [157,158], algae [159], and fungi [160] have also been explored for heavy metal adsorption by different studies.

## 2.6 Fundamentals of adsorption

The basic concept of adsorption involves the definition of the terms adsorbate and adsorbent. Adsorbates are the components that are transported to the solid phase from the liquid phase, whereas adsorbent is the solid phase that maintains the adsorbates on the surface. The process of adsorption is analyzed by fitting the data to pre-designed kinetic models and isotherm models. The values of adjusted linear regression coefficients (adj.  $R^2$ ) are utilized to estimate the best isotherm and kinetic model.

### 2.6.1 Classification of adsorption

Depending on the nature of the forces that bind adsorbate molecules to adsorbent molecules, adsorption can be classed as a physical (physisorption) or chemical (chemisorption) process. Desorption is the process of removing adsorbate molecules from the adsorbent's surface, which may be accomplished by altering the liquid phase's parameters such as concentration, temperature, and pH.

The adsorption process can work in either a batch or continuous mode. Continuous systems are cheaper and more efficient for full-scale applications, whereas batch systems are better for treating small quantities [161]. The first evaluation of an adsorption process is usually done in a discontinuous manner, with kinetics, equilibrium, and thermodynamics being examined.

### 2.6.2 Adsorption Kinetics

The study of adsorption kinetics yields valuable information on the efficiency and economic feasibility, as well as the potential processes involved [162]. Temperature, pH, starting adsorbate concentration in the fluid phase, and adsorbent size and specific surface are all factors that have a direct impact on adsorption kinetics [163]. In order to discover intrinsic kinetic adsorption constants, many kinetic models were created. Adsorption kinetic models are either based on chemical reactions— pseudo-first order equation, pseudo-second order equation, general-order equation, or the empiric models— Avrami fractionary model, and Elovich chemisorption model [164].

### 2.6.2.1 Kinetic Models Based on the Order of Reaction

Lagergren introduced the pseudo-first-order model as one of the earliest kinetic models to describe the adsorption of a solute from a fluid phase to the surface of a solid phase in 1898. When studying the adsorption kinetics of oxalic acid and malonic acid on activated carbon, he discovered that adsorption happened quickly at first, then gradually increased until the adsorption equilibrium was reached. The pseudo-first-order model is based on the adsorption capacity of the solid and is expressed by equation 2.4 below.

$$\log(q_e - q_t) = \log(q_e) - \frac{k_1 t}{2.303} \dots \dots \dots \text{Equation 2.4}$$

Where  $q_t$  ( $\text{mg g}^{-1}$ ) is the adsorption capacity at contact time  $t$  (min),  $q_e$  ( $\text{mg g}^{-1}$ ) is the adsorption capacity in equilibrium and  $k_1$  ( $\text{min}^{-1}$ ) is the pseudo-first-order rate constant. The quantity of adsorbate taken up by the adsorbent per unit mass (or volume) of the adsorbent is known as adsorption capacity,  $q$ . It is calculated from initial ( $C_i$   $\text{mgL}^{-1}$ ) and final concentration ( $C$   $\text{mgL}^{-1}$ ) of the adsorbate in the solution, volume of the liquid solution ( $V$ ) in mL, and the mass of the added adsorbent  $W$  in g from the formula below.

$$q = \frac{(C_i - C)V}{W \times 1000} \dots \dots \dots \text{Equation 2.5}$$

The pseudo-second-order model similar to the pseudo first-order model, is also based on the adsorptive capacity of the solid phase. It is expressed as,

$$\frac{t}{q_t} = \frac{1}{k_2 q_e^2} + \frac{t}{q_e} \dots \dots \dots \text{Equation 2.6}$$

where  $k_2$  ( $\text{g mg}^{-1} \text{min}^{-1}$ ) is the pseudo-second-order rate constant. The most often used kinetic models for characterizing adsorption processes based on chemical reactions are pseudo-first-order and pseudo-second-order.

### 2.6.2.2 Empiric adsorption kinetic models

The Elovich equation is commonly used in chemisorption kinetics [165]. The equation has been shown to cover a wide variety of slow adsorption rates and has been successfully applied to several chemisorption processes [166]. The Elovich equation is also applicable for heterogeneous adsorption surfaces. The Elovich–chemisorption kinetic adsorption model is expressed as,

$$q_t = \frac{1}{\beta} \ln(\alpha\beta) + \frac{1}{\beta} \ln(t) \dots \dots \dots \text{Equation 2.7}$$

Here  $\alpha$  is the initial adsorption rate ( $\text{mg g}^{-1} \text{min}^{-1}$ ) and  $\beta$  is related to the extent of surface coverage and the activation energy involved in chemisorption with the unit  $\text{g mg}^{-1}$ .

The traditional models still have limitations in determining some kinetic parameters, possible changes of the adsorption rates as function of the initial concentration and the adsorption, and determining fractional kinetic orders in some cases. The alternative Avrami kinetic equation can overcome these imitations and provide a match in the calculated and experimental data [167]. The Avrami equation is adapted from the kinetic thermal decomposition modeling. It is expressed as,

$$q_t = q_e [1 - \exp(-k_{AV}t)]^{n_{AV}} \dots \dots \dots \text{Equation 2.8}$$

Here,  $k_{AV}$  is the Avrami kinetic constant ( $\text{min}^{-1}$ ), and  $n_{AV}$  is a fractional adsorption order, which is related to the adsorption mechanism.

### 2.6.3 Adsorption Isotherms

An adsorption isotherm describes the connection between the adsorption capacity ( $q_e$ ) and the final concentration of the adsorbate in the solution when equilibrium is attained at a constant temperature. The adsorption isotherm model parameters give important information on the surface qualities, adsorption process, and interaction between the adsorbent and adsorbate. The Langmuir [168] and Freundlich isotherms are the most widely used and studied in the literature. Sips isotherm, Liu isotherm, and Redlich–Peterson isotherm models are also applied in many reported studies.

#### 2.6.3.1 Langmuir isotherm model

The Langmuir model for gas adsorption was established theoretically using a highly idealized adsorption mechanism for gaseous model. The assumptions made by the Langmuir isotherm model consists of homogeneous surfaces, monolayer adsorption, constant energies in the adsorption sites, neighboring sites does not have any interaction, and a single site can only provide accommodations to a single adsorbate particle [169]. The Langmuir isotherm equation is expressed by the following equation.

$$q_e = \frac{q_{max} + K_L C_e}{1 + K_L C_e} \dots \dots \dots \text{Equation 2.9}$$

Here,  $q_e$  is the adsorption capacity ( $\text{mg g}^{-1}$ ) of the adsorbent at equilibrium,  $C_e$  is the solution concentration ( $\text{mg L}^{-1}$ ) at the equilibrium,  $K_L$  is the Langmuir equilibrium constant with the unit  $\text{L mg}^{-1}$ , and  $q_{max}$  is the maximum adsorption capacity of the adsorbent ( $\text{mg g}^{-1}$ ). Another parameter termed as the separation factor  $R_L$  is calculated from the initial adsorbate concentration in solution  $C_i$  and the Langmuir equilibrium constant  $K_L$  is derived from the equation 2.9 using the following formula.

$$R_L = \frac{1}{1 + C_i K_L} \dots \dots \dots \text{Equation 2.10}$$

The calculated value of  $R_L$  indicates the adsorption possibility. If the value of  $R_L$  fall between the range  $0 < R_L < 1$  then the conditions are favorable for reversible adsorption, for  $R_L = 0$  the adsorption is irreversible, and for  $R_L = 1$  the adsorption data is linear.

### 2.6.3.2 Freundlich isotherm model

The Freundlich model is an empirical model that was constructed originally for gas adsorption. The model is based on the assumption that concentration of adsorbate on the adsorbent surface increases as the adsorbate concentration increases and adsorption will take place in infinitely [169]. The model has been extensively utilized to explain adsorptive processes in aqueous environments. Non-ideal systems with heterogeneous surfaces and multilayer adsorption can be represented using the Freundlich equation. But it is usually limited to midrange concentration levels [170]. Equation 2.11 is the expression of the Freundlich isotherm model.

$$q_e = K_F C_e^{\frac{1}{n}} \dots \dots \dots \text{Equation 2.11}$$

Here  $K_F$  is the Freundlich constant with the unit  $\text{mg g}^{-1}(\text{mg L}^{-1})^{-1/n}$ , and  $1/n$  is an empirical dimensionless constant termed as the adsorption intensity. The calculated value of  $1/n$  indicates the favorable or unfavorable conditions for adsorption. Adsorption following the Freundlich isotherm model is favored when  $0.1 < 1/n < 0.5$  whereas it will not be favored when the value of  $1/n$  is greater than 2.

### 2.6.3.3 Sips isotherm model

The Sips isotherm model is an amalgamation of Langmuir and Freundlich model [171]. Therefore, the Sips model is described in the following form.

$$q_e = \frac{q_{max} K_S C_e^{\frac{1}{n_s}}}{1 + K_S C_e^{\frac{1}{n_s}}} \dots \dots \dots \text{Equation 2.12}$$

$K_S$  is the Sips equilibrium constant ( $\text{mg L}^{-1}$ )<sup>-1/n</sup>,  $q_{max}$  is the Sips maximum adsorption capacity ( $\text{mg g}^{-1}$ ), and  $n_s$  is the exponent where the value lies between the range  $0 < 1/n_s \leq 1$ . Sips equation predicts a monolayer adsorption capacity typical of the Langmuir isotherm at high adsorbate concentrations, but it decreases to the Freundlich isotherm at low adsorbate concentrations.

### 2.6.3.4 Liu isotherm model

The Liu isotherm model is also a hybrid of the Langmuir and Freundlich isotherm models, with the Langmuir model's monolayer assumption and the Freundlich model's infinite adsorption assumption removed [172]. According to the Liu model, the adsorbent's active sites cannot have the same energy. As a result, the adsorbent may have active spots that the adsorbate molecules choose to occupy. But unlike the Freundlich isotherm model saturation of the active sites can occur. The Liu isotherm model is defined by the following equation.

$$q_e = \frac{q_{max} (K_g C_e)^{n_L}}{1 + (K_g C_e)^{n_L}} \dots \dots \dots \text{Equation 2.13}$$

Here  $K_g$  is the Liu equilibrium constant ( $\text{L mg}^{-1}$ ) and  $n_L$  is dimensionless exponent of the Liu equation. The benefit of the Liu isotherm model over the Sips isotherm model is that the exponent  $n_L$  can be any positive number, whereas the exponent of the Sips is only allowed to be  $1/n_s \leq 1$ .

### 2.6.3.5 Redlich–Peterson isotherm model

Redlich–Peterson is another empirical isotherm model [173]. There are three parameters in this model and it is expressed as,

$$q_e = \frac{K_{RP}C_e}{1+a_{RP}C_e^g} \dots \dots \dots \text{Equation 2.14}$$

$K_{RP}$  and  $a_{RP}$  are Redlich–Peterson constants with the units of  $L g^{-1}$  and  $(mg L^{-1})^{-g}$  respectively, and  $g$  is the dimensionless Redlich–Peterson exponent which has a value in the range  $0 < g \leq 1$ . The model becomes linear when there is lower surface coverage at  $g=0$ . It takes the Langmuir isotherm form when  $g=1$ .

### 2.6.3.6 Other isotherm models for adsorption

Other models can be used to describe an adsorption mechanism, in addition to the equilibrium models discussed above. Table 2–7 lists the mathematical equations along with associated parameters for several of these adsorption equilibrium models. The terms  $q_e$ ,  $q_{max}$ , and  $C_e$  define the equilibrium adsorption capacity, maximum adsorption capacity, and adsorbate concentration at equilibrium respectively in all cases.

Table 2–7: List of other reported adsorption isotherm models.

Isotherm model	Mathematical expression	Associated parameters	Ref.
Hill	$q_e = \frac{q_{max}C_e^{n_H}}{K_H + C_e^{n_H}}$	$K_H$ – Hill equilibrium isotherm constant with unit $(mgL^{-1})^{n_H}$ $n_H$ – Dimensionless Hill exponent.	[174]
Khan	$q_e = \frac{q_{max}K_K C_e}{(1 + K_K C_e)^{n_K}}$	$K_K$ – Khan equilibrium isotherm constant with unit $(L mg^{-1})$ $n_K$ – Dimensionless Khan exponent	



Isotherm model	Mathematical expression	Associated parameters	Ref.
<b>Radke–Prausnitz</b>	$q_e = \frac{q_{max} K_{RAP} C_e}{(1 + K_{RAP} C_e)^{n_{RAP}}}$	$K_{RAP}$ – Radke–Prausnitz equilibrium isotherm constant with unit ( $L\ mg^{-1}$ ) $n_{RP}$ – Dimensionless Radke–Prausnitz exponent	[175]
<b>Toth</b>	$q_e = \frac{q_{max} K_T C_e}{[1 + (K_T C_e)^{1/n_T}]^{n_T}}$	$K_T$ – Toth equilibrium isotherm constant with unit ( $L\ mg^{-1}$ ) $n_T$ – Dimensionless Toth exponent	

Since, Langmuir and Freundlich isotherm models have been reported as the most suitable models for chitosan-mesoporous silica based adsorbents, the adsorption data from this work was also fitted to these two models with satisfactory results.

### 3 Chapter 3: Experimental Details

The objective of this work was to synthesize novel magnetic magnetite ( $\text{Fe}_3\text{O}_4$ ) nanoparticles with chitosan mesoporous silica coating and to evaluate their efficiency in heavy metal removal from water along with their recoverability via desorption. Therefore, the experimental work of this thesis was performed in the following steps-

1. Synthesis of  $\text{Fe}_3\text{O}_4$  MNPs via thermal decomposition method.
2. Coating the synthesized MNPs with mesoporous silica and chitosan coating.
3. Study the adsorption capacity and mechanism of the prepared MNPs for lead ( $\text{Pb}^{2+}$ ), cadmium ( $\text{Cd}^{2+}$ ), and arsenic ( $\text{As}^{3+}$ ).

#### 3.1 Raw Materials

All the raw materials used in different stages of this thesis work is listed in the table 3–1 below.

Table 3–1: List of chemical reagents used at different stages of experiment.

<i>Chemical</i>	<i>Specification</i>
<b><i>Synthesis of <math>\text{Fe}_3\text{O}_4</math> MNPs</i></b>	
Sodium hydroxide ( $\text{NaOH}$ )	Assay $\geq$ 98%, Sigma-Aldrich
Oleic acid ( $\text{C}_{18}\text{H}_{34}\text{O}_2$ )	Assay $\geq$ 99%, Sigma-Aldrich
Ferric chloride ( $\text{FeCl}_3$ )	Anhydrous, assay $\geq$ 98%, Merck
Ethanol ( $\text{C}_2\text{H}_5\text{OH}$ )	Assay $\geq$ 96%, Merck
Hexane ( $\text{C}_6\text{H}_{14}$ )	Assay $\geq$ 95%, Sigma-Aldrich
Octadecane ( $\text{C}_{18}\text{H}_{38}$ )	Assay $\geq$ 99%, Aldrich
Propanol ( $\text{C}_3\text{H}_7\text{OH}$ )	Assay $\geq$ 96%, Merck

<i>Chemical</i>	<i>Specification</i>
<b><i>Surface functionalization</i></b>	
Cetrimonium bromide (CTAB) (C <sub>19</sub> H <sub>42</sub> BrN)	Assay ≥ 99%, Kemaus
Tetraethyl orthosilicate (TEOS) (SiC <sub>8</sub> H <sub>20</sub> O <sub>4</sub> )	Assay ≥ 99.5%, Sigma-Aldrich
Ammonium Nitrate (NH <sub>4</sub> NO <sub>3</sub> )	Assay ≥ 99%, Sigma-Aldrich
Chitosan	Sigma-Aldrich
Acetic acid (CH <sub>3</sub> COOH)	Assay ≥ 99.8%, Supelco.
<b><i>Adsorption test</i></b>	
Lead chloride (PbCl <sub>2</sub> )	Assay ≥ 98%, Sigma-Aldrich
Cadmium nitrate tetrahydrate (Cd(NO <sub>3</sub> ) <sub>2</sub> · 4H <sub>2</sub> O)	Assay ≥ 98%, Sigma-Aldrich
Arsenic trioxide (As <sub>2</sub> O <sub>3</sub> )	Assay ≥ 99.5%, Sigma-Aldrich
Hydrochloric acid (HCl)	Assay ≥ 37%, Sigma-Aldrich

Deionized water (DIW) was used in steps where it was needed for solution making or washing.

### 3.2 Synthesis of Fe<sub>3</sub>O<sub>4</sub> MNPs

- **Precursor preparation-** For the Fe<sub>3</sub>O<sub>4</sub> MNPs synthesis a Fe-oleat precursor was prepared by mixing 4.83g NaOH pellets in 60 ml DIW and adding 37.9 ml oleic acid. Another mixture of 10.8g of FeCl<sub>3</sub> dissolved in 80 ml ethanol and 140 ml hexane was also prepared. These two mixtures were added to a three-necked bottle and refluxed at 70<sup>o</sup>C for 4 hours.
- **Precursor washing-** the heated contents were cooled to the room temperature and the upper brownish layer of Fe-oleat was separated using a separatory funnel. The Fe-oleat was washed alternately with DIW and hexane to remove the inorganic salts and excess

oleic acid respectively. After three wash cycles the precursor was left in open air at room temperature for the hexane to evaporate.

- **MNPs synthesis-** for the thermal decomposition synthesis 18.33 g Fe-oleate precursor was dissolved in 100 g octadecane with 2.89 g oleic acid by stirring at 50°C for 10 minutes. The mixture was then heated under reflux in nitrogen atmosphere at 200°C for 1 hour followed by refluxing at 315°C for 10 minutes.
- **Washing of MNPs-** after thermal decomposition the mixture was cooled down to room temperature and taken into the separatory funnel. The MNPs were precipitated from the organic solvent by adding excess acetone. The precipitated MNPs centrifuged out of the solution. Then the MNPs were washed by adding hexane and vortexing followed by sonication for 5 minutes. The MNPs were again precipitated from hexane by addition of excess acetone and then centrifuged out of the acetone hexane solution. This cycle was repeated for 4 times. Finally, the MNPs were preserved in hexane and dried afterwards as needed for further study.

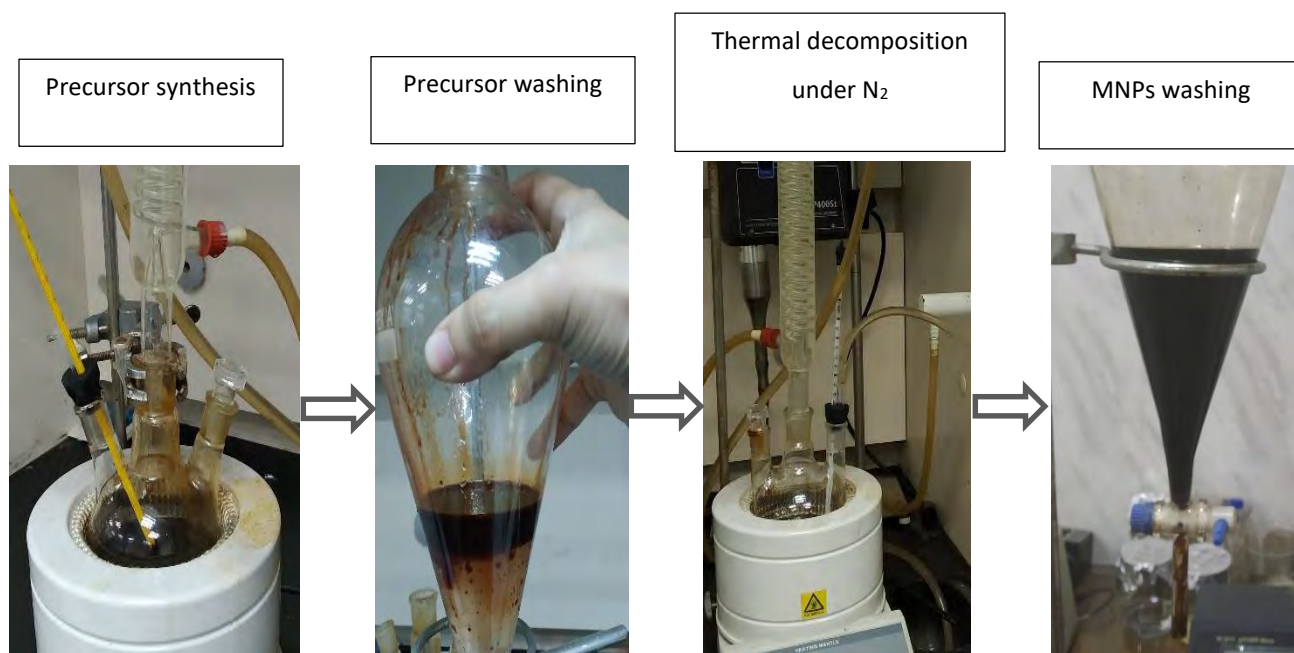


Figure 3–1: Thermal decomposition synthesis of Fe<sub>3</sub>O<sub>4</sub> MNPs.

### 3.3 Surface functionalization of MNPs with mesoporous silica and chitosan

- **Mesoporous silica coating-** 1g of the prepared MNPs were sonicated for 24 hours in the mixture of 5g CTAB and 1.6g NaOH in 480 ml of DIW. The sonicated mixture was heated to 80°C while stirring at 1500 rpm. 25 ml of TEOS was added dropwise to the mixture with 2 hours of additional stirring. The precipitate was centrifuged at 13500 rpm and washed three times with ethanol followed by air drying.
- **Surfactant removal-** the CTAB template was removed from the particles by stirring them in  $\text{NH}_4\text{NO}_3$  and ethanol mixture for 30 minutes followed by centrifugation and ethanol wash. This cycle was repeated for two times and sample was air dried.

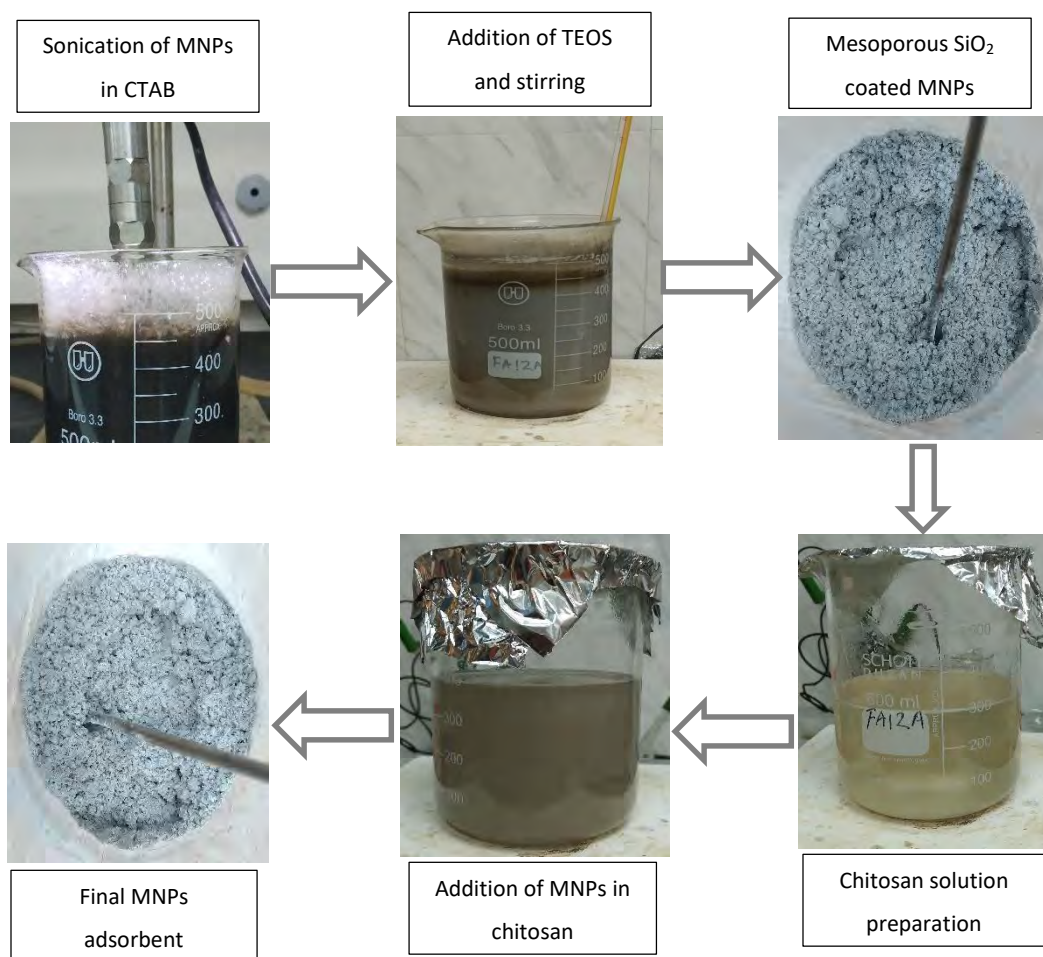


Figure 3–3: Surface functionalization of  $\text{Fe}_3\text{O}_4$  MNPs with mesoporous  $\text{SiO}_2$  and chitosan.

- **Chitosan coating**- chitosan solution was prepared by dissolving 5g low molecular weight chitosan in 400 ml of 5% (v/v) acetic acid. The solution was stirred for 72 hours. 200 mg of Silica coated MNPs were sonicated in 10 ml ethanol for 10 minutes and added to the chitosan solution. The pH of the solution was adjusted between 3.5-4.5 by addition of acetic acid. The mixture was stirred for 24 hours. Finally, the MNPs were centrifuged out of the chitosan solution and subjected to three cycles of ethanol and DIW wash and air dried to be used as adsorbents.

### 3.4 Adsorption test

- **Salt solution preparation**- 0.14g of  $\text{PbCl}_2$  and 0.2g of  $\text{Cd}(\text{NO}_3)_2$  was dissolved in 100 ml DIW to prepare 1000 mg/L solutions of  $\text{Pb}^{2+}$  and  $\text{Cd}^{2+}$ . These solutions were diluted to prepare solutions of varied concentrations ranging from 5 mg/L to 150 mg/L. 13.2mg of  $\text{As}_2\text{O}_3$  was dissolved in 10% NaOH solution and pH was neutralized with 1N HCl. The solution was diluted to 500 ml with DIW to make a 20 mg/L  $\text{As}^{3+}$  solution which was diluted to prepare solutions ranging from 10  $\mu\text{g/L}$  to 100  $\mu\text{g/L}$ .
- **Adsorption**- the adsorption test was carried out in batches with interchanging the variables of contact time and initial concentration. 50 mg of adsorbent was added to 100 ml solution of varied concentrations and stirred for 30 minutes. The amount of adsorbent was 5 mg for the  $\text{As}^{3+}$  solution due to dilute concentration. Same experiment was conducted with a solution of 50 mg/L but with contact time varying from 5 minutes to 30 minutes. For  $\text{As}^{3+}$  solution the concentration was 50  $\mu\text{g/L}$ . the final concentration after adsorption was measured with atomic absorption spectrometer (AAS).
- **Kinetic model and isotherm model fitting**- the collected data of final concentrations from the fixed initial concentration study was fitted to the pseudo first order and pseudo second order kinetic model with the help of the OriginPro software. The data from the fixed contact time study was fitted to the Langmuir and Freundlich isotherm models.
- **Desorption study**- 50 mg dried adsorbents used in the adsorption experiment of  $\text{Pb}^{2+}$  and  $\text{Cd}^{2+}$  solutions were sonicated in a solution of pH 4-4.5 for 30 minutes and then separated

by centrifugation. The solution was subjected to AAS for measuring the  $Pb^{2+}$ ,  $Cd^{2+}$ , and  $Fe^{3+}$  concentration.

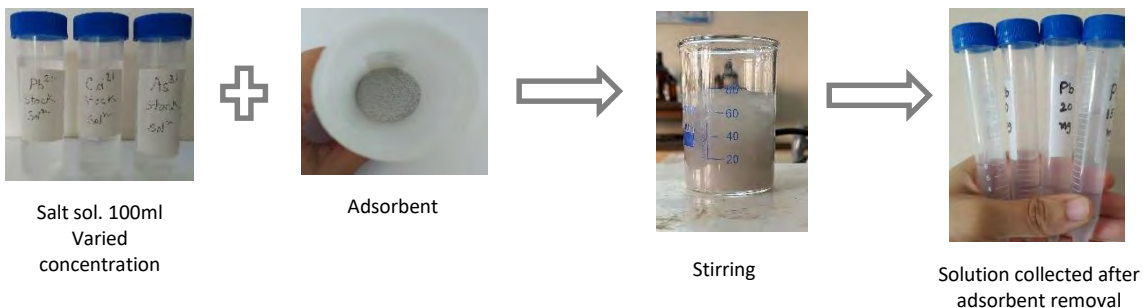


Figure 3–5: Adsorption experiment.

## 3.5 Characterizations

### 3.5.1 X-ray Diffractometry (XRD)

Rigaku SmartLab XRD machine was used to determine the structural and physical phase of the bare as well as the coated MNPs. A Cu x-ray source of wavelength  $K_{\alpha 1} = 1.540598 \text{ \AA}$  was used for the tests. The diffraction was conducted between the Bragg angle of  $10^{\circ}$  and  $80^{\circ}$ . The data was plotted and analyzed using OriginPro software.



Figure 3–6: Rigaku SmartLab XRD machine.

### 3.5.2 Transmission Electron Microscopy (TEM)

F200X Talos from Thermo-Fisher TEM machine was used to perform the transmission electron microscopy of the bare and coated MNPS to determine their morphological, structural and elemental aspect before and after surface coating.



Figure 3–9: TEM machine.

### 3.5.3 Fourier Transform Infrared Spectroscopy (FTIR)

Perkin-Elmer Spectrum 2 NFT-NIR Spectrometer was used to conduct FTIR between wavenumber 400 to 4000  $\text{cm}^{-1}$  of the bare and coated MNPs to observe the changes resulting from the coating synthesis. The FTIR spectra helps to determine whether coating was successfully synthesized over the MNPs.



Figure 3–10: FTIR machine.



### 3.5.4 Physical Properties Measurement System (PPMS)

The vibrating system magnetometer (VSM) data of the bare and coated MNPs was retrieved with the Dynacool PPMS system from Quantum Design Inc. The samples were tested at 300K with the magnetic field varying up to 5T. 9mg sample was taken for each run. The VSM data indicated the magnetic properties of the adsorbent and the effect of coating materials on the magnetic property of the  $\text{Fe}_3\text{O}_4$  core.



Figure 3–13: Physical Properties Measurement System.

### 3.5.5 Atomic Absorption Spectroscopy (AAS)

The concentration of the  $\text{Pb}^{2+}$ ,  $\text{Cd}^{2+}$ , and  $\text{As}^{3+}$  solutions from the adsorption-desorption experiments were measured by the Shimadzu Atomic Absorption Spectrophotometer Model: AA-7000. Determining the final concentration after adsorption study helped to fit the data to a proper kinetic and isotherm model and determine the adsorption mechanism consequently.



Figure 3–14: AAS machine.

## 4 Chapter 4: Results and Discussion

This chapter contains the detailed discussion of the results obtained from the FTIR, XRD, TEM, and VSM characterization of the bare and surface functionalized MNPs. Analysis of these results provided visualization of the morphological and structural phase of the magnetic core of the MNPs along with the confirmation of successful surface functionalization. The AAS data of the adsorption-desorption solution was studied by fitting them to different adsorption kinetic and isotherm models in order to envision the adsorption mechanism and compare the results with reported literature.

### 4.1 X-Ray Diffraction Analysis

The XRD analysis of the bare MNPs after synthesis confirmed the formation of  $\text{Fe}_3\text{O}_4$  via thermal decomposition. The subsequent XRD tests conducted on the MNPs after coating them with mesoporous  $\text{SiO}_2$  and chitosan showed that the  $\text{Fe}_3\text{O}_4$  core was intact as the XRD data still showed the characteristic peaks of  $\text{Fe}_3\text{O}_4$ . Figures 4–1 and 4–2 below contain the XRD plot of the bare and coated  $\text{Fe}_3\text{O}_4$  MNPs.

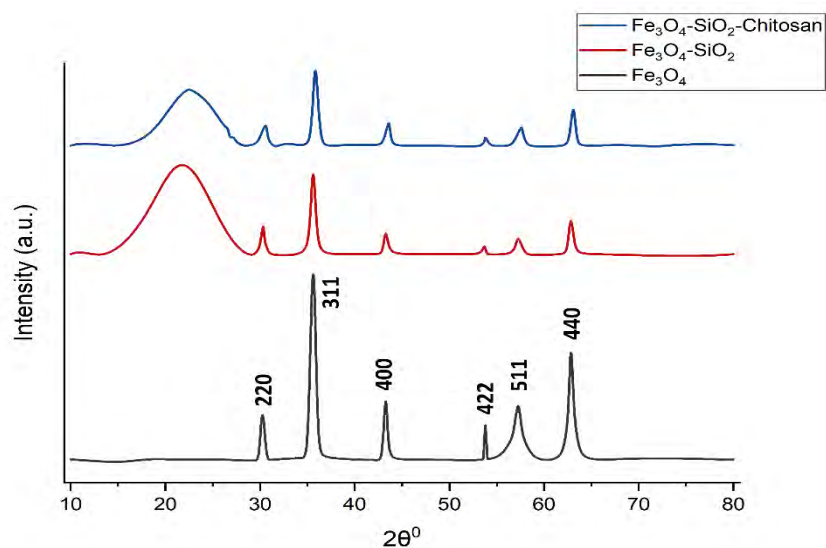


Figure 4–1: XRD plot of the bare and coated  $\text{Fe}_3\text{O}_4$  MNPs.

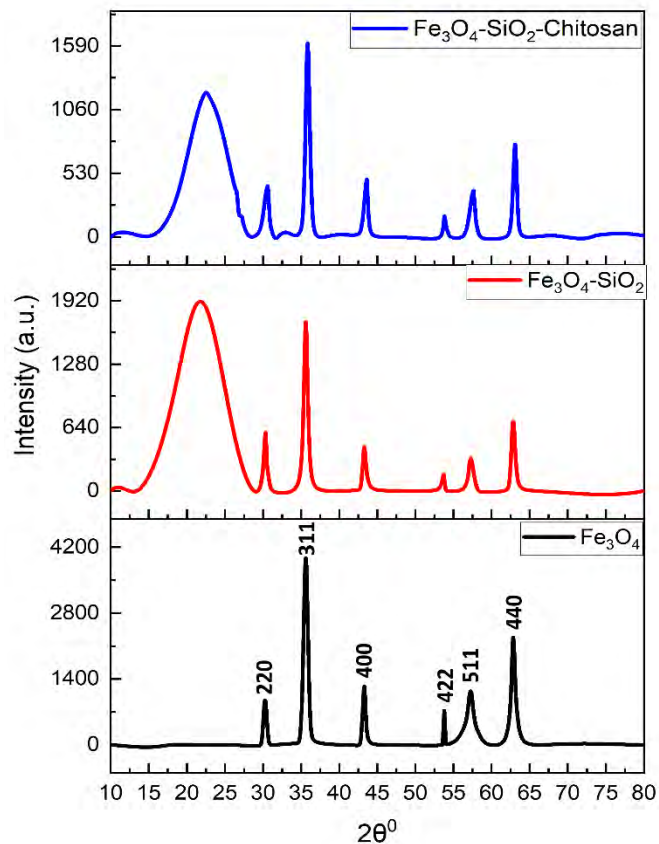


Figure 4-4: Comparative stacking of XRD plots of bare and coated  $\text{Fe}_3\text{O}_4$  MNPs.

The peaks of the bare  $\text{Fe}_3\text{O}_4$  MNPs were compared to the ICDD-PDF card no. 01-085-1436 [176]. The diffraction peaks at  $2\theta = 30.1^\circ$  (220),  $35.42^\circ$  (311),  $37.05^\circ$  (400),  $53.4^\circ$  (422),  $56.9^\circ$  (511),  $62.5^\circ$  (440) are almost a perfect match with the standard diffraction data of magnetite [177]. It is evident from both of the above figures that even after surface coating the positions of these characteristic peaks did not shift. Which is an indication of the intact magnetic core of the adsorbent. The coating process did not result in any structural alterations in the  $\text{Fe}_3\text{O}_4$  core. The only change in the XRD spectra after coating process showed in figure 4-2 is the decrease in the peak intensity which was expected due to the coating effect. The appearance of the broad peak after silica coating at  $2\theta = 22^\circ$  is the characteristic peak of mesoporous silica. Peak broadening indicates the presence of pores which lead to amorphous structure [178]. Since chitosan is an

organic substance, the chitosan coating does not generate any new peaks in the XRD spectra. The only effect of the chitosan coating is further decrease in the peak intensity.

The XRD analysis was also utilized to calculate the crystallite size which helped to estimate the size of the MNPs. The calculated crystallite size was later confirmed with the TEM analysis. The crystallite size of the bare MNPs was calculate by the Scherrer's formula represented as

$$D = \frac{k\lambda}{\beta \cos\theta} \dots\dots\dots \text{Equation 4.1}$$

Where, D is the mean crystallite size or diameter, k is a dimensionless factor of value 0.94,  $\lambda$  is the wavelength of x-ray which is 1.54 Å for this experiment,  $\beta$  is the full width half maxima (FWHM) measurement of the characteristic peak, and  $\theta$  is the Bragg angle corresponding to the characteristic peak. D was calculated using the above equation for each characteristic peaks and average crystallite size was calculate. The results are given in table 4–1.

Table 4–1: Calculation of crystallite size of Fe<sub>3</sub>O<sub>4</sub> MNPs from FWHM.

Peak	2 $\theta$	FWHM	Crystallite Size, nm	Avg. Crystallite size of Fe <sub>3</sub> O <sub>4</sub> , nm
1	30.2289	0.5155	16.6660	
2	35.58807	0.6726	12.9510	
3	43.26141	0.4365	12.9510	15.9090
4	57.2173	1.0614	18.4885	
5	62.80711	0.5256	18.4885	

Based on the calculated average crystallite size it was estimated that average size of the MNPs would be close to 16 nm. The actual size was confirmed by the TEM analysis.

## 4.2 Transmission Electron Microscopy Analysis

TEM was conducted on the bare and mesoporous silica coated MNPs. Figure 4–3 shows the TEM images of bare and silica coated  $\text{Fe}_3\text{O}_4$  particles at different magnifications along with the particle size distribution curves. The size distribution curves were constructed using the ImageJ and OriginPro software.

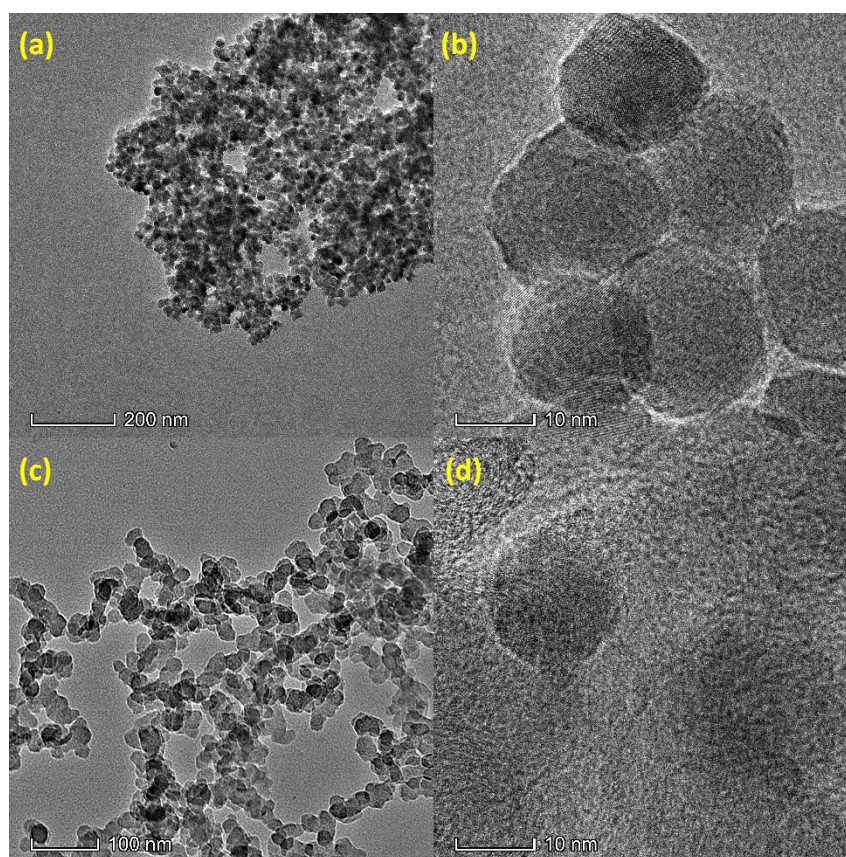


Figure 4–5: TEM images of (a) and (b) bare  $\text{Fe}_3\text{O}_4$  MNPs; (c) and (d) mesoporous  $\text{SiO}_2$  coated  $\text{Fe}_3\text{O}_4$  MNPs

It was concluded from the TEM images that the bare  $\text{Fe}_3\text{O}_4$  had a mixture of cubic and spherical shape. According to Dewi et al. [19] the  $\text{Fe}_3\text{O}_4$  MNPs initially take a cubic formation upon the immediate decomposition of Fe-oleate precursor and eventually take spherical shape with further refluxing. Dewi et al. achieved a complete shape transformation in spheres with 40 minutes of refluxing. Since the refluxing time was 10 minutes in this study, the shape of the MNPs

was in between cubic and spherical. The  $\text{SiO}_2$  coated MNPs appeared to be larger in the TEM image.

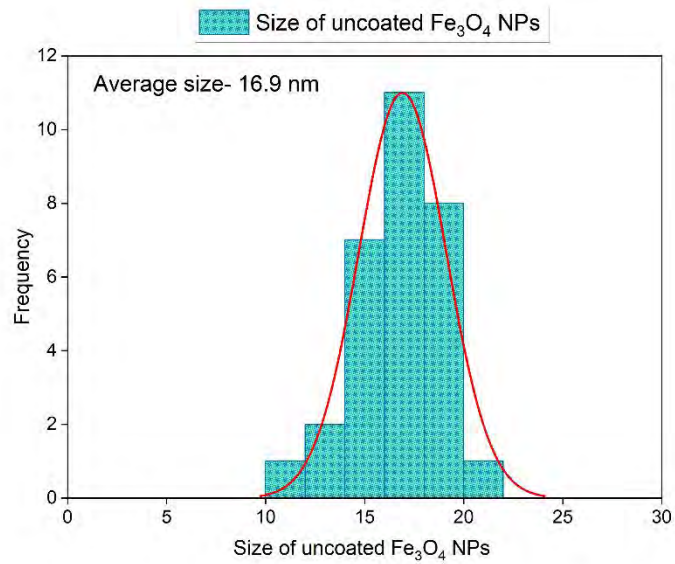


Figure 4–7: Size distribution of bare  $\text{Fe}_3\text{O}_4$  MNPs.

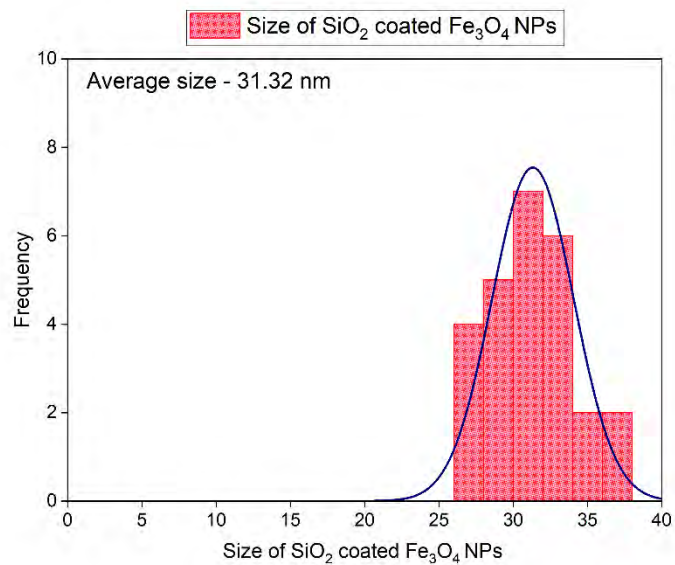


Figure 4–8: Size distribution of mesoporous  $\text{SiO}_2$  coated  $\text{Fe}_3\text{O}_4$  MNPs.

The size distribution data retrieved from the TEM images showed that monodispersity was achieved with the thermal decomposition synthesis in the  $\text{Fe}_3\text{O}_4$  MNPs. The average size calculated from the size distribution is 16.9 nm which is very close to the calculated crystallite size from the XRD analysis. Therefore, it can be concluded that the particles were single domain MNPs. The average size of the  $\text{SiO}_2$  coated MNPs were larger than the bare MNPs which is attributed to the presence of the outer shell.

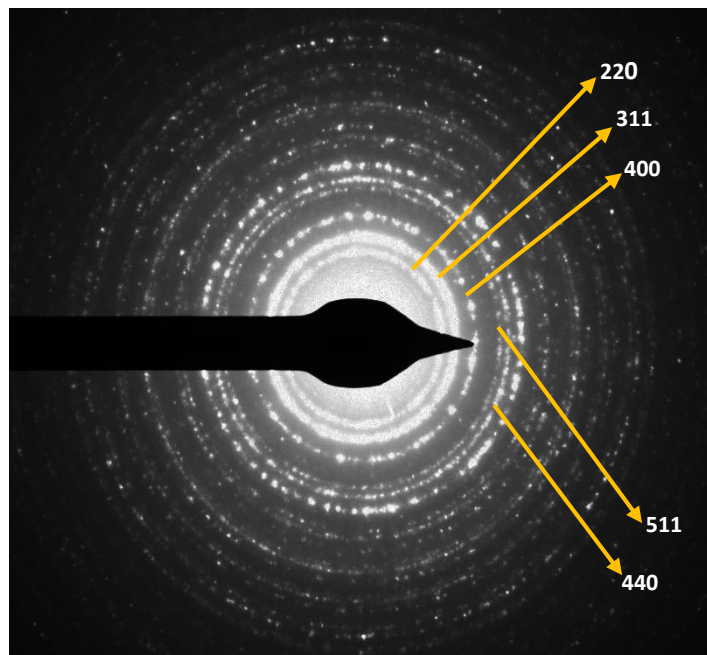
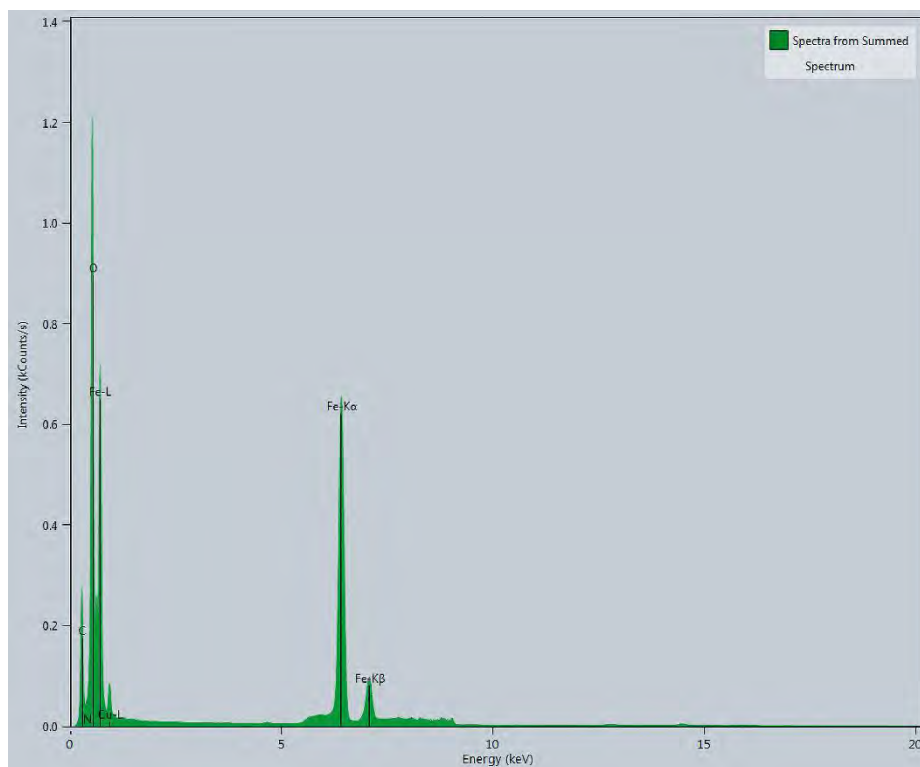
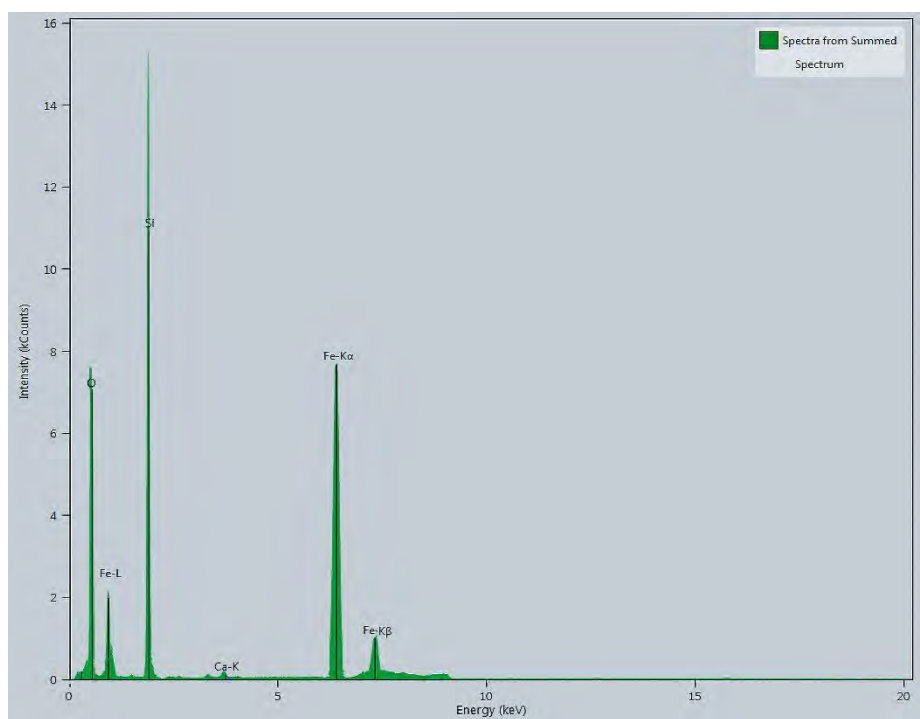


Figure 4–10: SAED pattern of bare  $\text{Fe}_3\text{O}_4$  MNPs.

The selected area electron diffraction (SAED) obtained by TEM was analyzed and the result was found to be in agreement with the XRD pattern, further confirming the phase of  $\text{Fe}_3\text{O}_4$ .

The Energy Dispersive X-ray spectra (EDS) of the  $\text{Fe}_3\text{O}_4$  MNPs confirms the presence of iron (Fe), oxygen (O), nitrogen (N), and carbon (C). The O and C signal is due to O and C atoms in the oleic acid acting as the capping agent of the MNPs. The N signal can be attributed to the residual N present on the surface of the MNPs as they were synthesized in a nitrogen environment. The EDS spectra of the mesoporous  $\text{SiO}_2$  coated MNPs exhibits an extra peak of silicon (Si).

Figure 4–11: EDS spectra of bare Fe<sub>3</sub>O<sub>4</sub> MNPs.Figure 4–12: EDS spectra of mesoporous SiO<sub>2</sub> coated Fe<sub>3</sub>O<sub>4</sub> MNPs.



### 4.3 Fourier Transform Infrared Spectroscopic Analysis

FTIR was conducted to confirm the presence of the SiO<sub>2</sub> and chitosan coating on the MNPs. The first FTIR was done on the sample after the SiO<sub>2</sub> coating process but before the removal of the CTAB template via ion exchange. The later FTIR tests were done after the template removal and after the chitosan coating procedure. Figure 4–9 illustrates the FTIR spectra of three different stages of the adsorbent.

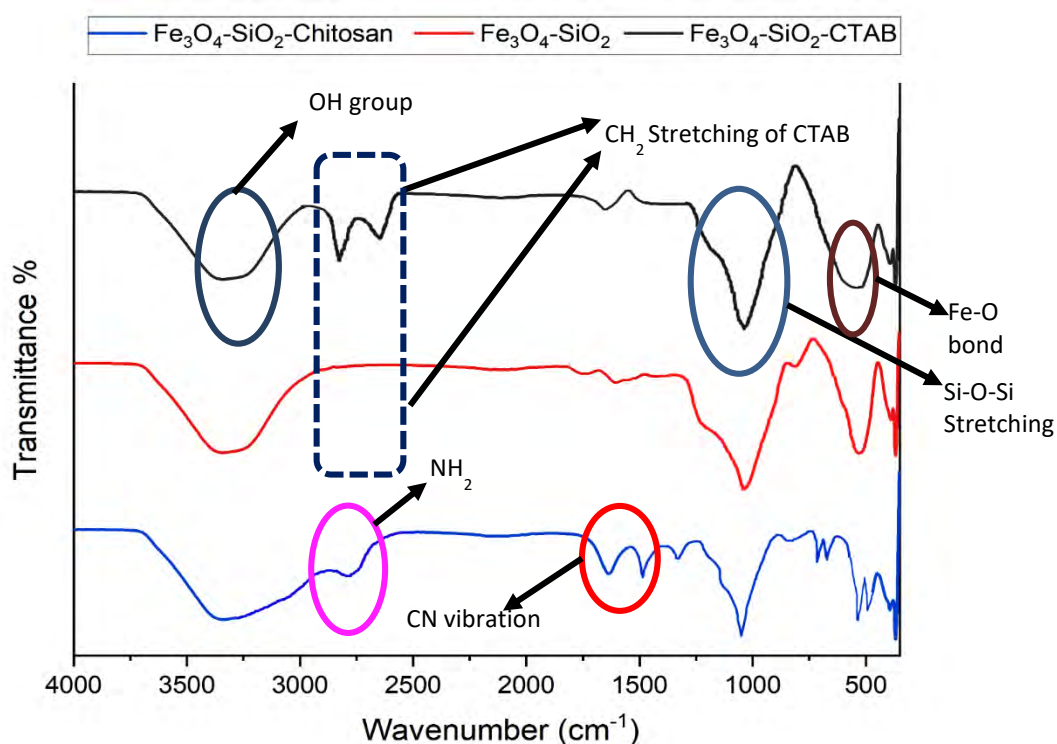


Figure 4–15: FTIR spectra of Fe<sub>3</sub>O<sub>4</sub>-SiO<sub>2</sub>-CTAB, Fe<sub>3</sub>O<sub>4</sub>-SiO<sub>2</sub>, and Fe<sub>3</sub>O<sub>4</sub>-SiO<sub>2</sub>-Chitosan MNPs.

The FTIR spectra of all three samples were recorded between the wavenumber 450-4000 cm<sup>-1</sup>. All three sample spectra contained absorption peaks around 580 cm<sup>-1</sup> which is characteristic to the Fe-O bond. This is an indication of the presence of the Fe<sub>3</sub>O<sub>4</sub> core [179]. The absorption peaks at 3425 cm<sup>-1</sup> and 1720 cm<sup>-1</sup> are attributed to the vibration of the -OH group and stretching of C=O group of the oleic acid which is the capping agent of the MNPs [92]. The broad absorption band at 1092 cm<sup>-1</sup> corresponds to Si-O-Si stretching vibration of mesoporous SiO<sub>2</sub>. The vibration band of the CH<sub>2</sub> group of the CTAB template is seen in the Fe<sub>3</sub>O<sub>4</sub>-SiO<sub>2</sub>-CTAB spectra at 2760 cm<sup>-1</sup>

and  $2925\text{ cm}^{-1}$  which was absent in the below spectra of  $\text{Fe}_3\text{O}_4\text{-SiO}_2$ . This confirmed that the template was successfully removed by the  $\text{NH}_4\text{NO}_3$  leaching.

The vibration of the  $\text{NH}_2$  group in chitosan at  $2750\text{ cm}^{-1}$  is overlapped by the absorption band of the  $\text{-OH}$  group. During coating the chitosan amino groups forms imine ( $\text{C=N}$ ) group. The CN group absorption band was observed in the  $\text{Fe}_3\text{O}_4\text{-SiO}_2\text{-Chitosan}$  spectra at  $1612\text{ cm}^{-1}$  which proves the successful attachment of the chitosan coating over the mesoporous  $\text{SiO}_2$  coating [180].

#### 4.4 VSM Data Analysis

The M-H curves of the bare and coated MNPs were constructed from the data received from the PPMS experiments. The data was then fitted to the Langevin function represented by the equation 2.3 mentioned in chapter 2. Figure 4–10 below shows the M-H curves of bare,  $\text{SiO}_2$  coated, and  $\text{SiO}_2\text{-Chitosan}$  coated  $\text{Fe}_3\text{O}_4$  MNPs.

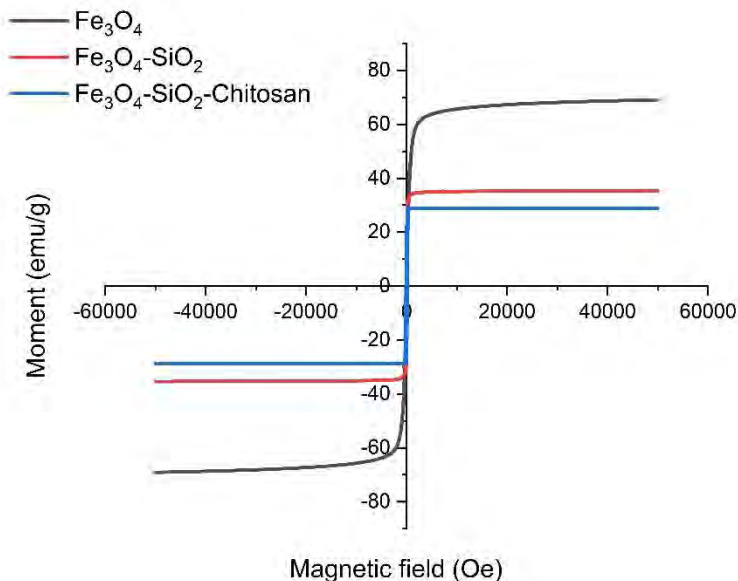


Figure 4–16: M-H curves of bare  $\text{Fe}_3\text{O}_4$ ,  $\text{SiO}_2$  coated  $\text{Fe}_3\text{O}_4$  and  $\text{SiO}_2\text{-Chitosan}$  coated  $\text{Fe}_3\text{O}_4$  MNPs.

It was evident even from the visual observation of the curves that the samples exhibited superparamagnetic properties, as no visible loops can be seen i.e., no magnetic remanence. The superparamagnetism was further confirmed by the fitting of the Langevin function on the curves. The saturation magnetization of each sample was also calculated from the Langevin function

fitting. Based on the values of the calculated adjusted linear regression coefficient (adj.  $R^2$ ) of the sample M–H curves it can be concluded that the fitting to the Langevin function was almost perfect in all three cases and all samples exhibited superparamagnetism. The data of the Langevin function fitting is summarized in table 4–2.

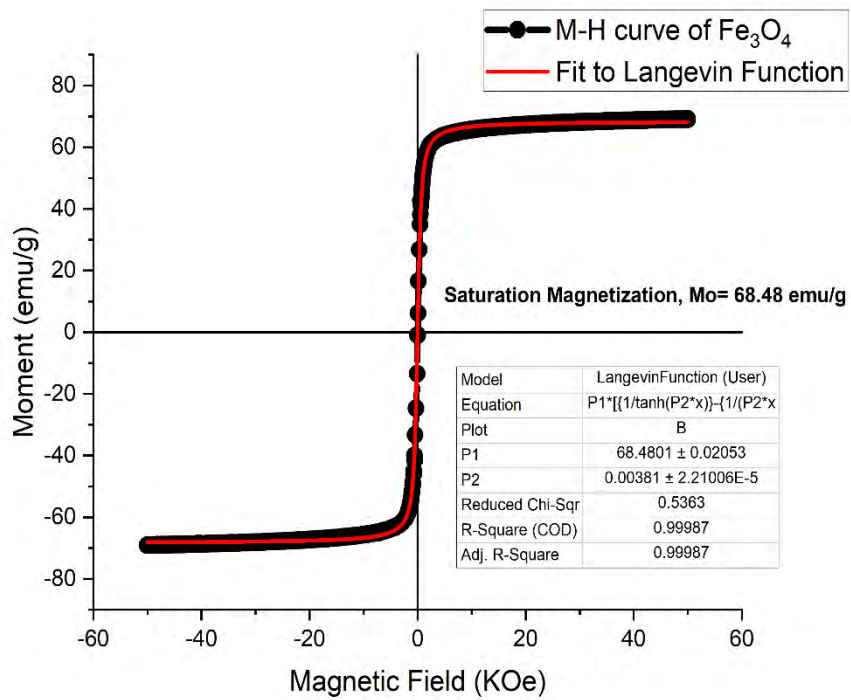
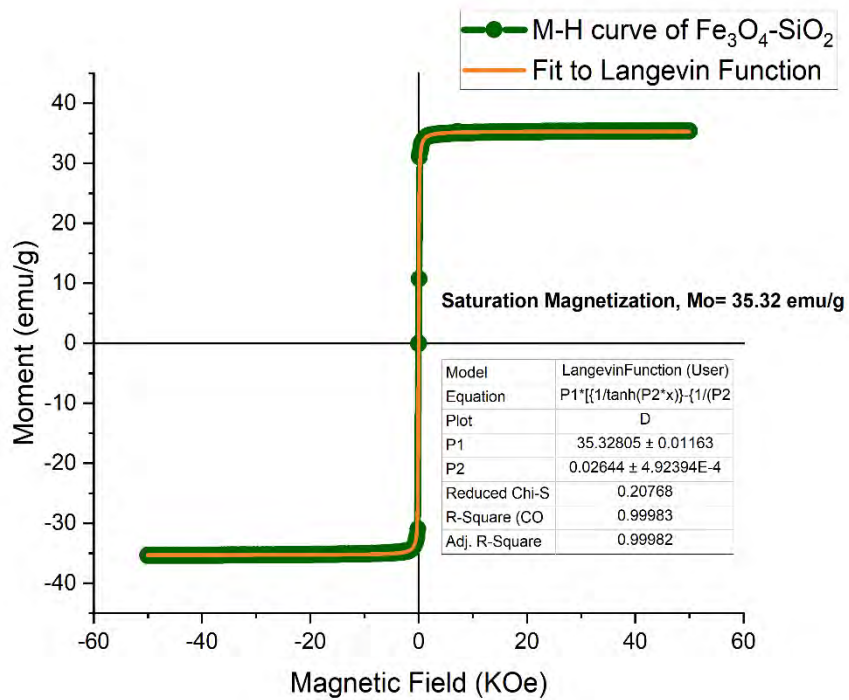
Table 4–2: Result of Langevin function fitting to the VSM data.

Sample	Saturation Magnetization, $M_o$ (emu/g)	Adj. $R^2$ to Langevin fitting
Bare $Fe_3O_4$	68.48	0.99987
$SiO_2$ coated $Fe_3O_4$	35.32	0.99952
Chitosan- $SiO_2$ coated $Fe_3O_4$	28.84	0.9987

The Langevin function fitted curves are illustrated in the figures 4–11, 4–12, and 4–13. It is seen from the VSM data that the saturation magnetization  $M_o$  of the adsorbent is 28.84 emu/g. Compared to  $M_o$  of other magnetic adsorbents reported by various studies, the obtained result is satisfactory as the adsorbents can be easily separated from solution with external magnetic field. A comparison between the magnetic properties of the developed adsorbent with other magnetic adsorbents reported by other research groups are given in table 4–3.

Table 4–3: Comparison of magnetic properties of various reported magnetic adsorbents.

Adsorbent	Saturation Magnetization (emu/g)	Reference
$Fe_3O_4$ - $SiO_2$ -Chitosan	28.84	This work
$Fe_3O_4@SiO_2-NH_2$	34.0	[64]
$Fe_3O_4$ -Chitosan	40.2	[106]
$Fe_3O_4@PAA@TSH$	33	[3]
$Fe_3O_4$ -Chitosan	27	[4]

Figure 4–17: Langevin function fitting to the M-H curve of bare  $\text{Fe}_3\text{O}_4$  MNPs.Figure 4–20: Langevin function fitting to the M-H curve of  $\text{SiO}_2$  coated  $\text{Fe}_3\text{O}_4$  MNPs.

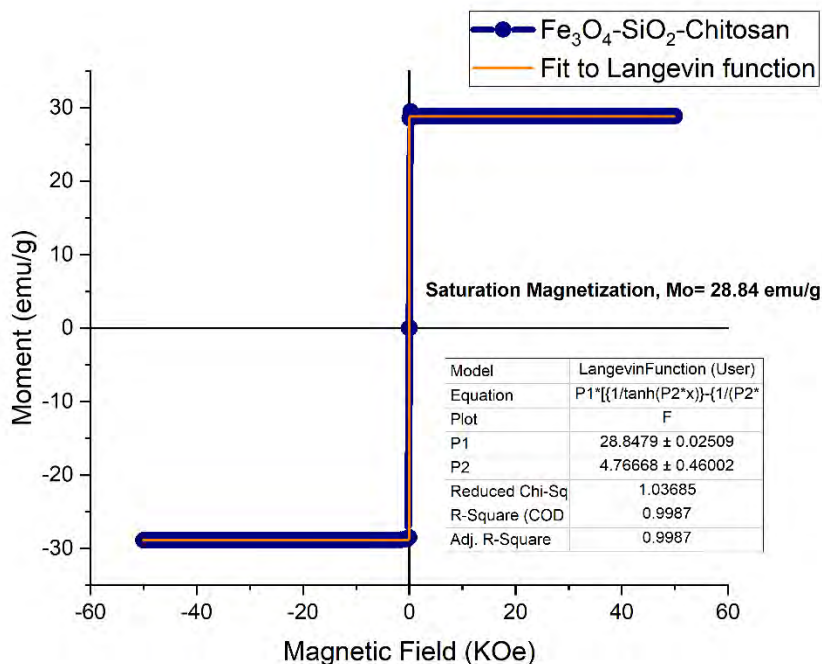


Figure 4–23: Langevin function fitting to the M-H curve of SiO<sub>2</sub>-Chitosan coated Fe<sub>3</sub>O<sub>4</sub> MNPs.

The saturation magnetization of double coated adsorbents is logically lower than the single coated adsorbents. But the  $M_0$  is yet higher than some reported adsorbents which gave satisfactory performances regarding magnetic separation.

#### 4.5 Adsorption Data Analysis

Analysis of the adsorption data received from the AAS measurements is the most important part of this entire study. The results from the adsorption data analysis will determine whether the developed MNPs can be effectively used as sustainable heavy metal adsorbents. The adsorption mechanism and capacity is calculated by fitting the adsorption data to the adsorption kinetic models and adsorption isotherm models. The data from this work was fitted to the mostly utilized kinetic models- pseudo first order and pseudo second order. The two most popular isotherm

models were compared to the obtained data- the Langmuir isotherm model and the Freundlich isotherm model.

The adsorption data can be classified into two distinct sections. In the first section, the variable parameter was the contact time and the fixed parameter was the initial concentration of the heavy metal salt solution. The data from the first section was used for the kinetic model fitting. The first section experimental data is summarized in table 4–4 below.

The adsorption capacity  $q$  is calculated by the equation 2.5. The volume of the liquid solution ( $V$ ) was 100 mL, the mass of the added adsorbent  $W$  was 50 mg for  $Pb^{2+}$  and  $Cd^{2+}$  solutions and 5 mg for  $As^{3+}$  solution.

Table 4–4: Adsorption data of  $Pb^{2+}$ ,  $Cd^{2+}$ , and  $As^{3+}$  with variable contact time.

Fixed parameter, initial concentration $C_i$ - 50 mg/L (50 $\mu$ g/L for As)									
Contact time, t minutes	Final concentration, $C_t$			Adsorption capacity at time t, $q_t$			Removal efficiency %		
	$Pb^{2+}$ (mg/L)	$Cd^{2+}$ (mg/L)	$As^{3+}$ ( $\mu$ g/L)	$Pb^{2+}$ (mg/g)	$Cd^{2+}$ (mg/g)	$As^{3+}$ ( $\mu$ g/g)	$Pb^{2+}$	$Cd^{2+}$	$As^{3+}$
0	50	50	50	0	0	0	0	0	0
5	7.56	11.3	18.32	84.88	77.4	633.6	84.88	77.4	63.36
10	3.65	7.76	12.43	92.7	84.48	751.4	92.7	84.48	75.14
15	2.91	5.78	3.56	94.18	88.44	928.8	94.18	88.44	92.88
20	2.36	5.32	1.96	95.28	89.36	960.8	95.28	89.36	96.08
30	2.34	5.27	1.67	95.32	89.44	966.6	95.32	89.44	96.66

The above data was plotted individually for  $Pb^{2+}$ ,  $Cd^{2+}$ , and  $As^{3+}$  to observe the effect of the contact time on the adsorption capacity of the adsorbent. It was seen that the adsorption reached equilibrium in about 5 minutes in the solution of  $Pb^{2+}$  and  $Cd^{2+}$ . For the  $As^{3+}$  solution the equilibrium was achieved after 15 minutes.

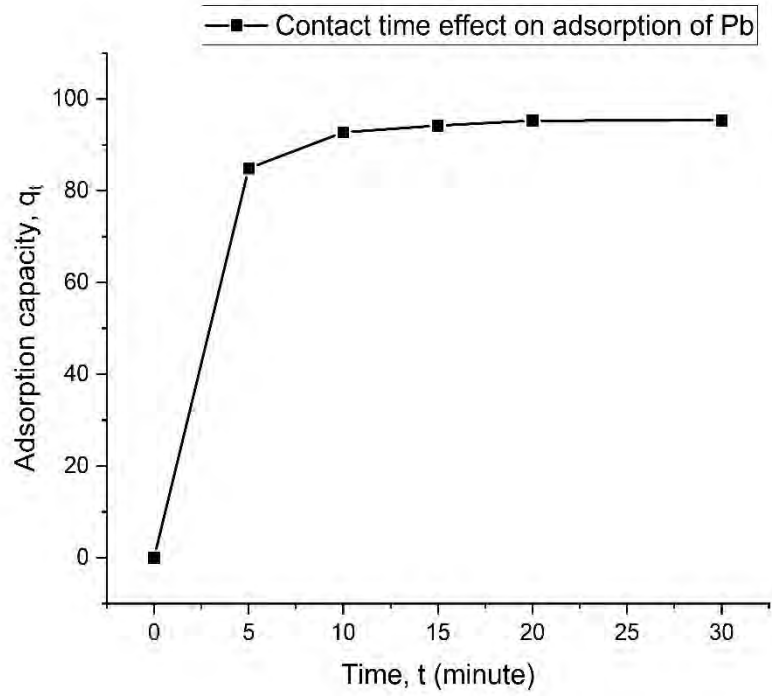


Figure 4–24: Contact time effect on the adsorption capacity of lead ( $Pb^{2+}$ ).

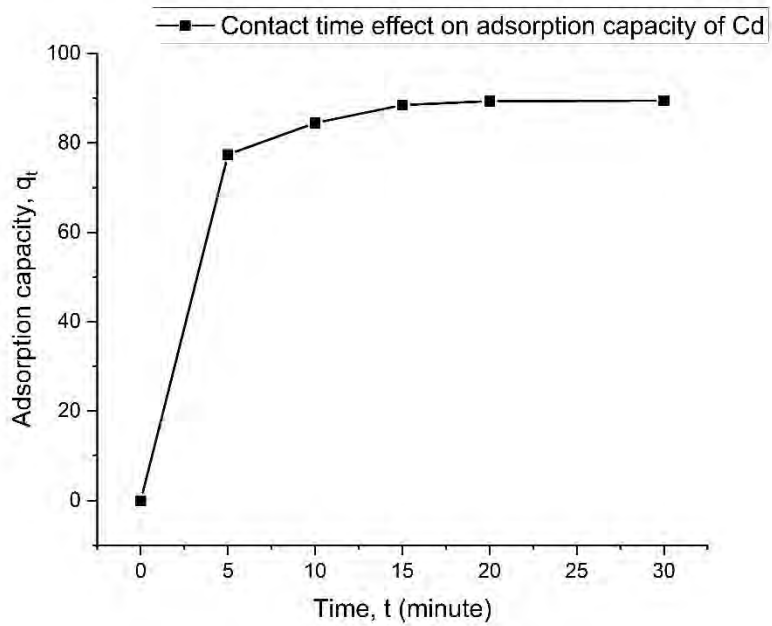


Figure 4–27: Contact time effect on the adsorption capacity of cadmium ( $Cd^{2+}$ ).

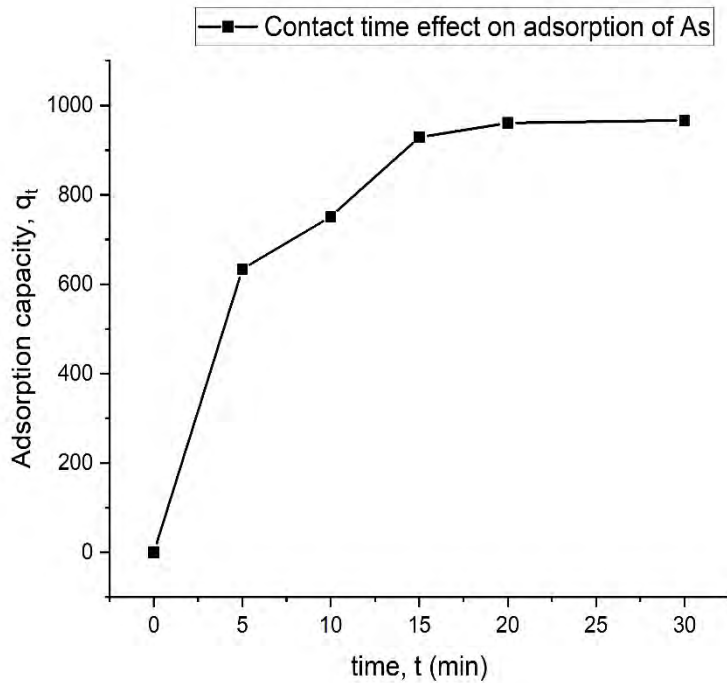


Figure 4–28: Contact time effect on the adsorption capacity of arsenic ( $\text{As}^{3+}$ ).

#### 4.5.1 Adsorption Kinetic Model Fitting

The pseudo first order kinetic model and the pseudo second order kinetic model are expressed by the equation 2.4 and equation 2.6 respectively, discussed in the literature review.

For the pseudo first order model fitting, the adsorption data is plotted as  $\ln(q_e - q_t)$  vs  $t$  where  $q_e$  is the adsorption capacity at equilibrium. The plot is then subjected to linear fitting. The adj.  $R^2$  is calculated to determine the degree of fit to the pseudo first order kinetic model. The intercept of the linear fitting gives the value of  $\ln q_e$  which consequently gives the value of the equilibrium adsorption capacity,  $q_e$ . This calculated value is compared to the experimental value of  $q_e$ . The slope of the linear fit is the value of  $k_1 t$  where  $k_1$  is the pseudo-first-order rate constant with the unit  $\text{min}^{-1}$ . The calculated data from the first order adsorption kinetic model fitting for  $\text{Pb}^{2+}$ ,  $\text{Cd}^{2+}$ , and  $\text{As}^{3+}$  is summarized in the table 4–5. The pseudo first order kinetic model fitting plots are illustrated in figures 4–17, 4–18, and 4–19.



Table 4–5: Parameters of the pseudo first order kinetic model fitting to the adsorption data.

Metal species	Adj. R <sup>2</sup>	k <sub>1</sub> (min <sup>-1</sup> )	Calculated q <sub>e</sub> (mg/g)	Experimental q <sub>e</sub> (mg/g)
Pb <sup>2+</sup>	0.92435	-0.0097	58.19	95.32
Cd <sup>2+</sup>	0.9248	-0.0083	53.69	89.44
As <sup>3+</sup>	0.76955	-0.0008	0.679	0.967

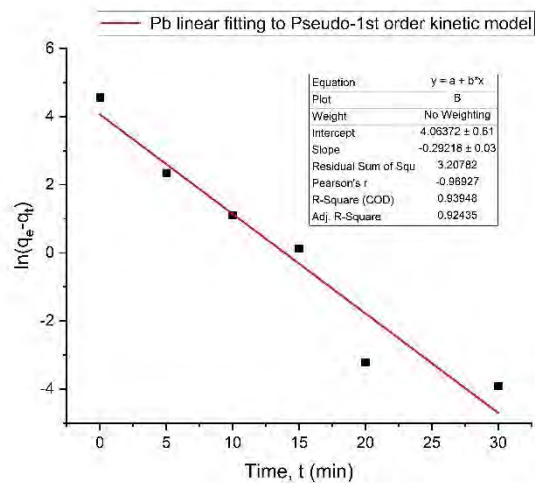


Figure 4–31: Lead (Pb<sup>2+</sup>) adsorption data fitting to the pseudo first order kinetic model.

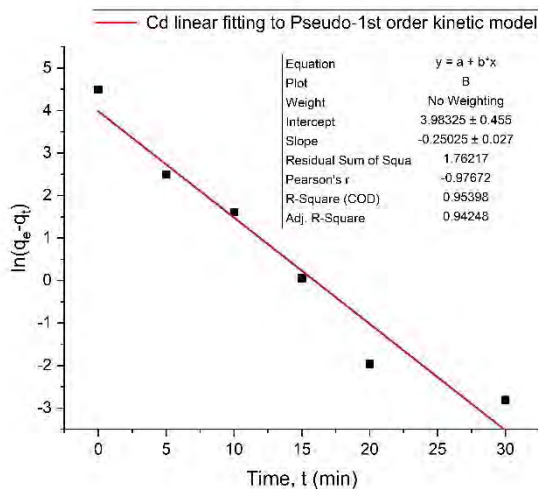


Figure 4–32: Cadmium (Cd<sup>2+</sup>) adsorption data fitting to the pseudo first order kinetic model.

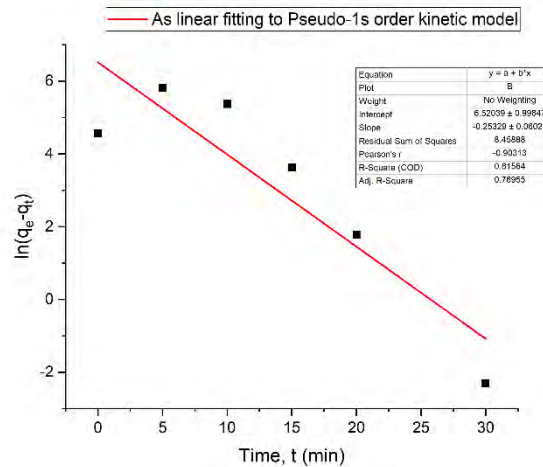


Figure 4–33: Arsenic ( $\text{As}^{3+}$ ) adsorption data fitting to the pseudo first order kinetic model.

For the pseudo second order kinetic model fitting, the adsorption data is plotted in the form  $t/q_t$  vs  $t$  where  $q_t$  is the adsorption capacity at the equilibrium. After applying linear fitting to the plot, the value of the intercept and slope is recorded. The value of the slope is equal to  $1/q_e$  where  $q_e$  is the equilibrium adsorption capacity. The intercept value is equal to  $\frac{1}{k_2 q_e^2}$  and  $k_2$  ( $\text{g mg}^{-1} \text{min}^{-1}$ ), the pseudo-second-order rate constant is calculated from this value. Comparison between the calculated  $q_e$  and the experimental  $q_e$  along with the value of adj.  $R^2$  can also be an indicator for model fitting. The calculated data of the pseudo second order kinetic model fitting are presented in table 4–6 below. The fitting plots are illustrated in figures 4–20, 4–21, and 4–22.

Table 4–6: Parameters of the pseudo second order kinetic model fitting to the adsorption data.

Metal species	Adj. $R^2$	$k_2$ ( $\text{g mg}^{-1} \text{min}^{-1}$ )	Calculated $q_e$ (mg/g)	Experimental $q_e$ (mg/g)
$\text{Pb}^{2+}$	0.9948	0.033	96.24	95.32
$\text{Cd}^{2+}$	0.9989	0.025	90.66	89.44
$\text{As}^{3+}$	0.9823	0.0005	1.01	0.967

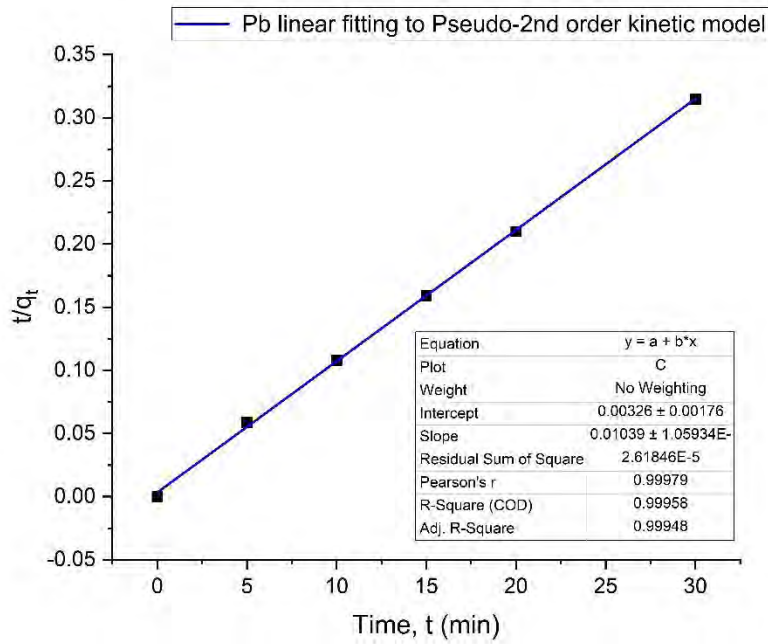


Figure 4–34: Lead ( $Pb^{2+}$ ) adsorption data fitting to the pseudo second order kinetic model.

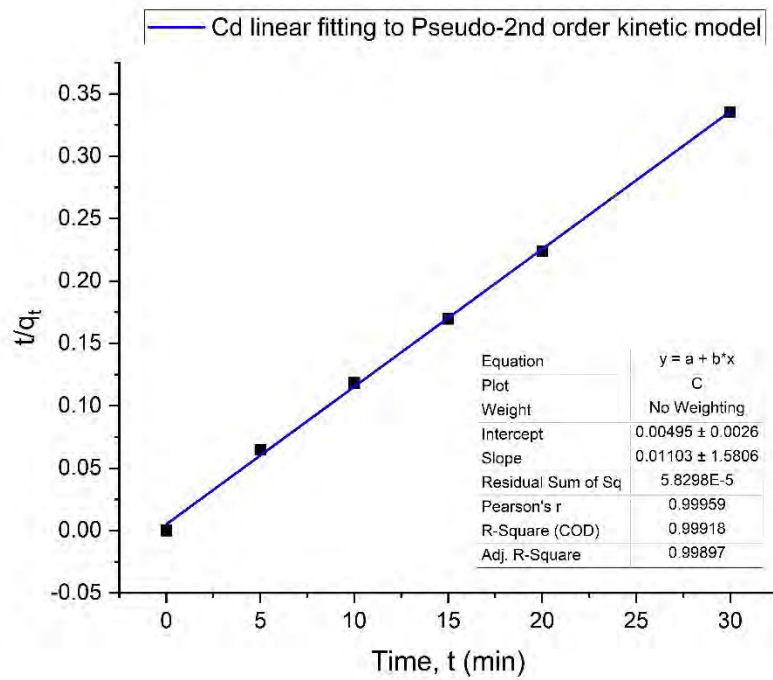


Figure 4–35: Cadmium ( $Cd^{2+}$ ) adsorption data fitting to the pseudo second order kinetic model.

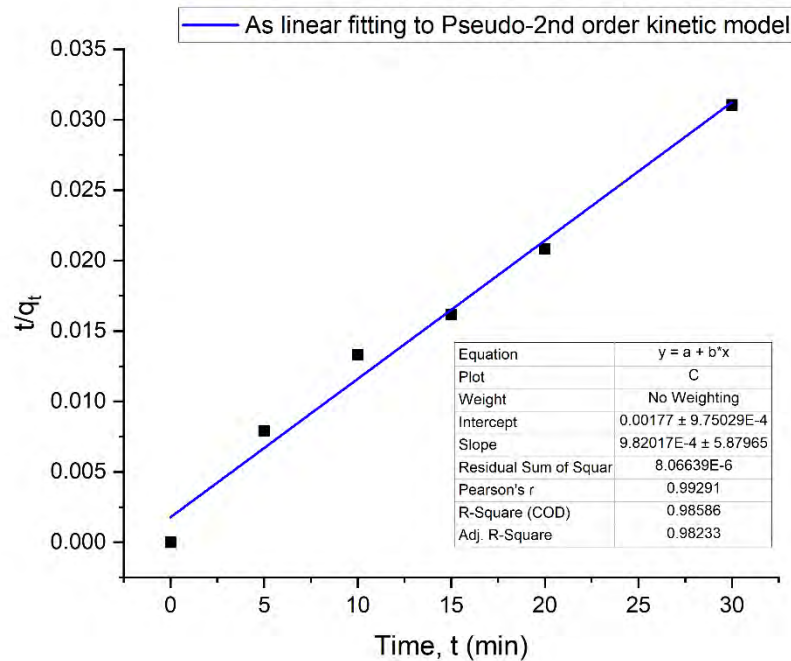


Figure 4–36: Arsenic ( $\text{As}^{3+}$ ) adsorption data fitting to the pseudo second order kinetic model.

The adj.  $R^2$  of  $\text{Pb}^{2+}$ ,  $\text{Cd}^{2+}$ , and  $\text{As}^{3+}$  adsorption data to the pseudo second order kinetic model fitting is closer to unity than the adj.  $R^2$  of fitting to the pseudo first order kinetic model. Based on the comparison of the linear regression coefficient adj.  $R^2$ , it is evident that the pseudo second order kinetic model is a better fit for the data in all three cases. The fitting plots also show a better fit to the pseudo second order kinetic model visually in all cases. Moreover, the calculated  $q_e$  from the pseudo second order kinetic model fitting is more compatible to the experimental  $q_e$  than the calculated  $q_e$  from the pseudo first order kinetic model regarding all three species. The better suitability of the data with the pseudo second kinetic model suggests that the nature of the adsorption is chemisorption [4]. This conclusion is also in agreement with the previously reported literature [4,73,179]. From the previous discussion it is known that chitosan adsorbs heavy metal ions through chelation which is a type of chemical bonding. Therefore, it can be concluded that the experimental data is compatible with the theory.

#### 4.5.2 Adsorption Isotherm Model Fitting

So far we have discussed the adsorption data with fixed initial solution concentration and variable contact time. The second section of the adsorption data is recorded interchanging the last two parameters. The data that is subjected to the adsorption isotherm model fitting is recorded with a constant contact time of 30 minutes which is the time required for achieving equilibrium. In this the case the initial concentration of the salt solution is varied from 10 mg/L upto 150 mg/L for  $\text{Pb}^{2+}$  and  $\text{Cd}^{2+}$ . For  $\text{As}^{3+}$  adsorption the initial solution was taken to be between 10  $\mu\text{g/L}$  to 150  $\mu\text{g/L}$ . The second set of adsorption data with fixed contact time of 30 minutes is summarized in table 4–7 below.

Table 4–7: Adsorption data of  $\text{Pb}^{2+}$ ,  $\text{Cd}^{2+}$ , and  $\text{As}^{3+}$  with variable initial solution concentration.

Fixed parameter, Contact time $t = 30$ minutes										
Initial concentration, $C_i$		Final concentration, $C_t$			Adsorption capacity at equilibrium, $q_e$			Removal efficiency %		
$\text{Pb}^{2+}$ , $\text{Cd}^{2+}$ (mg/L)	As ( $\mu\text{g/L}$ )	$\text{Pb}^{2+}$ (mg/L)	$\text{Cd}^{2+}$ (mg/L)	$\text{As}^{3+}$ ( $\mu\text{g/L}$ )	$\text{Pb}^{2+}$ (mg/g)	$\text{Cd}^{2+}$ (mg/g)	$\text{As}^{3+}$ ( $\mu\text{g/g}$ )	$\text{Pb}^{2+}$	$\text{Cd}^{2+}$	$\text{As}^{3+}$
10	10	0.66	0.62	0.13	18.68	18.76	197.4	93.4	93.8	98.7
20	25	0.99	0.94	0.67	38.02	38.12	486.6	95.05	95.3	97.32
30	50	1.94	1.89	1.67	56.12	56.22	966.6	93.53	93.7	96.66
50	75	2.34	5.27	2.05	95.32	89.44	1459	95.32	89.46	97.27
100	100	6.19	7.65	2.28	187.62	184.7	1954.4	93.81	92.35	97.72
150	150	20.36	14.49	3.46	259.28	271.02	2930.8	86.43	90.34	97.7

The Langmuir isotherm model is expressed by the equation 2.9. the adsorption data is fitted to the Langmuir isotherm model by plotting  $1/q_e$  vs  $1/C_e$  where  $q_e$  and  $C_e$  are the equilibrium adsorption capacity and heavy metal concentration in the solution at equilibrium respectively.

After fitting the intercept is calculated. The value of the intercept is equal to  $1/q_{\max}$  where  $q_{\max}$  is the maximum adsorption capacity of the adsorbent for the specific heavy metal species. The Langmuir equilibrium constant  $K_L$  with the unit  $L\ mg^{-1}$  is calculated from the slope of the linear fitting since,  $K_L = \frac{1}{\text{slope} \times q_{\max}}$ . The value of  $K_L$  is used in the calculation of the separation factor  $R_L$  whose value indicates if the adsorption condition is favorable or unfavorable.  $R_L$  is calculated by the equation 2.10. The calculated parameters of the Langmuir isotherm model fitting for  $Pb^{2+}$ ,  $Cd^{2+}$ , and  $As^{3+}$  are given in table 4–8. The Langmuir fitting plots are illustrated in figures 4–23, 4–24, and 4–25.

Table 4–8: Parameters of the Langmuir isotherm model fitting to the adsorption data.

Metal species	Adj. R <sup>2</sup>	$q_{\max}$ (mg/g)	$K_L$ (L mg <sup>-1</sup> )	$R_L$ (g mg <sup>-1</sup> min)
Pb <sup>2+</sup>	0.997	151.98	0.209	0.088
Cd <sup>2+</sup>	0.993	144.51	0.238	0.084
As <sup>3+</sup>	0.992	3.021	0.533	0.158

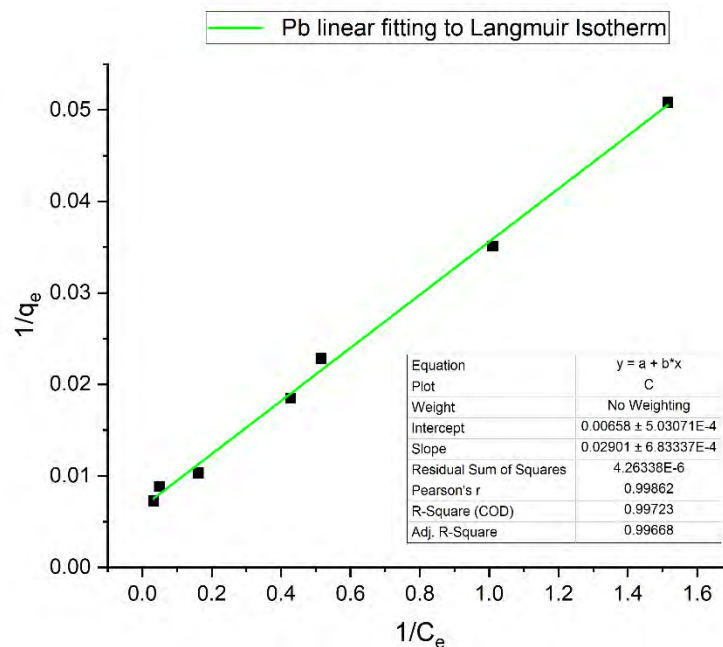


Figure 4–39: Lead ( $Pb^{2+}$ ) adsorption data fitting to the Langmuir isotherm model.

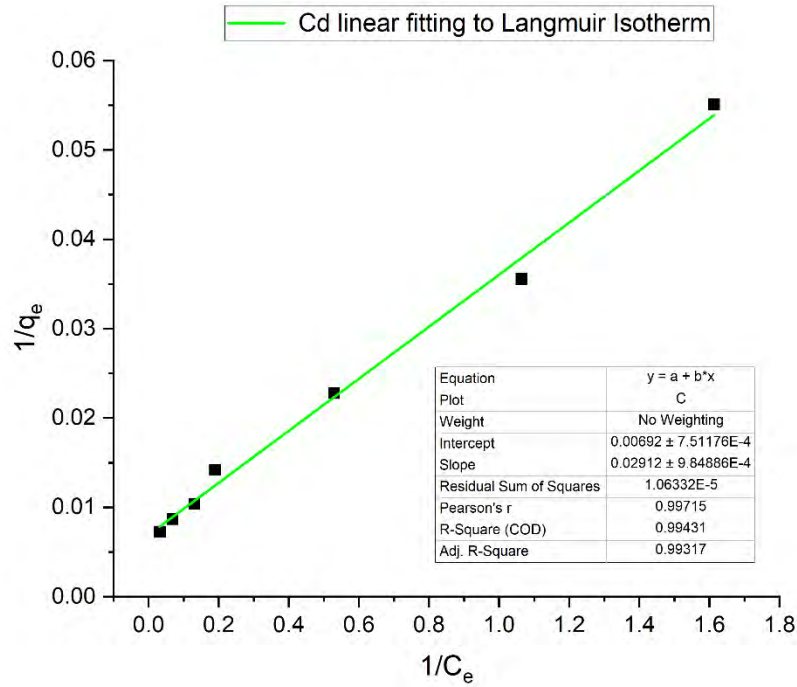


Figure 4–40: Cadmium ( $\text{Cd}^{2+}$ ) adsorption data fitting to the Langmuir isotherm model.

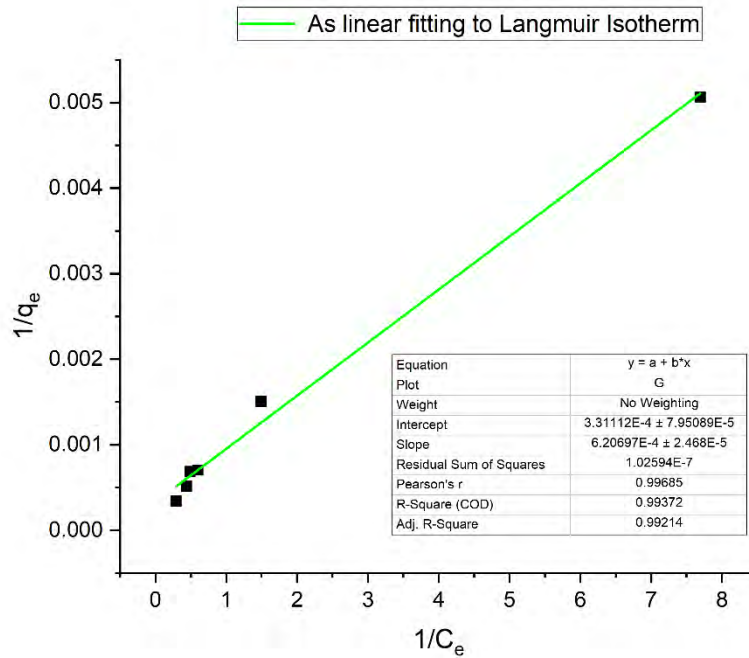


Figure 4–41: Arsenic ( $\text{As}^{3+}$ ) adsorption data fitting to the Langmuir isotherm model.

It was observed that the value of  $R_L$  was well within the range of  $0 < R_L < 1$  for all three adsorbates. Therefore, the adsorption conditions were favorable for reversible adsorption mechanism. This is in agreement with the adsorption mechanism of chitosan which is reversible in nature.

The Freundlich isotherm model is fitted to adsorption data by plotting  $\log q_e$  vs  $\log C_e$  and subjecting the plot to linear fitting. The slope of the linear fitting gives the value of  $1/n$  which is the adsorption intensity. The value of  $1/n$  dictates the favorable or unfavorable conditions for adsorption. The intercept of the linear fitting has the value  $\log K_F$  where  $K_F$  is the Freundlich constant with the unit  $\text{mg g}^{-1}(\text{mg L}^{-1})^{-1/n}$ . The calculated parameters of the Freundlich isotherm model fitting for  $\text{Pb}^{2+}$ ,  $\text{Cd}^{2+}$ , and  $\text{As}^{3+}$  are given in table 4–9. The Freundlich fitting plots are illustrated in figures 4–26, 4–27, and 4–28.

Table 4–9: Parameters of the Freundlich isotherm model fitting to the adsorption data.

Metal species	Adj. $R^2$	$1/n$	$K_F \text{ mg g}^{-1}(\text{mg L}^{-1})^{-1/n}$
$\text{Pb}^{2+}$	0.936	0.74	35.9
$\text{Cd}^{2+}$	0.936	1.41	37.1
$\text{As}^{3+}$	0.934	0.8	851.1

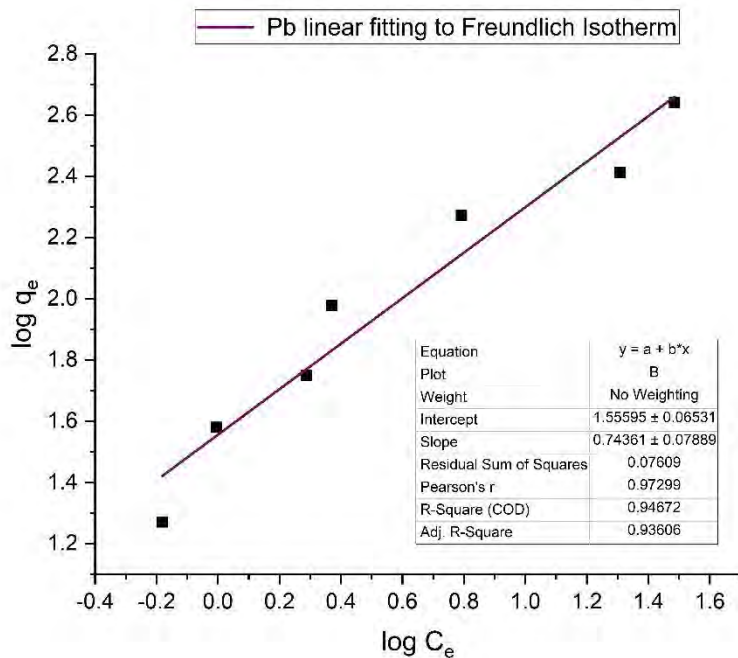


Figure 4–42: Lead ( $\text{Pb}^{2+}$ ) adsorption data fitting to the Freundlich isotherm model.



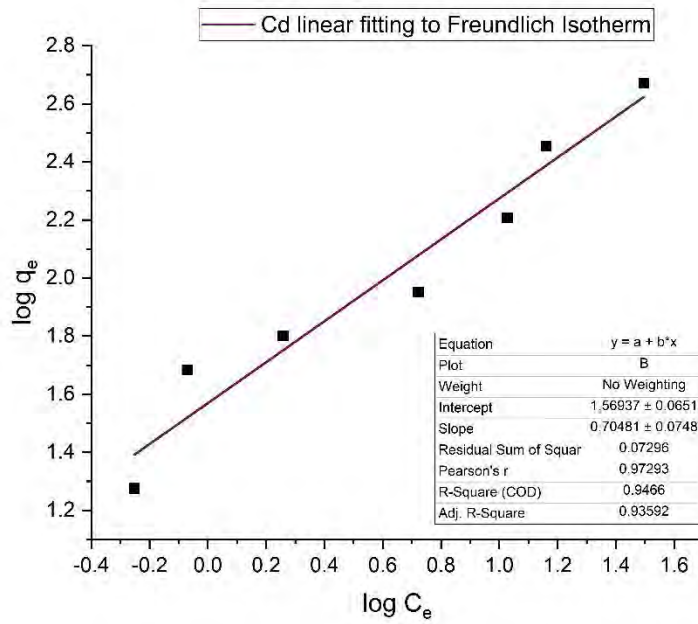


Figure 4–43: Cadmium ( $\text{Cd}^{2+}$ ) adsorption data fitting to the Freundlich isotherm model.

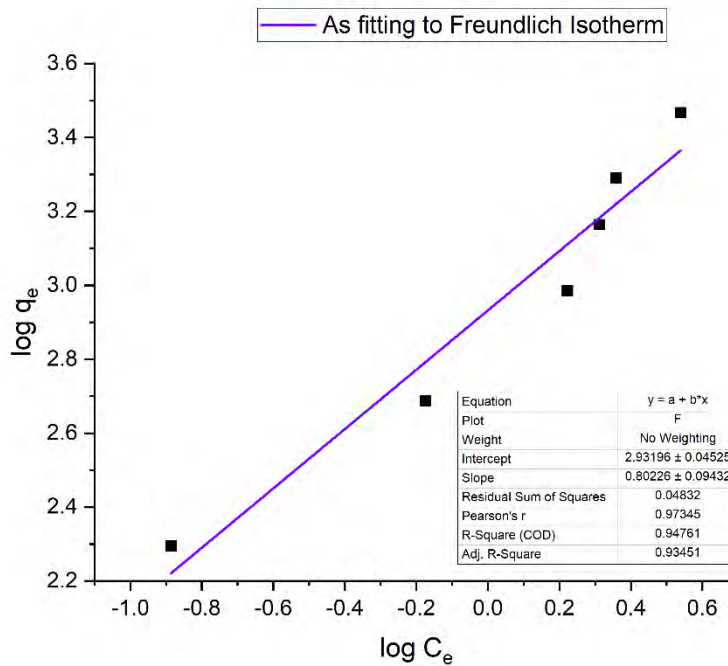


Figure 4–44: Arsenic ( $\text{As}^{3+}$ ) adsorption data fitting to the Freundlich isotherm model.

It is evident from the above results that in case of all three species, the adj.  $R^2$  for the Langmuir fitting is greater than the adj.  $R^2$  of the Freundlich fitting. Based on the value of adj.  $R^2$  the Langmuir adsorption isotherm model is a more suitable match for this adsorption study. Moreover, the calculated values of the adsorption intensity  $1/n$  for  $Pb^{2+}$ ,  $Cd^{2+}$ , and  $As^{3+}$  derived from the Freundlich isotherm fitting do not fall between the favorable condition of  $0.1 < 1/n < 0.5$ . This is another reason for the Freundlich isotherm model not being the suitable model for this study. The physical significance of the Langmuir isotherm model being the suitable one verifies that the adsorption in this study is monolayer in nature which is similar to other reported adsorption study of chitosan based adsorbents [4,73].

Table 4–10 contains a relative comparison between the maximum adsorption capacity of the developed  $Fe_3O_4-SiO_2$ -Chitosan adsorbent for  $Pb^{2+}$ ,  $Cd^{2+}$ , and  $As^{3+}$  and the maximum adsorption capacity achieved with other types of adsorbents for the same metals. The adsorption capacity for  $Pb^{2+}$  and  $Cd^{2+}$  of the  $Fe_3O_4-SiO_2$ -Chitosan adsorbent is 150.33 mg/g and 126.26 mg/g respectively which higher than most of the polymer modified and surfactant coated magnetic adsorbents. Based on the observed adsorption capacity, the developed adsorbent can be used as an efficient  $Pb^{2+}$  and  $Cd^{2+}$  removal agent from water.

The observed adsorption capacity for  $As^{3+}$  is much lower than the  $Pb^{2+}$  and  $Cd^{2+}$ . Although the adsorption capacity for  $As^{3+}$  is generally lower than heavy metals since arsenic is a metalloid. However, the significantly lower adsorption capacity in this study may have been caused by the different concentration levels of the  $As^{3+}$  solutions. The AAS facility where the solution concentrations were measured was not equipped to measure  $As^{3+}$  concentration above 50  $\mu\text{g/L}$ . Therefore, the  $As^{3+}$  adsorption experiments were conducted with 1000 times diluted solutions than the  $Pb^{2+}$  and  $Cd^{2+}$  solutions. But it was not possible to reduce the adsorbent amount by the same ratio due to instrumental limitations. The difference in these experiment parameters may have contributed to the lower adsorption capacity for  $As^{3+}$ . Based on the observed performance of the developed adsorbent, it can be used as an efficient  $Pb^{2+}$  and  $Cd^{2+}$  removal agent from water.

Table 4–10: Comparison of maximum adsorption capacity of current work and other reported adsorbents.

Adsorbent type	Adsorption capacity, Pb <sup>2+</sup> mg/g	Adsorption capacity, Cd <sup>2+</sup> mg/g	Adsorption capacity, As <sup>3+</sup> mg/g	Ref.
Fe <sub>3</sub> O <sub>4</sub> -SiO <sub>2</sub> -Chitosan	150.33	126.26	3.021	This work
Fe <sub>3</sub> O <sub>4</sub> @PAA@TSC MNPs	181.1	125	–	[3]
Amino-functionalized Fe <sub>3</sub> O <sub>4</sub> @SiO <sub>2</sub> MNPs	76.6	–	–	[64]
Polymer-modified Fe <sub>3</sub> O <sub>4</sub> nanoparticles	100.66	29.9	–	[63]
Salicylic acid type chelate adsorbent	86.1	57.1	–	[181]
TiO <sub>2</sub> -impregnated chitosan bead	–	–	2.10	[100]
Fe <sub>3</sub> O <sub>4</sub> -chitosan-Polyethylenimine nanocomposite	–	–	77.6	[182]
Synthesized surfactant coated Fe <sub>3</sub> O <sub>4</sub>	42.37	42.55	–	[61]

### 4.5.3 Desorption Study

A desorption study was conducted for the adsorbent MNPs used for the Pb<sup>2+</sup> and Cd<sup>2+</sup> adsorption experiments to explore the possibility of recovery and leaching of the magnetic core in acidic environment. The composition of the desorption solution is given in table 4–11.

Table 4–11: Concentration profile of desorption solution.

<b>Metal species</b>	<b>Concentration (mg/L)</b>
Pb <sup>2+</sup>	31.56
Cd <sup>2+</sup>	23.45
Fe <sup>3+</sup>	0.04

The Pb<sup>2+</sup> and Cd<sup>2+</sup> concentration in the desorption solution was released from the adsorbent surface. The Fe<sup>3+</sup> presence proves a very negligible amount of leaching in the weak acidic environment. Therefore, the Fe<sub>3</sub>O<sub>4</sub>-SiO<sub>2</sub>-Chitosan nano-adsorbent can be sustainably used more than once without any damage to the magnetic core

## 5 Chapter 5: Conclusion & Recommendation

### 5.1 Concluding Remarks

The objective of this work was to synthesize novel magnetic magnetite ( $\text{Fe}_3\text{O}_4$ ) nanoparticles with chitosan–mesoporous silica coating and to evaluate their efficiency in heavy metal removal from water along with their recoverability via desorption. The goal was successfully achieved as the developed MNPs exhibited excellent adsorption capacity for lead and cadmium from water. The MNPs also showed potential for easy recovery via a simple desorption in weakly acidic medium keeping the integrity of the magnetic core. The arsenic adsorption capacity may have been altered due to the experimental parameter change.

The overall synthesis process of the adsorbent was chosen to be the most feasible. Thermal decomposition procedure for the magnetic nanoparticle production was deemed to be the most suitable procedure for obtaining monodisperse MNPs. The magnetic properties of the coated and uncoated MNPs were sufficient for simple magnetic separation. The mesoporous silica and chitosan coating on the MNPs were formed fruitfully via an efficient and economically feasible method. The presence of the coating on the MNPs and the overall morphology and structure properties were determined using XRD, TEM, EDS, FTIR, VSM characterization techniques. The analysis of the AAS data from the adsorption experiment revealed critical information about the adsorption capacity and mechanism.

This thesis work can be concluded with the following remarks-

- ✓ Desired magnetic and morphological property was achieved in  $\text{Fe}_3\text{O}_4$  nanoparticles via thermal decomposition procedure.
- ✓ MNPs were successfully coated with mesoporous silica and chitosan.
- ✓ Coated MNPs were successfully used as adsorbents for  $\text{Pb}^{2+}$ ,  $\text{Cd}^{2+}$ , and  $\text{As}^{3+}$  from water with reversible adsorption.
- ✓ The adsorption capacity of the adsorbent for  $\text{Pb}^{2+}$ ,  $\text{Cd}^{2+}$ , and  $\text{As}^{3+}$  was 150.33 mg/g, 126.26 mg/g, and 3.021 mg/g respectively.

- ✓ The coating was successful in preventing Fe leaching during recovery/desorption and oxidation of the magnetic core.
- ✓ The analysis of the adsorption data represents the adsorption mechanism as monolayer chemisorption.

## 5.2 Recommendations for Future Prospect

This study has provided multiple pathways in heavy metal adsorption to be explored. Some possible routes for further research can be-

- The developed adsorbent's capacity in removing other heavy metals such as chromium (Cr), mercury (Hg), etc. can be studied.
- The adsorption study of  $As^{3+}$  could be studied at more concentrated level to find out the reason of discrepancy between the adsorption capacity with  $Pb^{2+}$  and  $Cd^{2+}$ .
- The adsorbent can be used to remove heavy metals from mixed solutions containing more than one metal species, wastewater collected from local sources, or water collected from natural reserves to study the effect of multiple constituents on adsorption capacity and mechanism as well as the preferential order of adsorption.
- Different magnetic nanoparticle synthesis procedures can be employed to study the difference in the magnetic and morphological properties of the adsorbent.

## 6 References

1. Villarín MC, Merel S. Paradigm shifts and current challenges in wastewater management. *J Hazard Mater* [Internet]. 2020;390:122139. Available from: <https://www.sciencedirect.com/science/article/pii/S0304389420301278>
2. Hong J, Xie J, Mirshahghassemi S, Lead J. Metal (Cd, Cr, Ni, Pb) removal from environmentally relevant waters using polyvinylpyrrolidone-coated magnetite nanoparticles. *RSC Adv*. 2020;10(6):3266–76.
3. Zargoosh K, Zilouei H, Mohammadi MR, Abedini H. 4-Phenyl-3-thiosemicarbazide modified magnetic nanoparticles: Synthesis, characterization and application for heavy metal removal. *Clean - Soil, Air, Water*. 2014;42(9):1208–15.
4. Ayub A, Raza ZA, Majeed MI, Tariq MR, Irfan A. Development of sustainable magnetic chitosan biosorbent beads for kinetic remediation of arsenic contaminated water. *Int J Biol Macromol* [Internet]. 2020;163:603–17. Available from: <https://doi.org/10.1016/j.ijbiomac.2020.06.287>
5. Fu X, Chen X, Wang J, Liu J. Fabrication of carboxylic functionalized superparamagnetic mesoporous silica microspheres and their application for removal basic dye pollutants from water. *Microporous Mesoporous Mater* [Internet]. 2011;139(1):8–15. Available from: <https://www.sciencedirect.com/science/article/pii/S1387181110003331>
6. Egodawatte S, Datt A, Burns EA, Larsen SC. Chemical Insight into the Adsorption of Chromium(III) on Iron Oxide/Mesoporous Silica Nanocomposites. *Langmuir*. 2015;31(27):7553–62.
7. Gan Q, Zhu J, Yuan Y, Liu H, Qian J, Li Y, et al. A dual-delivery system of pH-responsive chitosan-functionalized mesoporous silica nanoparticles bearing BMP-2 and dexamethasone for enhanced bone regeneration. *J Mater Chem B* [Internet]. 2015;3:2056–66. Available from: <https://pubs.rsc.org/en/content/articlelanding/2015/tb/c4tb01897d/unauth>
8. Jiang FY, Wang CM, Fu Y, Liu RC. Synthesis of iron oxide nanocubes via microwave-assisted solvothermal method. *J Alloys Compd* [Internet]. 2010;503(2):L31–3. Available from: <https://www.sciencedirect.com/science/article/pii/S0925838810011370>
9. Zhen G, Muir BW, Moffat BA, Harbour P, Murray KS, Moubaraki B, et al. Comparative Study of the Magnetic Behavior of Spherical and Cubic Superparamagnetic Iron Oxide Nanoparticles. *J Phys Chem C* [Internet]. 2011 Jan 20;115(2):327–34. Available from: <https://doi.org/10.1021/jp104953z>
10. Hatakeyama M, Kishi H, Kita Y, Imai K, Nishio K, Karasawa S, et al. A two-step ligand exchange reaction generates highly water-dispersed magnetic nanoparticles for biomedical applications. *J Mater Chem* [Internet]. 2011;21(16):5959–66. Available from:

<http://dx.doi.org/10.1039/C0JM04381H>

11. Tsang SC, Caps V, Paraskevas I, Chadwick D, Thompsett D. Magnetically Separable, Carbon-Supported Nanocatalysts for the Manufacture of Fine Chemicals. *Angew Chemie Int Ed [Internet]*. 2004 Oct 25;43(42):5645–9. Available from: <https://doi.org/10.1002/anie.200460552>
12. Lu A-H, Salabas EL, Schüth F. Magnetic Nanoparticles: Synthesis, Protection, Functionalization, and Application. *Angew Chemie Int Ed [Internet]*. 2007;46(8):1222–44. Available from: <https://onlinelibrary.wiley.com/doi/abs/10.1002/anie.200602866>
13. GREENWOOD NN, EARNSHAW ABT-C of the E (Second E, editors. 25 - Iron, Ruthenium and Osmium. In *Oxford: Butterworth-Heinemann*; 1997. p. 1070–112. Available from: <https://www.sciencedirect.com/science/article/pii/B9780750633659500316>
14. Bagbi Y, Sarswat A, Mohan D, Pandey A, Solanki PR. Lead (Pb<sup>2+</sup>) adsorption by monodispersed magnetite nanoparticles: Surface analysis and effects of solution chemistry. *J Environ Chem Eng*. 2016;4(4):4237–47.
15. Lee J, Isobe T, Senna M. Magnetic properties of ultrafine magnetite particles and their slurries prepared via in-situ precipitation. *Colloids Surfaces A Physicochem Eng Asp [Internet]*. 1996;109:121–7. Available from: <https://www.sciencedirect.com/science/article/pii/092777579503479X>
16. Willis AL, Turro NJ, O'Brien S. Spectroscopic Characterization of the Surface of Iron Oxide Nanocrystals. *Chem Mater [Internet]*. 2005 Nov 1;17(24):5970–5. Available from: <https://doi.org/10.1021/cm051370v>
17. O'Brien S, Brus L, Murray CB. Synthesis of Monodisperse Nanoparticles of Barium Titanate: Toward a Generalized Strategy of Oxide Nanoparticle Synthesis. *J Am Chem Soc [Internet]*. 2001 Dec 1;123(48):12085–6. Available from: <https://doi.org/10.1021/ja011414a>
18. Nemati Z, Das R, Alonso J, Clements E, Phan MH, Srikanth H. Iron Oxide Nanospheres and Nanocubes for Magnetic Hyperthermia Therapy: A Comparative Study. *J Electron Mater*. 2017;46(6):3764–9.
19. Dewi MR, Skinner WM, Nann T. Synthesis and phase transfer of monodisperse iron oxide (Fe<sub>3</sub>O<sub>4</sub>) nanocubes. *Aust J Chem*. 2014;67(4):663–9.
20. Nikitin A, Fedorova M, Naumenko V, Shchetinin I, Abakumov M, Erofeev A, et al. Synthesis, characterization and MRI application of magnetite water-soluble cubic nanoparticles. *J Magn Magn Mater*. 2017;441:6–13.
21. Wang D, Ma Q, Yang P. Synthesis of Fe<sub>3</sub>O<sub>4</sub> nanoparticles with tunable and uniform size through simple thermal decomposition. *J Nanosci Nanotechnol*. 2012;12(8):6432–8.
22. Yu WW, Falkner JC, Yavuz CT, Colvin VL. Synthesis of monodisperse iron oxide nanocrystals by thermal decomposition of iron carboxylate salts. *Chem Commun*. 2004;(20):2306–7.



23. Lin MM, Kim DK. In situ thermolysis of magnetic nanoparticles using non-hydrated iron oleate complex. *J Nanoparticle Res.* 2012;14(2).
24. Park J, An K, Hwang Y, Park JEG, Noh HJ, Kim JY, et al. Ultra-large-scale syntheses of monodisperse nanocrystals. *Nat Mater.* 2004;3(12):891–5.
25. Kim DK, Lee JW. Synthesis of non-hydrate iron oleate for eco-friendly production of monodispersed iron oxide nanoparticles. *J Korean Ceram Soc.* 2018;55(6):625–34.
26. Hufschmid R, Arami H, Ferguson RM, Gonzales M, Teeman E, Brush LN, et al. Synthesis of phase-pure and monodisperse iron oxide nanoparticles by thermal decomposition. *Nanoscale.* 2015;7:11142–54.
27. Chen Y, Johnson E, Peng X. Formation of Monodisperse and Shape-Controlled MnO Nanocrystals in Non-Injection Synthesis: Self-Focusing via Ripening. *J Am Chem Soc* [Internet]. 2007 Sep 1;129(35):10937–47. Available from: <https://doi.org/10.1021/ja073023n>
28. Li Y, Afzaal M, O'Brien P. The synthesis of amine-capped magnetic (Fe, Mn, Co, Ni) oxide nanocrystals and their surface modification for aqueous dispersibility. *J Mater Chem* [Internet]. 2006;16(22):2175–80. Available from: <http://dx.doi.org/10.1039/B517351E>
29. Shavel A, N LML-M. Chemistry and physics of metal oxide nanostructures. *Phys Chem Chem Phys.* 2009;11:3762–6.
30. LaMer VK, Dinegar RH. Theory, Production and Mechanism of Formation of Monodispersed Hydrosols. *J Am Chem Soc* [Internet]. 1950 Nov 1;72(11):4847–54. Available from: <https://doi.org/10.1021/ja01167a001>
31. Langevin D. Micelles and Microemulsions. *Annu Rev Phys Chem* [Internet]. 1992 Oct 1;43(1):341–69. Available from: <https://doi.org/10.1146/annurev.pc.43.100192.002013>
32. Paul BK, Moulik SP. Uses and applications of microemulsions. *Curr Sci* [Internet]. 2001 Apr 27;80(8):990–1001. Available from: <http://www.jstor.org/stable/24105809>
33. Gupta AK, Gupta M. Synthesis and surface engineering of iron oxide nanoparticles for biomedical applications. *Biomaterials* [Internet]. 2005;26(18):3995–4021. Available from: <https://www.sciencedirect.com/science/article/pii/S0142961204009317>
34. Woo K, Lee HJ, Ahn J-P, Park YS. Sol–Gel Mediated Synthesis of Fe<sub>2</sub>O<sub>3</sub> Nanorods. *Adv Mater* [Internet]. 2003 Oct 16;15(20):1761–4. Available from: <https://doi.org/10.1002/adma.200305561>
35. Wang X, Zhuang J, Peng Q, Li Y. A general strategy for nanocrystal synthesis. *Nature* [Internet]. 2005;437(7055):121–4. Available from: <https://doi.org/10.1038/nature03968>
36. Deng H, Li X, Peng Q, Wang X, Chen J, Li Y. Monodisperse Magnetic Single-Crystal Ferrite Microspheres. *Angew Chemie Int Ed* [Internet]. 2005 Apr 29;44(18):2782–5. Available

- from: <https://doi.org/10.1002/anie.200462551>
37. Murray CB, Norris DJ, Bawendi MG. Synthesis and characterization of nearly monodisperse CdE (E = sulfur, selenium, tellurium) semiconductor nanocrystallites. *J Am Chem Soc* [Internet]. 1993 Sep 1;115(19):8706–15. Available from: <https://doi.org/10.1021/ja00072a025>
  38. O'Brien P, Pickett N. Strategies for the Scalable Synthesis of Quantum Dots and Related Nanodimensional Materials. In: Butler J, Rao CNR, Müller A, Cheetham AK, Butler J, editors. *The Chemistry of Nanomaterials Synthesis, Properties and Applications*. Wiley-VCH Verlag GmbH & Co. KGaA; 2004.
  39. Carlos L, Garcia Einschlag FS, C. M, O. D. Applications of Magnetite Nanoparticles for Heavy Metal Removal from Wastewater. *Waste Water - Treat Technol Recent Anal Dev*. 2013;
  40. Heng T, Ze W, Wen-sheng T, Xiao-ping L, Jian-guo Q, Xiao-Hong Y. Synthesis of magnetic Fe<sub>3</sub>O<sub>4</sub> micro/nanospheres in organic solvent. *J Appl Biomater Funct Mater*. 2018;16(1\_suppl):26–31.
  41. Wang L, Bao J, Wang L, Zhang F, Li Y. One-pot synthesis and bioapplication of amine-functionalized magnetite nanoparticles and hollow nanospheres. *Chem - A Eur J*. 2006;12(24):6341–7.
  42. Almomani F, Bhosale R, Khraisheh M, kumar A, Almomani T. Heavy metal ions removal from industrial wastewater using magnetic nanoparticles (MNP). *Appl Surf Sci* [Internet]. 2020;506:144924. Available from: <https://doi.org/10.1016/j.apsusc.2019.144924>
  43. Zhang W, Shen F, Hong R. Solvothermal synthesis of magnetic Fe<sub>3</sub>O<sub>4</sub> microparticles via self-assembly of Fe<sub>3</sub>O<sub>4</sub> nanoparticles. *Particuology* [Internet]. 2011;9(2):179–86. Available from: <http://dx.doi.org/10.1016/j.partic.2010.07.025>
  44. Fuentes-García JA, Carvalho Alavarse A, Moreno Maldonado AC, Toro-Córdova A, Ibarra MR, Goya GF. Simple Sonochemical Method to Optimize the Heating Efficiency of Magnetic Nanoparticles for Magnetic Fluid Hyperthermia. *ACS Omega* [Internet]. 2020 Oct 20;5(41):26357–64. Available from: <https://doi.org/10.1021/acsomega.0c02212>
  45. Abu Mukh-Qasem R, Gedanken A. Sonochemical synthesis of stable hydrosol of Fe<sub>3</sub>O<sub>4</sub> nanoparticles. *J Colloid Interface Sci* [Internet]. 2005;284(2):489–94. Available from: <https://www.sciencedirect.com/science/article/pii/S0021979704011142>
  46. Saunders RW, Plane JMC. The formation and growth of Fe<sub>2</sub>O<sub>3</sub> nanoparticles from the photo-oxidation of iron pentacarbonyl. *J Aerosol Sci* [Internet]. 2010;41(5):475–89. Available from: <https://www.sciencedirect.com/science/article/pii/S002185021000042X>
  47. Li Y, Hu Y, Huang G, Li C. Metallic iron nanoparticles: Flame synthesis, characterization and magnetic properties. *Particuology* [Internet]. 2013;11(4):460–7. Available from: <https://www.sciencedirect.com/science/article/pii/S1674200113000825>

48. Gautam M, Kim JO, Yong CS. Fabrication of aerosol-based nanoparticles and their applications in biomedical fields. *J Pharm Investig* [Internet]. 2021;51(4):361–75. Available from: <https://doi.org/10.1007/s40005-021-00523-1>
49. Fajaroh F, Setyawan H, Widiyastuti W, Winardi S. Synthesis of magnetite nanoparticles by surfactant-free electrochemical method in an aqueous system. *Adv Powder Technol* [Internet]. 2012;23(3):328–33. Available from: <https://www.sciencedirect.com/science/article/pii/S092188311100063X>
50. Marques RFC, Garcia C, Lecante P, Ribeiro SJL, Noé L, Silva NJO, et al. Electro-precipitation of Fe<sub>3</sub>O<sub>4</sub> nanoparticles in ethanol. *J Magn Magn Mater* [Internet]. 2008;320(19):2311–5. Available from: <https://www.sciencedirect.com/science/article/pii/S0304885308005635>
51. Cabrera L, Gutierrez S, Menendez N, Morales MP, Herrasti P. Magnetite nanoparticles: Electrochemical synthesis and characterization. *Electrochim Acta* [Internet]. 2008;53(8):3436–41. Available from: <https://www.sciencedirect.com/science/article/pii/S0013468607014521>
52. Gittins DI, Caruso F. Spontaneous Phase Transfer of Nanoparticulate Metals from Organic to Aqueous Media. *Angew Chemie Int Ed* [Internet]. 2001 Aug 17;40(16):3001–4. Available from: [https://doi.org/10.1002/1521-3773\(20010817\)40:16%3C3001::AID-ANIE3001%3E3.0.CO](https://doi.org/10.1002/1521-3773(20010817)40:16%3C3001::AID-ANIE3001%3E3.0.CO)
53. V. KM, Marcus S, V. TD. Colloidal Nanocrystals with Molecular Metal Chalcogenide Surface Ligands. *Science* (80- ) [Internet]. 2009 Jun 12;324(5933):1417–20. Available from: <https://doi.org/10.1126/science.1170524>
54. Liu Y, Purich DL, Wu C, Wu Y, Chen T, Cui C, et al. Ionic Functionalization of Hydrophobic Colloidal Nanoparticles To Form Ionic Nanoparticles with Enzymelike Properties. *J Am Chem Soc* [Internet]. 2015 Dec 2;137(47):14952–8. Available from: <https://doi.org/10.1021/jacs.5b08533>
55. Zhang T, Ge J, Hu Y, Yin Y. A General Approach for Transferring Hydrophobic Nanocrystals into Water. *Nano Lett* [Internet]. 2007 Oct 1;7(10):3203–7. Available from: <https://doi.org/10.1021/nl071928t>
56. Swami A, Kumar A, Sastry M. Formation of Water-Dispersible Gold Nanoparticles Using a Technique Based on Surface-Bound Interdigitated Bilayers. *Langmuir* [Internet]. 2003 Feb 18;19(4):1168–72. Available from: <https://doi.org/10.1021/la026523x>
57. Yu WW, Chang E, Falkner JC, Zhang J, Al-Somali AM, Sayes CM, et al. Forming Biocompatible and Nonaggregated Nanocrystals in Water Using Amphiphilic Polymers. *J Am Chem Soc* [Internet]. 2007 Mar 1;129(10):2871–9. Available from: <https://doi.org/10.1021/ja067184n>
58. Chan Y, Zimmer JP, Strohm M, Steckel JS, Jain RK, Bawendi MG. Incorporation of Luminescent Nanocrystals into Monodisperse Core–Shell Silica Microspheres. *Adv Mater* [Internet].

- 2004 Dec 17;16(23–24):2092–7. Available from: <https://doi.org/10.1002/adma.200400237>
59. Wu L, Yu J, Chen L, Yang D, Zhang S, Han L, et al. A general and facile approach to disperse hydrophobic nanocrystals in water with enhanced long-term stability. *J Mater Chem C*. 2017;5(12):3065–71.
  60. Liu JF, Zhao ZS, Jiang G Bin. Coating Fe<sub>3</sub>O<sub>4</sub> magnetic nanoparticles with humic acid for high efficient removal of heavy metals in water. *Environ Sci Technol*. 2008;42(18):6949–54.
  61. El-Dib FI, Mohamed DE, El-Shamy OAA, Mishrif MR. Study the adsorption properties of magnetite nanoparticles in the presence of different synthesized surfactants for heavy metal ions removal. *Egypt J Pet*. 2020;29(1):1–7.
  62. Mahdavian AR, Mirrahimi MAS. Efficient separation of heavy metal cations by anchoring polyacrylic acid on superparamagnetic magnetite nanoparticles through surface modification. *Chem Eng J [Internet]*. 2010;159(1–3):264–71. Available from: <http://dx.doi.org/10.1016/j.cej.2010.02.041>
  63. Ge F, Li MM, Ye H, Zhao BX. Effective removal of heavy metal ions Cd<sup>2+</sup>, Zn<sup>2+</sup>, Pb<sup>2+</sup>, Cu<sup>2+</sup> from aqueous solution by polymer-modified magnetic nanoparticles. *J Hazard Mater [Internet]*. 2012;211–212:366–72. Available from: <http://dx.doi.org/10.1016/j.jhazmat.2011.12.013>
  64. Wang J, Zheng S, Shao Y, Liu J, Xu Z, Zhu D. Amino-functionalized Fe<sub>3</sub>O<sub>4</sub>@SiO<sub>2</sub> core-shell magnetic nanomaterial as a novel adsorbent for aqueous heavy metals removal. *J Colloid Interface Sci [Internet]*. 2010;349(1):293–9. Available from: <http://dx.doi.org/10.1016/j.jcis.2010.05.010>
  65. Shishehbore MR, Afkhami A, Bagheri H. Salicylic acid functionalized silica-coated magnetite nanoparticles for solid phase extraction and preconcentration of some heavy metal ions from various real samples. *Chem Cent J*. 2011;5(1):17–20.
  66. Lu A-H, Li W-C, Matoussevitch N, Spliethoff B, Bönnemann H, Schüth F. Highly stable carbon-protected cobalt nanoparticles and graphite shells. *Chem Commun [Internet]*. 2005;(1):98–100. Available from: <http://dx.doi.org/10.1039/B414146F>
  67. Liu Q, Xu Z, Finch JA, Egerton R. A Novel Two-Step Silica-Coating Process for Engineering Magnetic Nanocomposites. *Chem Mater [Internet]*. 1998 Dec 1;10(12):3936–40. Available from: <https://doi.org/10.1021/cm980370a>
  68. Lin J, Zhou W, Kumbhar A, Wiemann J, Fang J, Carpenter EE, et al. Gold-Coated Iron (Fe@Au) Nanoparticles: Synthesis, Characterization, and Magnetic Field-Induced Self-Assembly. *J Solid State Chem [Internet]*. 2001;159(1):26–31. Available from: <https://www.sciencedirect.com/science/article/pii/S0022459601991170>
  69. Tartaj P, Serna CJ. Synthesis of Monodisperse Superparamagnetic Fe/Silica Nanospherical

- Composites. *J Am Chem Soc* [Internet]. 2003 Dec 1;125(51):15754–5. Available from: <https://doi.org/10.1021/ja0380594>
70. Yantasee W, Warner CL, Sangvanich T, Addleman RS, Carter TG, Wiacek RJ, et al. Removal of Heavy Metals from Aqueous Systems with Thiol Functionalized Superparamagnetic Nanoparticles. *Environ Sci Technol* [Internet]. 2007 Jul 1;41(14):5114–9. Available from: <https://doi.org/10.1021/es0705238>
71. Masjedi A, Askarizadeh E, Baniyaghoob S. Magnetic nanoparticles surface-modified with tridentate ligands for removal of heavy metal ions from water. *Mater Chem Phys* [Internet]. 2020;249:122917. Available from: <https://www.sciencedirect.com/science/article/pii/S0254058420302959>
72. Mahdavi M, Ahmad M Bin, Haron MJ, Gharayebi Y, Shameli K, Nadi B. Fabrication and Characterization of SiO<sub>2</sub>/(3-Aminopropyl)triethoxysilane-Coated Magnetite Nanoparticles for Lead(II) Removal from Aqueous Solution. *J Inorg Organomet Polym Mater* [Internet]. 2013;23(3):599–607. Available from: <https://doi.org/10.1007/s10904-013-9820-2>
73. Abdollahi M, Zeinali S, Nasirimoghaddam S, Sabbaghi S. Effective removal of As (III) from drinking water samples by chitosan-coated magnetic nanoparticles. *Desalin Water Treat*. 2015;56(8):2092–104.
74. Trewyn BG, Slowing II, Giri S, Chen H-T, Lin VS-Y. Synthesis and Functionalization of a Mesoporous Silica Nanoparticle Based on the Sol–Gel Process and Applications in Controlled Release. *Acc Chem Res* [Internet]. 2007 Sep 1;40(9):846–53. Available from: <https://doi.org/10.1021/ar600032u>
75. Narayan R, Nayak UY, Raichur AM, Garg S. Mesoporous silica nanoparticles: A comprehensive review on synthesis and recent advances. *Pharmaceutics*. 2018;10(3):1–49.
76. He Q, Shi J, Chen F, Zhu M, Zhang L. An anticancer drug delivery system based on surfactant-templated mesoporous silica nanoparticles. *Biomaterials* [Internet]. 2010;31(12):3335–46. Available from: <http://dx.doi.org/10.1016/j.biomaterials.2010.01.015>
77. Soto RJ, Yang L, Schoenfish MH. Functionalized Mesoporous Silica via an Aminosilane Surfactant Ion Exchange Reaction: Controlled Scaffold Design and Nitric Oxide Release. *ACS Appl Mater Interfaces*. 2016;8(3):2220–31.
78. Ghaedi H, Zhao M. Review on Template Removal Techniques for Synthesis of Mesoporous Silica Materials. *Energy & Fuels* [Internet]. 2022 Mar 3;36(5):2424–46. Available from: <https://doi.org/10.1021/acs.energyfuels.1c04435>
79. Lang N, Tuel A. A Fast and Efficient Ion-Exchange Procedure To Remove Surfactant Molecules from MCM-41 Materials. *Chem Mater* [Internet]. 2004 May 1;16(10):1961–6. Available from: <https://doi.org/10.1021/cm030633n>

80. Buchman JT, Elmer WH, Ma C, Landy KM, White JC, Haynes CL. Chitosan-Coated Mesoporous Silica Nanoparticle Treatment of *Citrullus lanatus* (Watermelon): Enhanced Fungal Disease Suppression and Modulated Expression of Stress-Related Genes. 2019;
81. Bhattarai N, Gunn J, Zhang M. Chitosan-based hydrogels for controlled, localized drug delivery. *Adv Drug Deliv Rev* [Internet]. 2010;62(1):83–99. Available from: <https://www.sciencedirect.com/science/article/pii/S0169409X09002828>
82. Hu X, Wang Y, Peng B. Chitosan-Capped Mesoporous Silica Nanoparticles as pH-Responsive Nanocarriers for Controlled Drug Release. 2013;1–10.
83. Gulfam M, Chung BG. Development of pH-Responsive Chitosan-Coated Mesoporous Silica Nanoparticles. 2014;
84. Shah P V, Rajput SJ. Facile Synthesis of Chitosan Capped Mesoporous Silica Nanoparticles : A pH Responsive Smart Delivery Platform for Raloxifene Hydrochloride. 2018;
85. Santoso AV, Susanto A, Irawaty W, Hartono SB. Chitosan modified mesoporous silica nanoparticles as a versatile drug carrier with pH dependent properties Chitosan Modified Mesoporous Silica Nanoparticles as A Versatile Drug Carrier with pH Dependent Properties. 2020;020011(June 2019).
86. Yan T, He J, Liu R, Liu Z, Cheng J. Chitosan capped pH-responsive hollow mesoporous silica nanoparticles for targeted chemo-photo combination therapy. *Carbohydr Polym* [Internet]. 2020;231:115706. Available from: <https://www.sciencedirect.com/science/article/pii/S0144861719313748>
87. Shakeran Z, Keyhanfar M, Varshosaz J, Sutherland DS. Biodegradable nanocarriers based on chitosan-modified mesoporous silica nanoparticles for delivery of methotrexate for application in breast cancer treatment. *Mater Sci Eng C* [Internet]. 2021;118:111526. Available from: <https://www.sciencedirect.com/science/article/pii/S0928493120334445>
88. Xu C, Cao L, Zhao P, Zhou Z, Cao C, Li F, et al. Emulsion-based synchronous pesticide encapsulation and surface modification of mesoporous silica nanoparticles with carboxymethyl chitosan for controlled azoxystrobin release. *Chem Eng J* [Internet]. 2018;348:244–54. Available from: <https://www.sciencedirect.com/science/article/pii/S1385894718307976>
89. Narayan R, Gadag S, Cheruku SP, Raichur AM, Day CM, Garg S, et al. Chitosan-glucuronic acid conjugate coated mesoporous silica nanoparticles: A smart pH-responsive and receptor-targeted system for colorectal cancer therapy. *Carbohydr Polym* [Internet]. 2021;261:117893. Available from: <https://www.sciencedirect.com/science/article/pii/S0144861721002800>
90. Nhavene EPF, da Silva WM, Trivelato Junior RR, Gastelois PL, Venâncio T, Nascimento R, et al. Chitosan grafted into mesoporous silica nanoparticles as benzimidazol carrier for Chagas diseases treatment. *Microporous Mesoporous Mater* [Internet]. 2018;272:265–75.

- Available from: <https://www.sciencedirect.com/science/article/pii/S1387181118303457>
91. Abukhadra MR, Refay NM, Nadeem A, El-Sherbeeney AM, Ibrahim KE. Insight into the role of integrated carbohydrate polymers (starch, chitosan, and  $\beta$ -cyclodextrin) with mesoporous silica as carriers for ibuprofen drug; equilibrium and pharmacokinetic properties. *Int J Biol Macromol* [Internet]. 2020;156:537–47. Available from: <https://www.sciencedirect.com/science/article/pii/S0141813020329093>
  92. Keshavarz H, Khavandi A, Alamolhoda S, Naimi-jamal MR. pH-Sensitive magnetite mesoporous silica nanocomposites for controlled drug delivery and hyperthermia. 2020;39008–16.
  93. Ramasamy DL, Puhakka V, Iftekhar S, Wojtuś A, Repo E, Ben Hammouda S, et al. N- and O-ligand doped mesoporous silica-chitosan hybrid beads for the efficient, sustainable and selective recovery of rare earth elements (REE) from acid mine drainage (AMD): Understanding the significance of physical modification and conditioning of th. *J Hazard Mater* [Internet]. 2018;348:84–91. Available from: <https://www.sciencedirect.com/science/article/pii/S030438941830030X>
  94. Abukhadra MR, Eid MH, El-Meligy MA, Sharaf M, Soliman AT. Insight into chitosan/mesoporous silica nanocomposites as eco-friendly adsorbent for enhanced retention of U (VI) and Sr (II) from aqueous solutions and real water. *Int J Biol Macromol* [Internet]. 2021;173:435–44. Available from: <https://www.sciencedirect.com/science/article/pii/S0141813021001690>
  95. Mahmoodi NM, Mokhtari-Shourijeh Z, Abdi J. Preparation of mesoporous polyvinyl alcohol/chitosan/silica composite nanofiber and dye removal from wastewater. *Environ Prog Sustain Energy* [Internet]. 2019 Mar 1;38(s1):S100–9. Available from: <https://doi.org/10.1002/ep.12933>
  96. Zarei F, Marjani A, Soltani R. Novel and green nanocomposite-based adsorbents from functionalised mesoporous KCC-1 and chitosan-oleic acid for adsorption of Pb(II). *Eur Polym J* [Internet]. 2019;119:400–9. Available from: <https://www.sciencedirect.com/science/article/pii/S0014305719312339>
  97. Shan W, Zhang D, Wang X, Wang D, Xing Z, Xiong Y, et al. One-pot synthesis of mesoporous chitosan-silica composite from sodium silicate for application in Rhenium(VII) adsorption. *Microporous Mesoporous Mater* [Internet]. 2019;278:44–53. Available from: <https://www.sciencedirect.com/science/article/pii/S1387181118305638>
  98. Kwok KCM, Koong LF, Chen G, McKay G. Mechanism of arsenic removal using chitosan and nanochitosan. *J Colloid Interface Sci* [Internet]. 2014;416:1–10. Available from: <https://www.sciencedirect.com/science/article/pii/S0021979713009314>
  99. Gupta A, Yunus M, Sankararamakrishnan N. Zerovalent iron encapsulated chitosan nanospheres – A novel adsorbent for the removal of total inorganic Arsenic from aqueous systems. *Chemosphere* [Internet]. 2012;86(2):150–5. Available from:

- <https://www.sciencedirect.com/science/article/pii/S0045653511011441>
100. Miller SM, Zimmerman JB. Novel, bio-based, photoactive arsenic sorbent: TiO<sub>2</sub>-impregnated chitosan bead. *Water Res* [Internet]. 2010;44(19):5722–9. Available from: <https://www.sciencedirect.com/science/article/pii/S0043135410003623>
  101. Yamani JS, Miller SM, Spaulding ML, Zimmerman JB. Enhanced arsenic removal using mixed metal oxide impregnated chitosan beads. *Water Res* [Internet]. 2012;46(14):4427–34. Available from: <https://www.sciencedirect.com/science/article/pii/S0043135412004009>
  102. Liu C, Wang B, Deng Y, Cui B, Wang J, Chen W, et al. Performance of a new magnetic chitosan nanoparticle to remove arsenic and its separation from water. *J Nanomater*. 2015;2015(lii).
  103. Wang J, Xu W, Chen L, Huang X, Liu J. Preparation and evaluation of magnetic nanoparticles impregnated chitosan beads for arsenic removal from water. *Chem Eng J* [Internet]. 2014;251:25–34. Available from: <http://dx.doi.org/10.1016/j.cej.2014.04.061>
  104. Ma J, Shen Y, Shen C, Wen Y, Liu W. Al-doping chitosan–Fe(III) hydrogel for the removal of fluoride from aqueous solutions. *Chem Eng J* [Internet]. 2014;248:98–106. Available from: <https://www.sciencedirect.com/science/article/pii/S1385894714002605>
  105. Shinde RN, Pandey AK, Acharya R, Guin R, Das SK, Rajurkar NS, et al. Chitosan-transition metal ions complexes for selective arsenic(V) preconcentration. *Water Res* [Internet]. 2013;47(10):3497–506. Available from: <https://www.sciencedirect.com/science/article/pii/S0043135413003084>
  106. Brião G de V, de Andrade JR, da Silva MGC, Vieira MGA. Removal of toxic metals from water using chitosan-based magnetic adsorbents. A review. *Environ Chem Lett* [Internet]. 2020;18(4):1145–68. Available from: <https://doi.org/10.1007/s10311-020-01003-y>
  107. Järup L. Hazards of heavy metal contamination. *Br Med Bull* [Internet]. 2003 Dec 1;68(1):167–82. Available from: <https://doi.org/10.1093/bmb/ldg032>
  108. Engwa GA. Mechanism and Health Effects of Heavy Metal Toxicity in Humans. In: Ferdinand PU, editor. Rijeka: IntechOpen; 2019. p. Ch. 5. Available from: <https://doi.org/10.5772/intechopen.82511>
  109. Wu X, Cobbina SJ, Mao G, Xu H, Zhang Z, Yang L. A review of toxicity and mechanisms of individual and mixtures of heavy metals in the environment. *Environ Sci Pollut Res* [Internet]. 2016;23(9):8244–59. Available from: <https://doi.org/10.1007/s11356-016-6333-x>
  110. Nordberg GF, Fowler BA, Nordberg M, Friberg LT. CHAPTER 1 - Introduction—General Considerations and International Perspectives. In: Nordberg GF, Fowler BA, Nordberg M, Friberg LTBT-H on the T of M (Third E, editors. *Handbook on the Toxicology of Metals* (Third



- Edition) [Internet]. Burlington: Academic Press; 2007. p. 1–9. Available from: <https://www.sciencedirect.com/science/article/pii/B9780123694133500562>
111. Fu F, Wang Q. Removal of heavy metal ions from wastewaters: A review. *J Environ Manage* [Internet]. 2011;92(3):407–18. Available from: <https://www.sciencedirect.com/science/article/pii/S0301479710004147>
  112. Renu, Agarwal M, Singh K. Heavy metal removal from wastewater using various adsorbents: a review. *J Water Reuse Desalin* [Internet]. 2016 Nov 3;7(4):387–419. Available from: <https://doi.org/10.2166/wrd.2016.104>
  113. Mamtani R, Stern P, Dawood I, Cheema S. Metals and Disease: A Global Primary Health Care Perspective. Büsselberg D, editor. *J Toxicol* [Internet]. 2011;2011:319136. Available from: <https://doi.org/10.1155/2011/319136>
  114. Egorova KS, Ananikov VP. Toxicity of Metal Compounds: Knowledge and Myths. *Organometallics* [Internet]. 2017 Nov 13;36(21):4071–90. Available from: <https://doi.org/10.1021/acs.organomet.7b00605>
  115. Hargreaves AJ, Constantino C, Dotro G, Cartmell E, Campo P. Fate and removal of metals in municipal wastewater treatment: a review. *Environ Technol Rev* [Internet]. 2018 Jan 1;7(1):1–18. Available from: <https://doi.org/10.1080/21622515.2017.1423398>
  116. Baltpurvins KA, Burns RC, Lawrance GA, Stuart AD. Effect of electrolyte composition on zinc hydroxide precipitation by lime. *Water Res* [Internet]. 1997;31(5):973–80. Available from: <https://www.sciencedirect.com/science/article/pii/S0043135496003272>
  117. Matlock MM, Howerton BS, Atwood DA. Chemical precipitation of heavy metals from acid mine drainage. *Water Res* [Internet]. 2002;36(19):4757–64. Available from: <https://www.sciencedirect.com/science/article/pii/S0043135402001495>
  118. Fu F, Zeng H, Cai Q, Qiu R, Yu J, Xiong Y. Effective removal of coordinated copper from wastewater using a new dithiocarbamate-type supramolecular heavy metal precipitant. *Chemosphere* [Internet]. 2007;69(11):1783–9. Available from: <https://www.sciencedirect.com/science/article/pii/S0045653507006911>
  119. Chang Q, Zhang M, Wang J. Removal of Cu<sup>2+</sup> and turbidity from wastewater by mercaptoacetyl chitosan. *J Hazard Mater* [Internet]. 2009;169(1):621–5. Available from: <https://www.sciencedirect.com/science/article/pii/S030438940900541X>
  120. Alyüz B, Veli S. Kinetics and equilibrium studies for the removal of nickel and zinc from aqueous solutions by ion exchange resins. *J Hazard Mater* [Internet]. 2009;167(1):482–8. Available from: <https://www.sciencedirect.com/science/article/pii/S0304389409000296>
  121. Gode F, Pehlivan E. Removal of chromium(III) from aqueous solutions using Lewatit S 100: The effect of pH, time, metal concentration and temperature. *J Hazard Mater* [Internet]. 2006;136(2):330–7. Available from:

- <https://www.sciencedirect.com/science/article/pii/S0304389405008319>
122. Motsi T, Rowson NA, Simmons MJH. Adsorption of heavy metals from acid mine drainage by natural zeolite. *Int J Miner Process* [Internet]. 2009;92(1):42–8. Available from: <https://www.sciencedirect.com/science/article/pii/S0301751609000349>
  123. Doula MK. Simultaneous removal of Cu, Mn and Zn from drinking water with the use of clinoptilolite and its Fe-modified form. *Water Res* [Internet]. 2009;43(15):3659–72. Available from: <https://www.sciencedirect.com/science/article/pii/S0043135409003522>
  124. Sadrzadeh M, Mohammadi T, Ivakpour J, Kasiri N. Neural network modeling of Pb<sup>2+</sup> removal from wastewater using electrodialysis. *Chem Eng Process Process Intensif* [Internet]. 2009;48(8):1371–81. Available from: <https://www.sciencedirect.com/science/article/pii/S0255270109001032>
  125. Lundh M, Jönsson L, Dahlquist J. Experimental studies of the fluid dynamics in the separation zone in dissolved air flotation. *Water Res* [Internet]. 2000;34(1):21–30. Available from: <https://www.sciencedirect.com/science/article/pii/S0043135499001360>
  126. Polat H, Erdogan D. Heavy metal removal from waste waters by ion flotation. *J Hazard Mater* [Internet]. 2007;148(1):267–73. Available from: <https://www.sciencedirect.com/science/article/pii/S0304389407002634>
  127. Capponi F, Sartori M, Souza ML, Rubio J. Modified column flotation of adsorbing iron hydroxide colloidal precipitates. *Int J Miner Process* [Internet]. 2006;79(3):167–73. Available from: <https://www.sciencedirect.com/science/article/pii/S0301751606000408>
  128. Chen G. Electrochemical technologies in wastewater treatment. *Sep Purif Technol* [Internet]. 2004;38(1):11–41. Available from: <https://www.sciencedirect.com/science/article/pii/S1383586603002636>
  129. Issabayeva G, Aroua MK, Sulaiman NM. Electrodeposition of copper and lead on palm shell activated carbon in a flow-through electrolytic cell. *Desalination* [Internet]. 2006;194(1):192–201. Available from: <https://www.sciencedirect.com/science/article/pii/S0011916406003730>
  130. Worch E. Adsorption Technology in Water Treatment: Fundamentals, Processes, and Modeling [Internet]. De Gruyter; 2012. Available from: <https://doi.org/10.1515/9783110240238>
  131. Kang KC, Kim SS, Choi JW, Kwon SH. Sorption of Cu<sup>2+</sup> and Cd<sup>2+</sup> onto acid- and base-pretreated granular activated carbon and activated carbon fiber samples. *J Ind Eng Chem* [Internet]. 2008;14(1):131–5. Available from: <https://www.sciencedirect.com/science/article/pii/S1226086X07000214>
  132. Kabbashi NA, Atieh MA, Al-Mamun A, Mirghami MES, Alam MDZ, Yahya N. Kinetic adsorption of application of carbon nanotubes for Pb(II) removal from aqueous solution. *J*

- Environ Sci [Internet]. 2009;21(4):539–44. Available from: <https://www.sciencedirect.com/science/article/pii/S1001074208623050>
133. Apiratikul R, Pavasant P. Batch and column studies of biosorption of heavy metals by *Caulerpa lentillifera*. *Bioresour Technol* [Internet]. 2008;99(8):2766–77. Available from: <https://www.sciencedirect.com/science/article/pii/S0960852407005354>
  134. Otunola BO, Ololade OO. A review on the application of clay minerals as heavy metal adsorbents for remediation purposes. *Environ Technol Innov* [Internet]. 2020;100692. Available from: <https://doi.org/10.1016/j.eti.2020.100692>
  135. Aboudi Mana SC, Hanafiah MM, Chowdhury AJK. Environmental characteristics of clay and clay-based minerals. *Geol Ecol Landscapes* [Internet]. 2017;1(3):155–61. Available from: <http://doi.org/10.1080/24749508.2017.1361128>
  136. Borden D, Giese RF. BASELINE STUDIES OF THE CLAY MINERALS SOCIETY SOURCE CLAYS: CATION EXCHANGE CAPACITY MEASUREMENTS BY THE AMMONIA-ELECTRODE METHOD. *Clays Clay Miner*. 2001;49(5):444–5.
  137. Dogan AU, Dogan M, Onal M, Sarikaya Y, Aburub A, Wurster DE. Baseline studies of the clay minerals society source clays: Specific surface area by the Brunauer Emmett Teller (BET) method. *Clays Clay Miner* [Internet]. 2006;54(1):62–6. Available from: <https://doi.org/10.1346/CCMN.2006.0540108>
  138. O’Connell DW, Birkinshaw C, O’Dwyer TF. Heavy metal adsorbents prepared from the modification of cellulose: A review. *Bioresour Technol* [Internet]. 2008;99(15):6709–24. Available from: <https://www.sciencedirect.com/science/article/pii/S0960852408000710>
  139. Maekawa E, Koshijima T. Properties of 2,3-dicarboxy cellulose combined with various metallic ions. *J Appl Polym Sci* [Internet]. 1984 Jul 1;29(7):2289–97. Available from: <https://doi.org/10.1002/app.1984.070290705>
  140. Gopalakrishnan A, Krishnan R, Thangavel S, Venugopal G, Kim S-J. Removal of heavy metal ions from pharma-effluents using graphene-oxide nanosorbents and study of their adsorption kinetics. *J Ind Eng Chem* [Internet]. 2015;30:14–9. Available from: <https://www.sciencedirect.com/science/article/pii/S1226086X15002804>
  141. Li L, Fan L, Sun M, Qiu H, Li X, Duan H, et al. Adsorbent for chromium removal based on graphene oxide functionalized with magnetic cyclodextrin–chitosan. *Colloids Surfaces B Biointerfaces* [Internet]. 2013;107:76–83. Available from: <https://www.sciencedirect.com/science/article/pii/S0927776513000982>
  142. Guo X, Du B, Wei Q, Yang J, Hu L, Yan L, et al. Synthesis of amino functionalized magnetic graphenes composite material and its application to remove Cr(VI), Pb(II), Hg(II), Cd(II) and Ni(II) from contaminated water. *J Hazard Mater* [Internet]. 2014;278:211–20. Available from: <https://www.sciencedirect.com/science/article/pii/S0304389414004208>

143. Gupta VK, Agarwal S, Saleh TA. Chromium removal by combining the magnetic properties of iron oxide with adsorption properties of carbon nanotubes. *Water Res* [Internet]. 2011;45(6):2207–12. Available from: <https://www.sciencedirect.com/science/article/pii/S0043135411000273>
144. Luo C, Tian Z, Yang B, Zhang L, Yan S. Manganese dioxide/iron oxide/acid oxidized multi-walled carbon nanotube magnetic nanocomposite for enhanced hexavalent chromium removal. *Chem Eng J* [Internet]. 2013;234:256–65. Available from: <https://www.sciencedirect.com/science/article/pii/S1385894713011376>
145. Mubarak NM, Thines RK, Sajuni NR, Abdullah EC, Sahu JN, Ganesan P, et al. Adsorption of chromium (VI) on functionalized and non-functionalized carbon nanotubes. *Korean J Chem Eng* [Internet]. 2014;31(9):1582–91. Available from: <https://doi.org/10.1007/s11814-014-0101-8>
146. Javadian H, Sorkhrodi FZ, Koutenaie BB. Experimental investigation on enhancing aqueous cadmium removal via nanostructure composite of modified hexagonal type mesoporous silica with polyaniline/polypyrrole nanoparticles. *J Ind Eng Chem* [Internet]. 2014;20(5):3678–88. Available from: <https://www.sciencedirect.com/science/article/pii/S1226086X13006989>
147. Burke AM, Hanrahan JP, Healy DA, Sodeau JR, Holmes JD, Morris MA. Large pore bi-functionalised mesoporous silica for metal ion pollution treatment. *J Hazard Mater* [Internet]. 2009;164(1):229–34. Available from: <https://www.sciencedirect.com/science/article/pii/S030438940801193X>
148. Chen A, Zeng G, Chen G, Hu X, Yan M, Guan S, et al. Novel thiourea-modified magnetic ion-imprinted chitosan/TiO<sub>2</sub> composite for simultaneous removal of cadmium and 2,4-dichlorophenol. *Chem Eng J* [Internet]. 2012;191:85–94. Available from: <https://www.sciencedirect.com/science/article/pii/S138589471200304X>
149. Hydari S, Sharififard H, Nabavinia M, Parvizi M reza. A comparative investigation on removal performances of commercial activated carbon, chitosan biosorbent and chitosan/activated carbon composite for cadmium. *Chem Eng J* [Internet]. 2012;193–194:276–82. Available from: <https://www.sciencedirect.com/science/article/pii/S1385894712005190>
150. Zhu C, Luan Z, Wang Y, Shan X. Removal of cadmium from aqueous solutions by adsorption on granular red mud (GRM). *Sep Purif Technol* [Internet]. 2007;57(1):161–9. Available from: <https://www.sciencedirect.com/science/article/pii/S1383586607001463>
151. Gupta VK, Sharma S. Removal of Cadmium and Zinc from Aqueous Solutions Using Red Mud. *Environ Sci Technol* [Internet]. 2002 Aug 1;36(16):3612–7. Available from: <https://doi.org/10.1021/es020010v>
152. Ma Y, Lin C, Jiang Y, Lu W, Si C, Liu Y. Competitive removal of water-borne copper, zinc and cadmium by a CaCO<sub>3</sub>-dominated red mud. *J Hazard Mater* [Internet]. 2009;172(2):1288–

96. Available from:  
<https://www.sciencedirect.com/science/article/pii/S0304389409012680>
153. Mahmoud ME, Osman MM, Hafez OF, Elmelegy E. Removal and preconcentration of lead (II), copper (II), chromium (III) and iron (III) from wastewaters by surface developed alumina adsorbents with immobilized 1-nitroso-2-naphthol. *J Hazard Mater* [Internet]. 2010;173(1):349–57. Available from:  
<https://www.sciencedirect.com/science/article/pii/S0304389409013867>
154. Fouladgar M, Beheshti M, Sabzyan H. Single and binary adsorption of nickel and copper from aqueous solutions by  $\gamma$ -alumina nanoparticles: Equilibrium and kinetic modeling. *J Mol Liq* [Internet]. 2015;211:1060–73. Available from:  
<https://www.sciencedirect.com/science/article/pii/S0167732215303299>
155. Ghaemi N. A new approach to copper ion removal from water by polymeric nanocomposite membrane embedded with  $\gamma$ -alumina nanoparticles. *Appl Surf Sci* [Internet]. 2016;364:221–8. Available from:  
<https://www.sciencedirect.com/science/article/pii/S0169433215031141>
156. Han R, Li H, Li Y, Zhang J, Xiao H, Shi J. Biosorption of copper and lead ions by waste beer yeast. *J Hazard Mater* [Internet]. 2006;137(3):1569–76. Available from:  
<https://www.sciencedirect.com/science/article/pii/S0304389406004195>
157. Uslu G, Tanyol M. Equilibrium and thermodynamic parameters of single and binary mixture biosorption of lead (II) and copper (II) ions onto *Pseudomonas putida*: Effect of temperature. *J Hazard Mater* [Internet]. 2006;135(1):87–93. Available from:  
<https://www.sciencedirect.com/science/article/pii/S030438940500734X>
158. Lu W-B, Shi J-J, Wang C-H, Chang J-S. Biosorption of lead, copper and cadmium by an indigenous isolate *Enterobacter* sp. J1 possessing high heavy-metal resistance. *J Hazard Mater* [Internet]. 2006;134(1):80–6. Available from:  
<https://www.sciencedirect.com/science/article/pii/S0304389405006527>
159. Romera E, González F, Ballester A, Blázquez ML, Muñoz JA. Comparative study of biosorption of heavy metals using different types of algae. *Bioresour Technol* [Internet]. 2007;98(17):3344–53. Available from:  
<https://www.sciencedirect.com/science/article/pii/S096085240600486X>
160. Iqbal M, Edyvean RGJ. Biosorption of lead, copper and zinc ions on loofa sponge immobilized biomass of *Phanerochaete chrysosporium*. *Miner Eng* [Internet]. 2004;17(2):217–23. Available from:  
<https://www.sciencedirect.com/science/article/pii/S0892687503004102>
161. Gupta VK, Srivastava SK, Mohan D, Sharma S. Design parameters for fixed bed reactors of activated carbon developed from fertilizer waste for the removal of some heavy metal ions. *Waste Manag* [Internet]. 1998;17(8):517–22. Available from:  
<https://www.sciencedirect.com/science/article/pii/S0956053X97100629>

162. Ghanizadeh G, Asgari G. Adsorption kinetics and isotherm of methylene blue and its removal from aqueous solution using bone charcoal. *React Kinet Mech Catal* [Internet]. 2011;102(1):127–42. Available from: <https://doi.org/10.1007/s11144-010-0247-2>
163. Masel RI. *Principles of Adsorption and Reaction on Solid Surfaces*. JOHN WILEY & SONS, INC.; 1996.
164. Lima ÉC, Adebayo MA, Machado FM. Kinetic and Equilibrium Models of Adsorption BT - Carbon Nanomaterials as Adsorbents for Environmental and Biological Applications. In: Bergmann CP, Machado FM, editors. Cham: Springer International Publishing; 2015. p. 33–69. Available from: [https://doi.org/10.1007/978-3-319-18875-1\\_3](https://doi.org/10.1007/978-3-319-18875-1_3)
165. Vaghetti JCP, Lima EC, Royer B, da Cunha BM, Cardoso NF, Brasil JL, et al. Pecan nutshell as biosorbent to remove Cu(II), Mn(II) and Pb(II) from aqueous solutions. *J Hazard Mater* [Internet]. 2009;162(1):270–80. Available from: <https://www.sciencedirect.com/science/article/pii/S030438940800719X>
166. Vaghetti JCP, Lima EC, Royer B, Brasil JL, da Cunha BM, Simon NM, et al. Application of Brazilian-pine fruit coat as a biosorbent to removal of Cr(VI) from aqueous solution— Kinetics and equilibrium study. *Biochem Eng J* [Internet]. 2008;42(1):67–76. Available from: <https://www.sciencedirect.com/science/article/pii/S1369703X08001885>
167. Lopes ECN, dos Anjos FSC, Vieira EFS, Cestari AR. An alternative Avrami equation to evaluate kinetic parameters of the interaction of Hg(II) with thin chitosan membranes. *J Colloid Interface Sci* [Internet]. 2003;263(2):542–7. Available from: <https://www.sciencedirect.com/science/article/pii/S0021979703003266>
168. Langmuir I. THE ADSORPTION OF GASES ON PLANE SURFACES OF GLASS, MICA AND PLATINUM. *J Am Chem Soc* [Internet]. 1918 Sep 1;40(9):1361–403. Available from: <https://doi.org/10.1021/ja02242a004>
169. Lima ÉC, Adebayo MA, Machado FM. Kinetic and equilibrium models of adsorption. Vol. 0, Carbon Nanostructures. 2015. 33–69 p.
170. Rouquerol F, Rouquerol J, Sing K. CHAPTER 5 - Adsorption at the Liquid–Solid Interface: Thermodynamics and Methodology. In: Rouquerol F, Rouquerol J, Sing KBT-A by P and PS, editors. London: Academic Press; 1999. p. 117–63. Available from: <https://www.sciencedirect.com/science/article/pii/B9780125989206500063>
171. Sips R. On the Structure of a Catalyst Surface. *J Chem Phys* [Internet]. 1948 May 1;16(5):490–5. Available from: <https://doi.org/10.1063/1.1746922>
172. Liu Y, Xu H, Yang S-F, Tay J-H. A general model for biosorption of Cd<sup>2+</sup>, Cu<sup>2+</sup> and Zn<sup>2+</sup> by aerobic granules. *J Biotechnol* [Internet]. 2003;102(3):233–9. Available from: <https://www.sciencedirect.com/science/article/pii/S0168165603000300>
173. Redlich O, Peterson DL. A Useful Adsorption Isotherm. *J Phys Chem* [Internet]. 1959 Jun

- 1;63(6):1024. Available from: <https://doi.org/10.1021/j150576a611>
174. Foo KY, Hameed BH. Insights into the modeling of adsorption isotherm systems. *Chem Eng J* [Internet]. 2010;156(1):2–10. Available from: <https://www.sciencedirect.com/science/article/pii/S1385894709006147>
175. Liu Y, Liu Y-J. Biosorption isotherms, kinetics and thermodynamics. *Sep Purif Technol* [Internet]. 2008;61(3):229–42. Available from: <https://www.sciencedirect.com/science/article/pii/S1383586607004571>
176. Yasuda K, Kitamoto Y. Fabrication of Fe<sub>3</sub>O<sub>4</sub> nanorods designed for liquid-phase magnetic biosensing. *AIP Conf Proc* [Internet]. 2018 Jan 22;1929(1):20009. Available from: <https://aip.scitation.org/doi/abs/10.1063/1.5021922>
177. Prilepskii AY, Fakhardo AF, Drozdov AS, Vinogradov V V, Dudanov IP, Shtil AA, et al. Urokinase-Conjugated Magnetite Nanoparticles as a Promising Drug Delivery System for Targeted Thrombolysis: Synthesis and Preclinical Evaluation. *ACS Appl Mater Interfaces* [Internet]. 2018 Oct 31;10(43):36764–75. Available from: <https://doi.org/10.1021/acsami.8b14790>
178. Purnawira B, Purwaningsih H, Ervianto Y, Pratiwi VM, Susanti D, Rochiem R, et al. Synthesis and characterization of mesoporous silica nanoparticles (MSNp) MCM 41 from natural waste rice husk. *IOP Conf Ser Mater Sci Eng* [Internet]. 2019;541(1):12018. Available from: <http://dx.doi.org/10.1088/1757-899X/541/1/012018>
179. Pham XN, Nguyen TP, Pham TN, Tran TTN, Tran TVT. Synthesis and characterization of chitosan-coated magnetite nanoparticles and their application in curcumin drug delivery. *Adv Nat Sci Nanosci Nanotechnol* [Internet]. 2016;7(4):45010. Available from: <http://dx.doi.org/10.1088/2043-6262/7/4/045010>
180. Pratt DY, Wilson LD, Kozinski JA. Preparation and sorption studies of glutaraldehyde cross-linked chitosan copolymers. *J Colloid Interface Sci* [Internet]. 2013;395:205–11. Available from: <https://www.sciencedirect.com/science/article/pii/S0021979712014270>
181. An F, Gao B, Dai X, Wang M, Wang X. Efficient removal of heavy metal ions from aqueous solution using salicylic acid type chelate adsorbent. *J Hazard Mater* [Internet]. 2011;192(3):956–62. Available from: <https://www.sciencedirect.com/science/article/pii/S0304389411006893>
182. Alsaiari NS, Alzahrani FM, Katubi KM, Amari A, Rebah FB, Tahoon MA. Polyethylenimine-Modified Magnetic Chitosan for the Uptake of Arsenic from Water. Vol. 11, *Applied Sciences*. 2021.